GEOMETRICAL CONSTRAINTS ON THE FORMATION AND MELT OF RIDGED SEA ICE

by

Trisha Lynne Amundrud

B.Sc. Hons., Physical Science, University of Guelph, Canada, 1998

A THESIS SUBMITTED IN PARTIAL FULFILLMENT OF

THE REQUIREMENTS FOR THE DEGREE OF

DOCTOR OF PHILOSOPHY

in

THE FACULTY OF GRADUATE STUDIES

DEPARTMENT OF EARTH AND OCEAN SCIENCES
(Oceanography)

We accept this thesis as conforming

to the required standard

THE UNIVERSITY OF BRITISH COLUMBIA

October 2004

ABSTRACT

The Arctic ice pack consists of flat level ice, open water, and large ridge structures. During winter, ice thickens and is compacted into ridges, increasing the Arctic ice volume. In summer, ridging is accompanied by ice melt processes, which act to decrease ice volume. Current ice-atmosphere-ocean models cannot reproduce the evolution of the ridged ice fraction, suggesting that ridging or melt may be inappropriately parameterized. To increase our understanding of ridged ice evolution, this thesis investigates the factors that constrain the ridging and melt processes.

A unique ice draft distribution model is developed to simulate ice evolution in the Beaufort Sea, allowing direct comparison with observations of ice draft by moored sonar. Conventional ridging algorithms used in a 24-day simulation were found to overestimate the amount of very thick ice. Observations of level ice reveals that 75% of all ice floes are too small to create ridges of maximum draft. In addition, observed ridges have cusp-shaped keels with concave flanks, containing less thick ice and increased amounts of thinner ice than the triangular shaped keels assumed by most models. Including the observed constraints into the redistribution model produces ridged ice in agreement with observations, confirming the importance of the geometrical constraints to the creation of ridged ice.

During the melt season, simulations of ice ablation in the Beaufort Sea indicate that level ice melt processes cannot reproduce the observed enhanced melt rates of ridged ice. A semi-quantitative model for internal melt due to flow through the porous keel is developed and an enhanced internal melt rate estimated. The rate of melting within the porous structure of the ridge keel is up to an order of magnitude greater than the rate of melting at the surface of level ice floes. Including the internal melt within the ice draft distribution model can reproduce the enhanced melt of ridged ice and is thus essential for the accurate simulation of the evolution of ridged ice. Similar to the geometric constraints on ice ridging, the internal geometry of ridge keels plays a large role in the annual evolution of the thickest sea ice.

TABLE OF CONTENTS:

LIST OF TABLES

LIST OF FIGURES

PREFACE

Portions of Chapters III-VI have been published and presented as:

T.L. Amundrud, H. Melling, and R. G. Ingram. Geometrical constraints on the evolution of ridged sea ice. Journal of Geophysical Research (Oceans), vol. 109, C06005, doi:10.1029/2003JC002251, June 2004

T.L. Bellchamber-Amundrud, H. Melling, and R. G. Ingram. Modelling the evolution of draft distribution in the sea ice pack of the Beaufort Sea. Ice in the Environment: Proceedings of the 16th IAHR International Symposium on Ice, Dunedin, NZ, pp. 243-250. 2002.

ACKNOWLEDGEMENTS & DEDICATION

There are many people who have supported me during this research. My primary supervisor, Grant Ingram, has provided much needed support. Grant, your enthusiasm has helped me to enjoy this process and you've been an excellent role model and mentor! Committee members Garry Clarke and Susan Allen have been wonderful. Garry has made me feel welcome in his stimulating glacier research group and Susan's care in working through the thesis in the early stages has improved this work greatly.

Three individuals at the Institute of Ocean Sciences deserve credit for their assistance and support. My co-supervisor, Humfrey Melling, has been an invaluable resource and a questioning mind throughout this research. David Riedel performed the initial data analysis on the ice profile data. His efforts let me sleep well at nights knowing that all errors are mine alone. While at sea on the icebreaker Laurier in September 2002, Peter Gamble's instruction in maintaining the field equipment was wonderful and his enthusiasm and words of wisdom kept me happy. I would also like to acknowledge financial support from NSERC, Fisheries and Oceans Canada, and UBC.

My parents, Neil and Judy, have always encouraged me to pursue my research and offered financial support during my undergraduate degree when I took a low paying summer research position to gain experience. Your commitment to me, and your belief in my abilities has been essential to my success. My grandparents, Murray and Dorothy, have also been wonderful cheerleaders, always taking an interest and supporting my goals. My in-laws, Sue and Jim, and various other extended family members make a great support system. Dr. Gerry McKeon deserves credit for getting me excited about physics in the very beginning, and taking an interest ever since (and solving equation 9.7.5)

I want to especially thank my husband Cory, who has been there every step of the way through this research: listening, suggesting ideas, and learning far more about ice than you'd ever planned. The past few years would be nowhere near as bright without you. Thank you!

This thesis is dedicated to two strong and loving women who helped me become the person I am:

For Vera Arnold, nee Callaghan, (1920-2004).
Who taught me to see beauty in everything (and taught me how to drink whiskey).

and

For Audrey Bellchamber, nee Everitt (1913 -1993).
Who listened, believed, and taught me to be strong.

Thank you both for the love and laughter.

SECTION A: OVERVIEW AND INTRODUCTION

1. GENERAL INTRODUCTION

1.1. Motivation

The pack ice of the Arctic Ocean stretches over its polar seas in a thick, complex structure of ridges, leads, and flat level ice. Acting as an insulator between the cold Arctic atmosphere and warmer ocean water, the ever-changing arrangement of the pack ice regulates the heat flux between the atmosphere and ocean and thus influences the local and global heat budget. On timescales of days, gradients in the forces acting on moving pack ice cause floes to collide, raft over one another, and sometimes buckle and fail on impact. Ridges form as the ice fragments from sustained local failure are pushed into heaps along the line of interaction. These pressure ridges have been found to contain 68-73% of the total ice mass in the Beaufort Sea (Melling and Riedel, 1995) and are both an important component in the Arctic ice volume and a significant hazard for shipping and offshore structures.

As ridges form in the Arctic Ocean, the ice motion also opens leads and larger open water areas called polynyas that exist throughout the Arctic during the winter and spring seasons. Created by wind forcing, and water current drag, or thermal ocean heating, these areas are prevalent in thinner and marginal sea ice zones, and comprise 1% of the total pack area (Smith et al., 1990). Heat exchange in these open water areas is two orders of magnitude greater than the typical surrounding ice and snow, and thus are large contributors to regional heat budgets (Smith et al., 1990). In addition, the refreezing of these open water areas produces thin ice during midwinter and spring seasons that is easily ridged between thicker, older ice.

The complex arrangement of ice and open water in the Arctic influences the global climate in addition to the local heat budget. While the ice cover is an important influence on global climate, it is itself is one of the most sensitive factors responding to climate change with complex and indirect responses to global warming (Melling, 2002). Anticipated increased heat in the Arctic atmosphere could lead to decreasing amounts of multi year sea ice, and perhaps even a complete loss of the Arctic multi year ice pack. Millennial timescales in sedimentary records of large circulation changes (Darby et al., 2001) indicate that temperature increases of up to 5 degrees C have occurred over the past few thousand years in the Arctic. It is essential to be able to model and understand the ice-ocean-atmosphere system accurately, so as to make reliable predictions of

the response of the ice pack to projected climate changes similar in magnitude to those of the recent geological past.

Complicating the task of predicting ice cover changes in coastal regions is the large interannual variability and the influence of topography; the large number of islands contributes to the formation and movement of the ice pack. Recent work (Melling, 2002) in the Canadian Arctic Archipelago has found that the heavily ridged ice of the region is prevented from entering the Beaufort Sea by ice bridges between islands. Melling (2002) speculates that warming conditions thus may not bring uniformly lighter ice conditions to the Beaufort, as warming could decrease ice bridge blocking and flush heavily ridged ice into the Beaufort Sea. In a region of Canada where shipping is already highly dependent on ice conditions, the difference between a decrease in ice cover and an increase in ridged ice is of utmost importance.

The most useful tool scientists have for ice prediction is often computer modelling. Based on the observed conditions, a model should be able to forecast the future ice cover if the processes affecting climate are properly represented. Yet, current models show greatly varying results and often-erroneous ice cover characteristics (Proshutinsky et al.,2001). Model runs with current conditions will often underestimate the sea ice extent and thickness and overestimate melt (Cattle and Crossley, 1995). Others are biased towards larger thicknesses of ice (Flato and Hibler, 1995) leading to excess formation and slow degradation of thick ice ridges. The thermal growth and melt of flat level ice has been extensively researched and successfully modelled (ie. Maykut, 1986, Melling and Riedel, 1996a). Thus, the failure of models to evolve ice appropriately can be attributed to errors in the modelling of the processes controlling the formation and evolution of the thickest ice in ridges and rubble fields and suggests these processes must be further investigated.

While many physical components are incorporated into any ice-ocean-atmosphere model, the mechanical and thermal processes that affect the ridged ice require specific considerations. Thermal processes are often simplified under the assumption that simple heat balance calculations can account for changes in ice thickness. Yet simple heat balance models have failed to reproduce the ablation rates of the thickest, ridged sea ice (Flato and Hibler, 1995; Proshutinsky et al.,2001) leading to overestimates of ice draft in climate models. Since the ridges created by mechanical

forces are complex three-dimensional structures, perhaps the enhanced melt rates of ridged ice are due to the interaction of thermal processes with these complex geometries.

In concert with thermally driven freeze and melt processes; wind and ocean current forcing keeps the ice in motion, creating ridges and giving the ice pack its complex thickness distribution structure (Flato and Hibler, 1995). The mechanical processes acting to form a single ridge have been extensively studied due to the requirements of human activities in the north. Engineering design of ships, pipelines, and offshore structures must account for the unique constraints of the ice cover. This has motivated ridge research (Timco and Burden, 1997), leading to an understanding of the probable ridge distribution in the central Arctic ice pack (Thorndike et al.,1975; Lowry and Wadhams, 1979; and Mock et al.,1972) and ridge formation from level ice (e.g. Hopkins and Hibler, 1991). Applications of this knowledge of individual ridging processes to the thickness distribution for sea ice over regional scales should allow for more accurate representation of ridged ice in thickness redistribution models.

For ice-ocean-atmosphere models to correctly predict the distribution of sea ice, the mechanical and thermal processes that act on a ridge throughout the year must be better understood and appropriately modelled. In the following sections, the processes that create and maintain ridged sea ice will be reviewed and areas where our knowledge of the processes is limited identified.

1.2. Thermodynamics of sea ice

Thermodynamic sea ice growth or melt is determined by the balance of heat fluxes between the air, ocean, and ice. The rate of ice growth is a function of the longwave and shortwave radiation, conductive and oceanic heat fluxes, optical properties of the ice and snow surfaces, and the turbulent heat exchange. In addition, these parameters are functions of the cloud cover, open water area, wind forcing, and the current thickness of ice in the area (Maykut, 1986). Of all of these factors, in winter, when the water temperature is close to freezing, the temperature of the air often becomes the controlling variable. The simplest models of initial sea ice growth start with an estimate based on Stefan's Law, relating the number of cumulative freezing days, θ, to the ice thickness (Maykut, 1985). This yields a relationship of the form:

$$h^2 + Ah = B\theta \qquad (1.2.1)$$

where A and B are constants varying with location and snow cover (Maykut, 1986) and h is the thickness of the sea ice. Nearshore melt can be modelled in a similar fashion as a linear relationship between the accumulated days with temperature greater than freezing (Maykut, 1986).

From the above relationship (1.2.1) the estimate of ice growth, dh/dt, will be of the form:

$$dh/dt = f(1/h) + \text{other terms} \qquad (1.2.2)$$

suggesting that the rate of observed ice growth will be inversely proportional to the ice thickness. The atmospheric temperatures are much lower than the oceanic temperatures during the winter season. The resulting heat flux from the water to the atmosphere causes ice formation. As ice forms, it begins to act as an insulating layer inhibiting ice growth by reducing the heat flux from the water to the atmosphere, which for drafts from 0-0.4m is 1-2 orders of magnitude greater than the heat input from thicker perennial ice (Hibler, 1980). In addition, initial ice growth often occurs at higher rates due to turbulent wind mixing (Smith et al., 1990) in the upper centimetres of the water column. Frazil ice crystals can be mixed below the surface increasing growth rates. Wind also advects the newly formed frazil ice to the edge of an open water area, thus allowing more frazil ice to form and enhancing the ice growth rates (Cavalieri and Martin, 1994).

Ice thickness	Rate of ice growth
0 cm	13 cm day^{-1}
50 cm	2 cm day^{-1}
100 cm	0.8 cm day^{-1}
400 cm	< 0.1 cm day^{-1}

Table 1-1: Ice growth rates for central Arctic pack ice used as model input by Thorndike et al (1975).

A heat balance model (Cavalieri and Martin, 1994) of ice formation accounts for all significant input of heat into the ice from the ocean and atmosphere:

$$F_{net} = F_t + F_L - F_B - F_s + F_{oceanic} \qquad (1.2.3)$$

where the components on the right hand side are the turbulent heat flux, the longwave radiation down and up, the shortwave radiation down (Cavalieri and Martin, 1994), and the oceanic heat flux (Melling and Riedel, 1996a) respectively. In this model, snow is allowed to absorb a fraction

of the temperature difference between the atmosphere and the ice, reducing the temperature gradient and conductive heat flux but is not modelled explicitly (Melling and Riedel, 1996a). From this, the freezing growth rate of ice becomes:

$$dh/dt = F_{net}/\rho_i L_i \qquad (1.2.4)$$

where L_i is the latent heat of fusion and ρ_i is the ice density (Cavalieri and Martin, 1994). The individual components of the heat flux utilize measured meteorological data to estimate sea ice growth. The observationally based model of Cavalieri and Martin (1994) is easily implemented and has been adapted to allow for possible snow cover and applied successfully to ice growth in the Beaufort Sea (Melling and Riedel, 1996a).

Most current ice growth models should contain the caveat that they are only accurate for shallow sea ice drafts less than one metre in thickness (Maykut, 1985). At drafts larger than this, influences of porosity and non-uniformity in the ice may become more important. For most purposes, these estimates of sea ice growth are adequate as sea ice at 0-0.4m grows an order of magnitude faster than thicker ice (Maykut, 1985). This growth rate ensures that the greatest contribution of thermal cooling to ridge formation is in the development of thin ice available for ridging rather than thermal growth of previously ridged ice.

1.3. Ridge morphology

In an aerial view, the ridge sail protrudes above the level ice surface (Figure 1-1) while the greater mass of the ridge keel extends below into the water. Ridges often appear in linear sections joined by complex corners or bends with corner regions exhibiting greater accumulations of ice than linear sections (Bowen and Topham, 1996). Some locations may exhibit other ridge configurations such as the honeycomb appearance observed in the Weddell Sea (Granberg and Lepparanta, 1999) where large spatial variations in ridge configuration are not correlated to the distance from the ice edge. In the Beaufort Sea the arrangement of ridges has been observed to form orientated failure patterns (Hibler and Schulson, 2000). Using a sea ice model, Hibler and Schulson (2000) found ice flaws formed along preferred failure lines intersecting at angles of 25-30 degrees with a natural preference for flaws to form in an alternating manner as damage propagated. Full modelling of ridge orientation becomes complicated further by land-ice interactions and as such, ridge orientations are often treated statistically or ignored in ice models.

Typical to all ridges, the keel underneath the sail is both wider and taller to achieve isostatic balance. This balance occurs over scales of 20 to 100 m across a ridge (Bowen and Topham, 1996; Melling et al., 1993) as the force generated by the sail's ice area can exceeds the buoyant force created by the area of the keel directly underneath the sail and some proportion of the sail gravitational force is thus carried the wider flanks of the keel. In addition, the keel must balance the additional gravitation force of any snow cover.

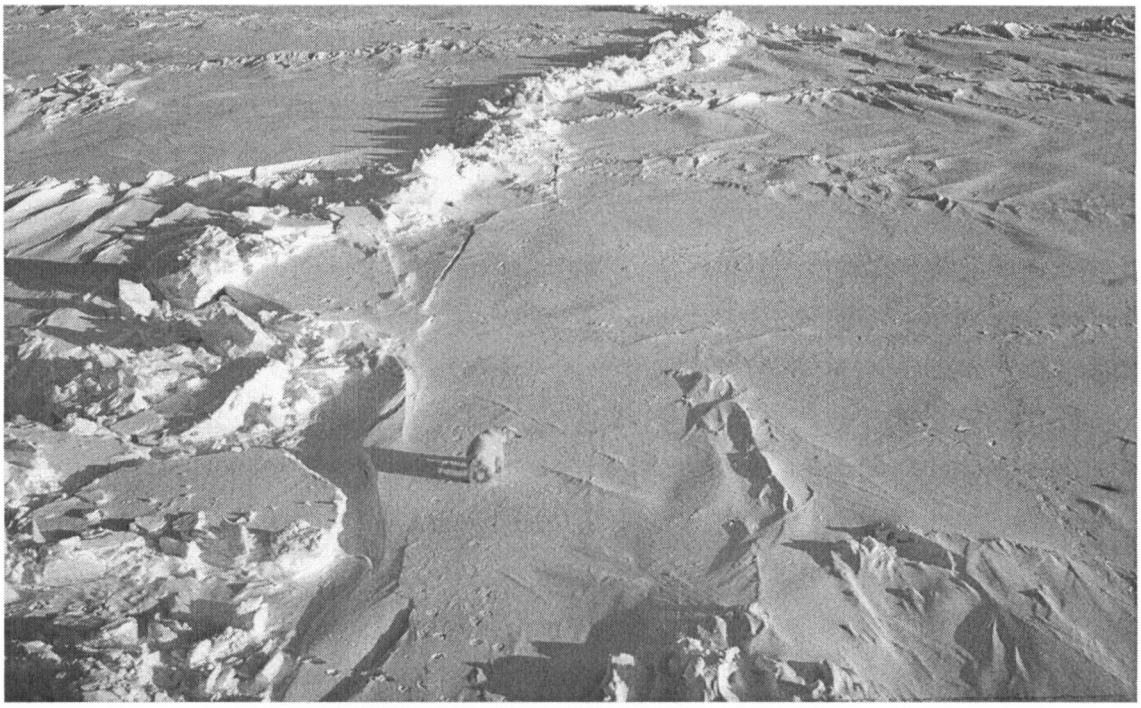

Figure 1-1: View of ice cover in the Beaufort Sea. The intersection of two floes to form a ridge structure is clearly visible across the upper left side of the photo. Additional structures are also present. Courtesy of H. Melling.

Observations of ridge structure often focus on the ridge sail topography due to the relative ease of data collection above the waterline. This is a questionable approach for quantifying ice volume, as the undersea area and volume of ridged ice is considerably greater than that of the upper surface. Multi year sails are often eroded with sail to keel thicknesses decreasing to approximately ¾ of their original values (Timco and Burden, 1997) and can be as smooth as level ice (Granberg and Lepparanta, 1992). Further complications include snow drifts that pile up at

ridges similar to drifts at a snow fence making discernment of ridge shapes difficult (Granberg and Lepparanta, 1992).

Field studies have provided rough generalizations of ridge geometry, although individual ridges vary greatly. Averaged ridge ratios and geometries displayed in Table 1-2 illustrate the sail-keel thickness and width ratios needed to satisfy isostacy. The idealized triangle keel geometry assumed in most ice ridging models (e.g. Thorndike et al., 1975; Flato and Hibler, 1995) is not observed except in larger ridges (Lepparanta and Hakala, 1992). Multi year ridges generally exhibit broader and more rectangular keels (Timco and Burden, 1997) than first year ice, differences attributed to seasonal degradation processes (see chapters 1.5 and 1.6).

Due to the mechanisms of ridge formation, most ridges begin with a loose porous block structure where the draft is a multiple of block thicknesses (Melling et al.,1993). These structures consolidate through freeze and melt processes as the winter progresses (Rigby and Hanson, 1976) although this consolidation layer is highly variable (Timco and Burden, 1997) and freeze-melt processes are not understood for porous structures. Some estimates of first year ridge porosity have ranged in the literature from 20-45 % (Bowen and Topham, 1996) with reported averages of 30% (Timco and Burden, 1997). Multi year ridges, due to ridged ice evolution processes (discussed in chapters 1.5 and 1.6), generally have very low porosities. The porosity also varies within the vertical structure of a ridge, with higher porosity in the keel than the sail attributed to lower relative gravitational packing forces (Lepparanta and Hakala, 1992; Melling et al., 1993). Ordered identical spheres will pack to a porosity of 25%, this comparison indicates the loose nature of the typical ridge structure with porosity 30% (Lepparanta and Hakala, 1992).

The strength of sea ice is obviously influenced by the ridge structures. For engineering design, the load applied to a mechanical structure will be a function of the ridge thickness, porosity/consolidation, and horizontal ridge extent (Tom Brown, University of Calgary, personal communication). On larger scales, models of ridge formation consider the strength of level ice, which must fracture and crumble to form ridges. Compressive strength of the ice is a function of the amount of thin ice and its thickness (Richter-Menge and Elder, 1998). Ice strength decreases with increasing scale, such that lab-scale strengths are approximately 2 orders of magnitude greater than mesoscale strengths (Dempsey et al., 1999). The tendency for the tensile strength in-

situ strength of ice to be less than results from lab testing is attributed to pre-existing cracks in the ice (Richter-Menge and Elder, 1998).

Ridge ratios	First year ridges		Multi year ridges	
Keel to sail height	3.95 + 0.12	*4.5 - 5*	3.17 + 0.08	*3.1 - 3.3*
Keel width to height	3.91 +0.16		----------	
Keel width to sail width		*4.4*		*3.2*
Keel area to sail area	7.96 + 0.33		----------	
Sail angle	32.9 + 9.2°	*25°*		*20°*
Keel angle	26.6 + 13.4°	*33°*	----------	
Porosity	~30%		Very low	

Table 1-2: Common ridge statistical ratios reported in Timco and Burden (1997) from a survey of 112 first year ridges and 64 multi year ridges. Italicized values are reported in Melling et al., (1993) from the literature. Of interest is the ratio of keel to sail geometries with keels taller and wider than sails by an approximate factor of four.

1.4. Mechanics of ridge formation

The ridge geometries and keel drafts of the previous sections are not static, but constantly evolving. The mechanical and thermal processes acting on the ice vary seasonally to provide an annual cycle in ridge evolution. This balance of processes can be simplified to a picture where the formation of ridges occurs mainly in winter, and ridge degradation primarily in summer (Figure 1-2). It is expected that with a solid understanding of winter and summer, the shoulder season sea ice development can be modelled as a combination of known mechanisms. For simplicity, this thesis will address mechanical ridge formation in winter and summer ridge ablation.

During formation, the convergence and divergence of the pack generate both ridge and open water formation. In the ice covered and land-bounded Arctic Ocean, divergence and convergence are essentially one process, as divergence in one region causes convergence in another. Winds and currents continue to open leads and polynyas throughout the winter season where new ice forms and can then be compressed by thicker pack ice to form pressure ridges (Smith et al., 1990).

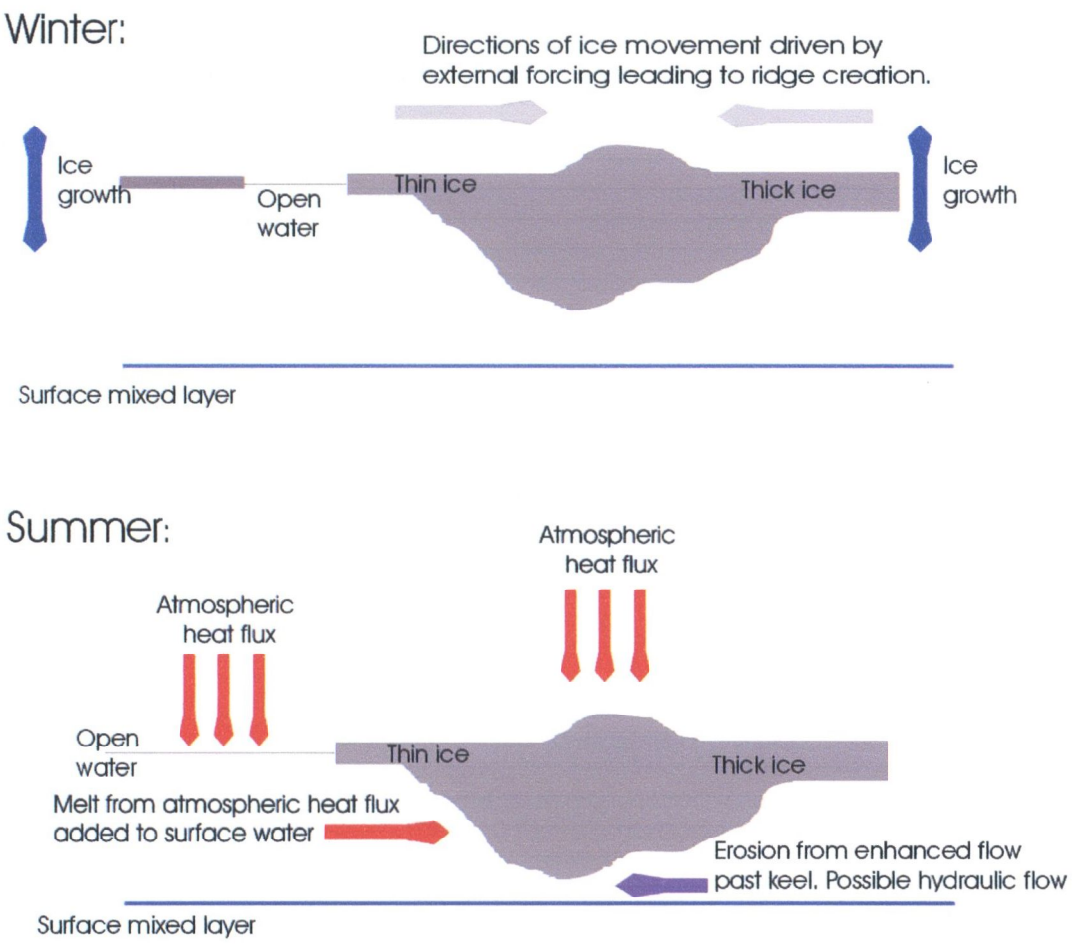

Figure 1-2: Schematic of the dominant processes acting on ridges during winter and summer. Thermodynamic melt is indicated in red, thermodynamic growth in blue, and mechanical forcing in grey (movement of ice) and purple (movement of water).

The contributions of mechanical forces to ridge formation have been extensively modelled through particle simulations. Initial work by Parmerter and Coon (1972) dealt with the compression of a rubble-filled lead by an ice sheet that would break under flexure with limiting assumptions restricting the repose angles of sail and keel. The central pile was found to grow until a maximum height was reached at which point it began to grow laterally. The maximum sail height of the modelled keels was 5 to 6 times the thickness of the level ice consumed in ridging. This direct linear relation contrasts with the observed relationship of 16 $m^{1/2}$ $h^{1/2}$ found by Melling

et al., (1993) in the Beaufort Sea and is at the upper limit of the range reported by Lepparanta and Hakala (1992) of $h^{1/3}$ to h^{1}.

With the increasing capacities of numerical models, more recent work has improved the particle simulations. Models have gained realistic block definitions and inter-particle forces with frictional and elastic contacts (Hopkins et al., 1991) and varying initial conditions (Hopkins and Hibler, 1991). Differing ice types involved in the ridge formation have been investigated including the compression of thin ice floes (Hopkins, 1994) or rubble filled leads with both polygonal and disc shaped particles (Hopkins et al., 1991).

A coherent picture of the stages of pressure ridging can be developed (Hopkins, 1998) based on the results of various particle simulations. Initially, the compression of thin ice against a thicker floe initiates ridge formation. The keel appears to function as the support for the sail portion of the ridge with growth exhibiting cyclic alterations of sail and keel development (Hopkins, 1994). With continuous driving ice velocities, the sail reaches a maximum height first (Hopkins, 1996a) after which the keel grows to its maximum draft. At this final stage, growth continues in the horizontal direction until all thin ice has been consumed. Finally, the ridge evolution continues with a compression of the ridge as characterized by a thick rubble field (Hopkins, 1998). The final draft reached by the keel in these models agrees with the observed relationships of Melling et al., (1993) and produces porous structures matching observed porosity estimates.

Of interest, several features and controlling factors of ridge development are apparent from particle simulations that produce ridge geometries and porosities consistent with observations (Hopkins, 1998). While the thickness of lead ice determines the ridge width and thickness (Hopkins, 1994), the ice sheet velocity (within observed ranges) does not have a significant effect on the resulting ridge structure (Hopkins, 1998). In all simulations, the ridge profiles appear to have a trapezoidal keel shape (Figure 1-3), in agreement with observations (Lepparanta and Hakala, 1992) and in contrast to the triangular shapes of larger scale models (e.g. Thorndike et al., 1975). The ridges formed from an intact frozen lead require much more energy for the potential energy of the constructed ridge than a similar ridge constructed out of rubble blocks (Hopkins and Hibler, 1991). This is likely due to the excess energy required to break the blocks, although as the ratio of work to potential energy is approximately 15 or 20 to 1, most of the

energy is consumed by frictional processes regardless of the initial ice conditions (Hopkins and Hibler, 1991; Hopkins, 1994).

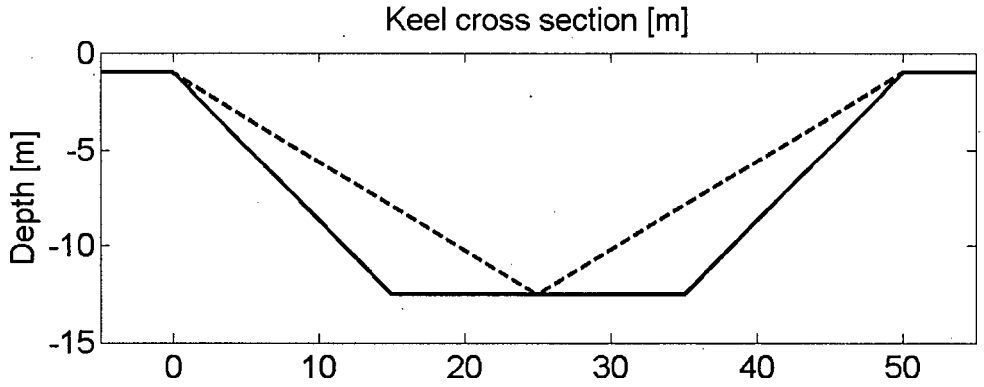

Figure 1-3: Keel schematic showing trapezoidal (solid line) and triangular (dashed line) cross sections.

Convergent ice motion can lead to rafting of sea ice as well as ridging. Rafting involves the movement of one ice sheet over another, and in contrast to ridging, produces low porosity structures. Babko et al (2002) identify two types of rafting processes; simple rafting where one sheet slides atop another, and finger rafting, where the ice sheets fracture perpendicular to the ice edge and form fingers of overthrusts and underthrusts. In the Weddell Sea, rafting of thin sea ice has been observed to increase ice growth substantially (Lange et al., 1989). Waves break and raft the newly formed ice resulting in thicker rafted ice areas and regions of open water. These regions of open water are then able to freeze at the open water rate leading to an increased volume of ice production.

A conventional view of rafting holds that only the thinnest ice is available to raft. Parmerter and Coon (1972) restrict rafting to ice thinner than 0.17 m while Babko et al., (2002) suggest a higher cut-off value of 0.75 m where ridging takes place only for ice thicker than 0.75 m. These simplifications do not truly represent the ice conditions observed. Ice over 2 m in thickness has been observed to raft, facilitated by breaking at the edges and lubrication from brine drainage in the upper sheet or by a rubble field of thin ice which can serve as a ramp for the thicker ice sheet (Babko et al., 2002). Rafting and ridging are equally possible for medium thicknesses of ice and there exists no range at which either should be excluded. No guidelines are currently in place for

determining the initial conditions leading to rafting although it is suggested (Babko et al., 2002) that rafting is the preferred form of interaction between floes of uniform thickness and ridging occurs, as simulated (Hopkins, 1994), from the interaction of one thick and one thinner floe.

While the standard ice thickness evolution models (Thorndike et al., 1975; Flato and Hibler, 1995) do not include a rafting mechanism, newer ice models are beginning to include a rafting component (Haapala, 2000) within their mechanical processes. This will likely improve the accuracy of modelled ice within the rafted draft range (1 – 5 m). The accuracy of the thick ice found in the largest ridges produced by the ridging models has yet to be addressed and is the focus of this thesis.

1.5. Winter ridge evolution

Once a ridge is formed, it continues to evolve through the growth of a consolidated layer, packing and lateral erosion, the deterioration of the unconsolidated rubble, and ice melt (Lepparanta et al.,1995; Hϕyland, 2002). Of these, the separate contributions of the processes of packing, erosion, and melt are unclear as they are thought to occur in parallel and are discussed in chapter 1.6. The process of consolidation is in comparison, well understood. After a ridge is formed, the rubble will begin to consolidate by freezing from the water surface downwards (Bowen and Topham, 1996) until there exists a frozen nucleus at the water level connecting with the level ice as a continuous ice field (Lepparanta and Hakala, 1992).

The consolidation process can be further separated into two phases, an initial phase where heat energy is redistributed between water and the surrounding ice blocks, and the main consolidated layer formation phase (Hϕyland, 2002). Models of this initial consolidation phase indicate that a purely conductive heat transfer is too slow (Hϕyland, 2002) and thus some flow of water through the ridge structure is expected. This is supported by observations of consolidation processes in level ice where fine-grained brine drainage networks (Cole and Shapiro, 1998) having porosities of up to 10% are developed. Combining this with a ridge structure's macro porosity averaging 30%, the total porosity of a ridge on formation is estimated to be 40% (Hϕyland, 2002). It is this high porosity that we believe causes the quick heat energy transfer throughout a ridge structure and this porosity is essential for transferring heat to the ice during the melt season as well (see sections D and E). Observations by divers at the start of the spring melt found that the ridge

keels were porous to bubbles from the divers equipment, suggesting a permeable ridge structure (Lepparanta and Hakala, 1992).

Once the heat energy has been redistributed, the consolidation layer begins to form as the atmospheric freezing temperatures are transferred through the ice via conductive heat flux (Hϕyland, 2002). As the consolidated layer grows, its growth is determined by the thermal history rather than the surface heat balance (Maykut, 1986) due to the time needed for temperature changes to penetrate through the already consolidated ice. The growth of the consolidated layer proceeds much faster than level ice growth, as would be expected for a structure which is not forming a complete sheet of new ice, but merely freezing the gaps between ice blocks. Analytical models predict growth rates approximately twice that of level ice (Lepparanta and Hakala, 1992; Hϕyland, 2002; Veitch et al., 1991). Comparing the observed consolidated layer depth to expected values; Lepparanta et al., (1995) observed consolidated layer depths in agreement with analytical estimates while Hϕyland and Lϕset (1999) and Veitch et al., (1991) observe shallower than predicted consolidated layers, perhaps due to incorrect porosity assumptions, insulation by the ridge, or two and three-dimensional effects.

Observational studies by Lepparanta et al (1995) and Hϕyland and Lϕset (1999) document the complete degradation of seasonal pack ice ridges in the Baltic Sea and in a Spitsbergen fjord, and describe the evolution of the consolidated layer in the ridges. From early February to mid April the consolidated layer of ice grows downward as water pockets freeze and unifying the loose porous blocks. This leads to a reduction in total keel porosity from 28 to 18% (Lepparanta et al., 1995) and along with mechanical arrangements in block packing, begins to decreases the high porosity of a first year ridge. Due to the formation of the consolidated layer, the porosity of the ridge is now not uniform. Consolidated ice may have porosity of only 3.4% (Hoyland and Loset, 1999) while the porosity of the unconsolidated keel remains high. Observations have shown either no change in the unconsolidated keel porosity after consolidation (Lepparanta et al., 1995) or minimal decrease (Hoyland and Loset, 1999) and thus suggest that a constant porosity in the loose, unconsolidated blocks is an adequate assumption for most modelling approaches (Hoyland, 2002). This implies, that while the consolidated layer of a ridge is resistant to erosion processes, the loose and unconsolidated keel may be susceptible to mechanical erosion.

1.6. Spring and summer ridge ablation

The third process to affect ridge evolution, after formation and consolidation, is ablation from thermal melt and mechanical erosion. These processes are most visible in summer months when overall ridge draft decreases. Melt in summer occurs through solar heating on the ice surface leading to melt ponds and through heat added to the water column in areas of open water. For melt occurring in the winter, any heat must come from below the mixed layer where sufficient heat may be entrained upwards (Figure 1-2). In Arctic waters, the temperature in winter can increase with depth due to atmospheric heat loss (Figure 1-4) although the temperature anomaly above freezing is very small when compared with the summer oceanic temperatures. Heat budget models similar to those discussed for ice growth can be derived for the melt of level ice (Lepparanta et al., 1995) where the dominant direction for melt is vertical rather than horizontal ablation. This follows as lateral melt rates are the same order of magnitude as vertical rates such that most of the change in volume is due to changes in thickness rather than area (Bjork, 1992).

The main body of work examining ridge degradation and summer evolution has been observational and often focused on seasonal ice. For example, Lepparanta et al (1995), Lepparanta and Hakala (1992), Veitch et al., (1991), and Hϕyland and Lϕset (1999) observe the complete degradation of seasonal pack ice ridges in the Baltic Sea and a Spitsbergen fjord. Although the reported work focused mainly on the consolidation processes, some observations on ridge melt were made. Lepparanta and Hakala (1992) reported that at the start of the spring melt season the keel blocks were well rounded and easily collected by divers. Lepparanta et al., (1995) also reported loose keel blocks although they found no evidence of erosion.

A summer melt cycle, including the transition to multi year ice, was observed by Rigby and Hanson (1976). They observed a strong depth dependent melt rate with deep draft features showing higher loss rates than shallower portions of the keel. Shallower portions also showed more resistance to drilling, indicating harder ice, and it is suggested that the deeper parts of the keel may shield the shallower portions from thermal melt and mechanical erosion. Consolidation in the first year ridge was evident with voids in the ridge volume becoming slush filled as the summer progressed, leading to multi year ridges of lower porosity and lower melt rates than first year ridged ice. Of importance, the general ablation rate for the ridge keel that is several times that of the level ice indicating that ridge specific processes are influential.

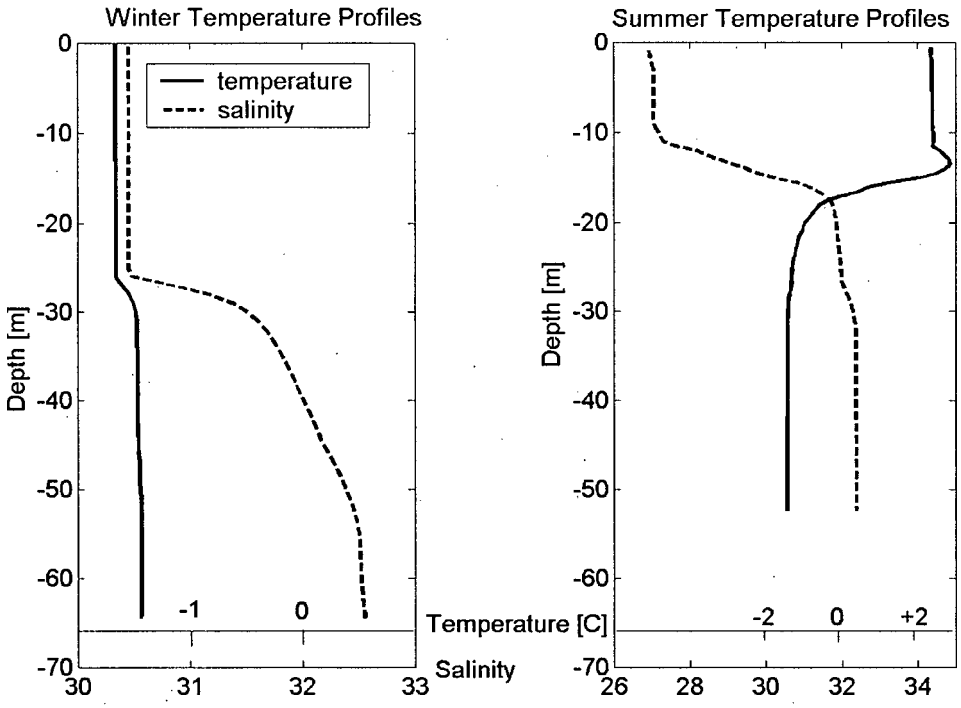

Figure 1-4: Typical temperature and salinity water profiles with depth [dbar] from the Beaufort Sea in winter and summer seasons. The typical changes in the mixed layer depths are evident here with the summer mixed layer being much shallower, and the change in density greater, than in the winter. Data provided by H. Melling.

Thermal melt in a ridge is more complicated than in level ice due to its structure of level ice blocks that are interspersed with large voids that will affect drainage, temperature conduction through the ice, and mechanical circulation. No complete models of ridged ice melt exist, although simplified models have investigated the importance of brine pockets and channels (Bitz, 1999) and geometry (Schramm et al., 2000) on melt rates. A complete understanding of ridge melt is of great importance to ice melt estimates but models consistently fail to reproduce the observed (Rigby and Hanson, 1976) higher melt rates (Flato and Hibler, 1995; Schramm et al., 2000). With ridged ice containing up to 68-73% of the total ice mass of some regions of the Arctic (Melling and Riedel, 1996a), an improved understanding of their melt processes is essential.

Why is the melt rate higher in keels than level ice? In agreement with Rigby and Hanson (1976), Flato and Hibler (1995) found that a lack of preferential thick ice melt made their model over predict the thick ice in their distribution. Schramm et al., (2000) suggest that factors such as increased surface area due to the sloping sides and accelerated flow around the keel increase the turbulent heat flux and contribute to thermal melt. Their work models 1-D and 2-D heat conduction effects in ridged ice to determine if purely thermodynamical processes can explain melt rates. By assuming 2-D heat conduction (which better approximates reality than a 1-D model) they find that increased surface area and internal heat conduction can account for only a small portion of the observed enhanced melt rates. The increased heat flux to the keel from accelerated flow velocity past a keel structure could produce melt rates 3 times that of the surrounding level ice, which may explain part of the enhanced melt rate observed (Rigby and Hanson, 1976) and could work in tandem with mechanical erosion and the influence of porosity on the melt processes. It seems likely that the porous nature of first year ridges will greatly aid in the conduction of heat through a ridge and thus increase the melt rate although no provision for porosity exists in current models (Schramm et al., 2000).

The observed contributions of mechanical erosion to ridge degradation is contradictory; Lepparanta et al., (1995) observe little mechanical erosion in winter, Rigby and Hanson (1976) report mechanical erosion causing high draft loss in summer. Samples of winter keel blocks in the Baltic (Lepparanta and Hakala, 1992) show loose, eroded, and porous blocks. Rigby and Hanson (1976) observe similar loose blocks throughout the entire summer and estimate that erosion of these blocks accounts for losses of up to half of the original thickness of a first year ridge. An explanation for the lack of erosion reported by Lepparanta et al., (1995) could stem from regional differences. Rigby and Hanson (1976) observed a ridge in a highly salinity and temperature-stratified region (similar to Figure 1-4). Lepparanta et al., (1995) observed ridges in the Baltic Sea, where different stratification regimes could reduce the potential for mechanical erosion.

Support for seasonal variations in erosion lies in the reduction of mixed layer depth (Figure 1-4) in summer. Solar heating both increases the temperature and freshens the water through ice melt, which increases stratification. If the water column is simplified to a two-layer flow, the decrease in depth of the upper layer can enhance flow past a keel due to conservation of volume.

Enhanced velocity of flow will not only increase heat conduction (Schramm et al., 2000) but may trigger hydraulic jumps and internal waves.

Similar to the two-layer flows over mountains or fjord sills (Farmer and Denton, 1985), the upper 100m of the Arctic forms a two-layer system flowing past a ridge keel where the keel surface slopes are on the same order of magnitude as mountain slopes (Pite et al., 1995). Laboratory experiments (Pite et al., 1995) predict the existence of a supercritical lee jet formed from a hydraulic jump downstream of a keel with a forward propagating bore. Numerical simulations (Cummins et al., 1995) support laboratory experiments and predict variations in hydraulic flow including soliton formation upstream of keels for steep-sided ridges (Cummins, 1995). Predicted hydraulic jumps and solitons occur for Froude values in the range of 0.25 to 1.35 (Cummins, 1995; Cummins et al., 1994, and Pite et al., 1995) which, using the density variations calculated from the profiles in Figure 1-4, can occur under common keel drafts and flow speeds.

The flows past the keel are tidally driven, and as such, produce a cyclic pattern of upstream bores, jumps, and soliton formation (Cummins, 1995). Ongoing observational work (Marsden, personal communication with R.G. Ingram) is attempting to observe these hydraulic features in two-layer flow past ridges in the Canadian Arctic Archipelago. Oceanographic situations vary from numerical and laboratory experiments in that the Arctic ice pack, as they consist of multiple ridge keels, such that hydraulic flow past one keel will likely interact with the next ridge feature. Thus predicting the effects of enhanced velocity and hydraulic flow on ridge melt becomes complex, yet the resulting increase in turbulent and potential energy to the water column has the potential to increase erosion and melt.

In summary, while the thermal melt of level ice is well understood, the processes of mechanical erosion, thermal melt with flow through a porous structure, and enhanced velocity past a keel on the ablation rates of ridges is largely unknown.

1.7. Research objectives

The above reviews of keel structure, formation, consolidation, and ablation processes highlight what is known about ridged ice formation and evolution. Previous work has investigated many of the processes that contribute to the evolution of an individual sea ice ridge, and yet the

compilation and assimilation of these processes into larger scale models is incomplete. The failure of current models to produce accurate and inter-model consistent ice cover characteristics (Proshutinsky et al., 2001) indicates that the mechanical and thermal processes that act on a ridge need more accurate representation in models of sea ice evolution. The goals of this thesis are therefore:

a. To determine why sea ice models are misrepresenting the amount of thick ridged ice.
b. To increase our understanding of the physical processes of ridging and melt (and constraints on those processes) that act on thick ridged ice.
c. To develop more accurate sea ice evolution algorithms for the evolution of the thickest ice.

These objectives require a unique approach to sea ice modelling. While most models evolve ice on either basin (e.g. Hibler, 1980) or individual ridge (e.g. Hopkins, 1998) scales, this research will model the evolution of mesoscale parcels of ice (O(50km)). This unique scale will allow large area-averaged ice pack characteristics to be compared with individual ridged ice features. Using an ice draft redistribution model adapted to short (~15-30 days) natural experiments in the Beaufort Sea, the ridging and melt processes evolving ridged ice can be isolated and studied.

This research can be separated into three sections. In section B this research sets out to evaluate currently used sea ice ridging and melt algorithms through the following steps:

1. Adapt the commonly used ice redistribution model (Thorndike et al., 1975) to evolve ice undergoing onshore convergence in the Beaufort Sea during the winter of 1997-1998.
2. Compare model results with observations of ice draft from moored subsea sonars.
3. Identify the discrepancy between modelled and observed ridged ice distributions during winter when ridged ice is being produced.

The tendency for models to create excess thick ridge ice is then explored in Section C. By combining model output with observed ice draft profiles, new insights into limitations of ridge sizes and shapes can be found. This portion of the research can be summarized as the steps:

4. Use observations of ice pack geometrical characteristics to determine geometric constraints on the formation of ridged ice.

5. Adapt ridging algorithms to include constraints on ridge size and shapes, allowing for improved simulation of ice evolution.
6. Validate the importance of these geometrical constrains through application of the model to a different year (the winter of 1991-1992) and to idealized distributions.

In the latter part of the thesis (Section D), the enhanced melt of ridged ice is investigated. Before sea ice models can reproduce the evolution of ridged ice, we must understand the process or processes that cause the observed enhanced melt rates in thick ice. Using the ice draft redistribution model, estimates of the enhanced melt can be made and will lead to the development of a semi-quantitative model for porous melt within ridge keels. The steps taken to develop this model are:

7. Adapt the winter model to the melt season and identify enhanced ablation rates within the thick, ridged ice.
8. Develop a semi-quantitative model for porous melt within ridge keels.
9. Using assumptions of keel geometries and ocean characteristics based on observations, calculate expected internal melt rates and evaluate the ability of internal melt to account for observed enhanced ablation rates.

The results of the thesis will demonstrate that current knowledge of ridged ice evolution is often limited to the evolution of a single idealized ridge. By extending our scope to look at ridge specific processes and their impact on the distribution of ridged ice, we will be able to build on current knowledge and develop a better understanding of the entire sea ice pack.

2. SEA ICE REDISTRIBUTION MODELS

2.1. General overview of statistical descriptions

In addition to characteristics of individual ridges, it is useful to look at the statistical descriptions of a region of sea ice that consists of ridges, level ice, and open water. On regional or basin scales, it is efficient to look at a statistical representation of sea ice rather than a description of each individual feature. One common representation used is the probability distribution of sea ice draft or (interchangeably) thickness (Figure 2-1) where the level ice is represented in peaks at 1.2 and 0.6 m and thicker ridged ice is apparent in the tail of the distribution. Visible in Figure 2-1 is the often-observed (Melling and Riedel, 1996a; Melling and Riedel, 1995) exponential tail of ridged ice in the draft distribution.

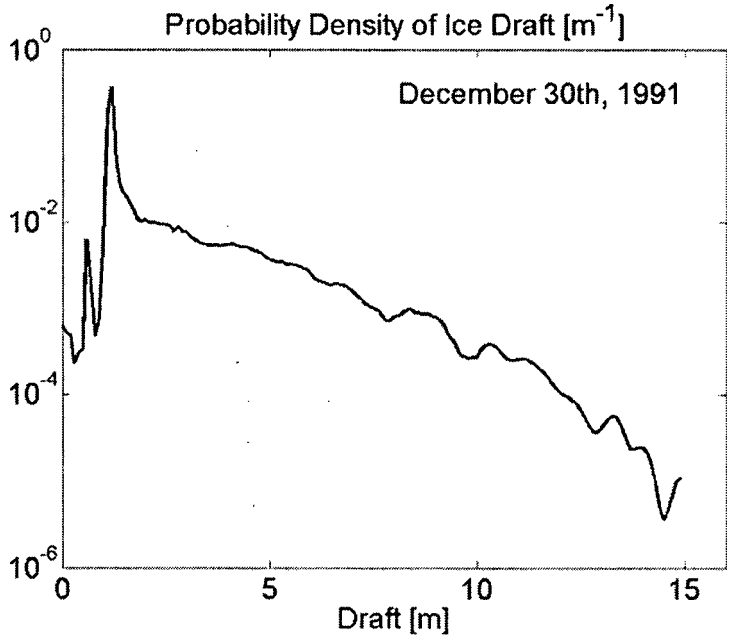

Figure 2-1: The statistical representation of the probability density distribution of sea ice draft (fraction per metre). Data are from the end of December, 1991 in the coastal Beaufort Sea. The level ice peaks at 1.2 and 0.6 m are visible as strong signals in the distribution. Open water is a much smaller peak. The exponential tail of ridged ice stretches from 1.5 m to 15 m, at which point no further observations of ridged ice were made. Data courtesy H. Melling.

In addition to the distribution of sea ice thickness, the spatial distribution of sea ice provides information about the horizontal structure of the sea ice pack. Analogous to ridge drafts, the

spatial ridge distribution though the ice pack off Alaska has been described with an exponential probability distribution $P(x)=\mu \exp(-\mu x)$ (Mock et al., 1972) where x is the horizontal distance. This and other statistical models for the distribution of pressure ridges (Lowry and Wadhams, 1979; Hibler et al., 1974) begin with an assumption of randomness. Yet significant directional anisotropy in ridge orientation has been found and coastal interaction may cause regions of higher ridging (Tucker et al., 1979; Hibler and Schulson, 2000). To avoid the assumption of randomness, Rothrock and Thorndike (1980) propose using more general properties of the ice profile such as an autocorrelation function.

To describe the regional characteristics of ice roughness, the fractal dimension of sea ice can be employed. The slope of the autocorrelation function of ice draft can be seen to increase as the lag decreases, indicating that the underside surface of the ice has a fractal dimension (Melling et al., 1993; Rothrock and Thorndike, 1980) and thus is a rough surface. The reported dimensions for sea ice fall clearly in the range of a rough profile with the exception of Rothrock and Thorndike (1980) who find smooth, non-fractal ice. Fractal dimensions found in the Beaufort Sea are remarkably constant (1.57 ± 0.06, Melling et al., 1993; 1.50 ± 0.05 for first year ice and 1.52 ± 0.02 for multi year ice, Melling and Riedel, 1995; and 1.44 ± 0.064, Bowen and Topham, 1996) and indicate a rougher profile than terrestrial landforms (Melling et al., 1993). Overland et al., (1995) suggests the use of the fractal dimension of sea ice as a state variable representing the aggregate properties of the pack. Physically, the fractal dimension is a measure of the surface area to volume ratio of the ice and is high, due to the loose block structure of a ridge. This influences both surface-exchange processes and creates a unique habitat for substrate-dependent biology.

2.2. Ice draft redistribution models

Using a probability distribution of sea ice draft to characterize the ice pack in a region allows the representation of ridge formation as an evolution of the thickness or draft distribution probability density function, *g(h)* (Thorndike et al., 1975). While Thorndike et al., (1975) and later researchers model ice thickness, draft and thickness may be used interchangeably and for the purposes of comparison with observed data, this thesis will refer to ice draft redistribution models. If we consider the distribution shown in Figure 2-2, during ridge formation ice is converging and diverging in different areas. This is seen in the distribution as a shift of ice to larger drafts, as more ridged ice is created (convergence), and as the creation of open water to

conserve volume (divergence). The thermal effects of melting and freezing shift the distribution to lower and higher drafts, respectively.

The evolution of the thickness distribution function, g(h), was first formulated by Thorndike et al., (1975) who represented the advective, thermodynamic, and ridging processes in the following form:

$$\frac{\partial g}{\partial t} = -\nabla \cdot (\vec{u} g) - \frac{\partial}{\partial h}(fg) + \psi \qquad (2.2.1)$$

The first term on the right hand side represents divergent motion with $\vec{u}$ being the horizontal velocity of the ice. The second term represents thermal growth by the thermal growth function, f, and finally, the third term represents the mechanical ridging. Thorndike et al., (1975) assumed a static form for f and a complex ridging function, ψ, which handled both the creation of new water through divergence and the transfer of level ice to thick ice through ridging (Figure 2-3). This function, ψ, depends on the strain rate along with the assumption that the thinnest 15% of ice is ridged into structures five times the level ice thickness.

A modified version of the thickness redistribution equation was developed by Hibler (1980). In this redistribution model, a lateral melt term, F_L, is added and the ice growth function, f, is represented as a heat budget that contains an ocean boundary layer model with a fixed oceanic mixed layer depth. This formulation is expanded to include snow cover in the ocean basin scale model of sea ice dynamics and thickness (Flato and Hibler, 1995). Both formulations of the ridging function, ψ, were improved to create maximum deformed ice thickness that scales as the square root of level ice, $h^{1/2}$, in agreement with Melling et al., (1993) and Hopkins (1998), although the restriction that only the thinnest 15% of ice may ridge is maintained.

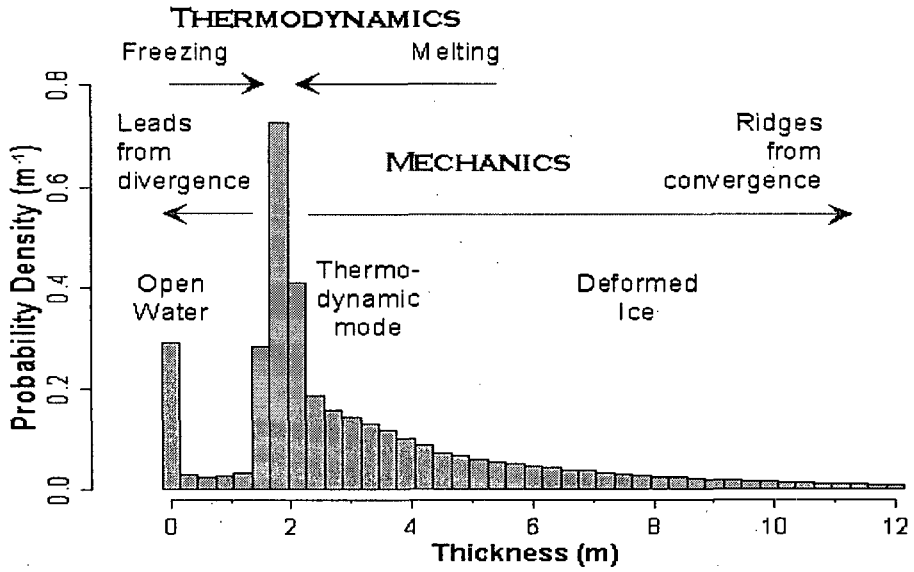

Figure 2-2: Schematic of the effects of mechanical and thermal forcing on the probability density function of ice draft. Level ice peak is at 1.8 m and indicates the proportion the ice pack that is level ice of this thickness. Figure courtesy of H. Melling.

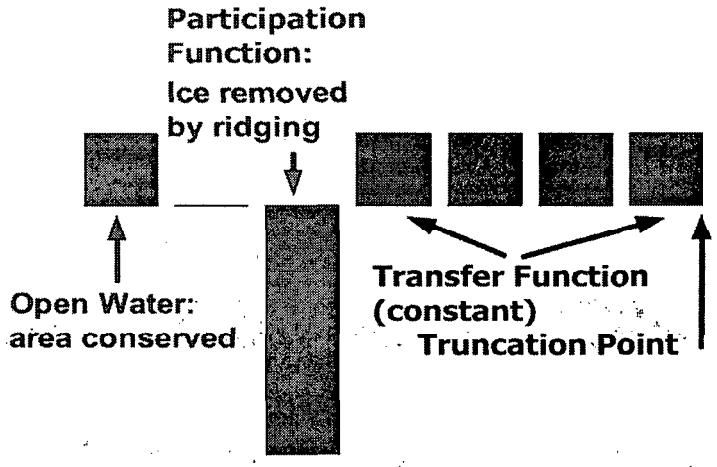

Figure 2-3: Form of mechanical ridging function, ψ. Level ice is removed by the participation function and redistributed through the transfer function. Open water is created to conserve area.

Hopkins (1996b) compared the thickness redistribution function (Thorndike et al., 1975) with the redistribution of thickness with the ridge formation processes of Hopkins (1996a) in a mesoscale model. The initial ice pack consists of polygonal parcels of ice that can interact through the elastic-plastic contact model driven by specified strain rates. This produces ice pack thickness distributions over time that are found to be in reasonable agreement to the thickness redistribution predicted by Thorndike et al., (1975) although only a single distribution was calculated in Hopkins' (1996b) study.

One limitation to either the Thorndike et al., (1975) or Hibler (1980) approach lies in the details of the ridging term in (2.2.1). The assumption that only the thinnest 15% may ridge makes the form of ψ non-linear; assuming a cut-off height above which ice cannot ridge, such as the limit of first year level ice growth, can remove this non-linearity. Thorndike (1992) formulated ψ as a product of the strain. The thermodynamic growth is represented as a mean annual forcing which produces thickness distributions that require several years to reach equilibrium. The resulting thickness distributions produced by this simplified approach resemble those of the more complicated formulations. Further work by Thorndike (2000) reaffirms that a simpler form of ψ will reproduce the general distribution and explains the negative exponential form of the thickness distribution as the result of a repetition of thin ice piling on thicker ice with decreasing probability for increasing thickness.

2.3. Ice area evolution models

Ice draft redistribution (IDR) models are not the only types of sea ice evolution models currently used by researchers. A comprehensive review by Savage (2001) for the Canadian Ice Service focuses on a different class of sea ice models referred to here as ice area evolution (IAE) models. In brief, while IDR models follow the evolution of the sea ice thickness distribution, an IAE model tracks the evolution of the mean thickness and area fraction of several distinct ice types. Both model types contain information about the mean thickness of ice and amount of ridged ice, but only the redistribution model includes the information about the shape and size of the created ridges.

The premise of an IAE model, that the mean thickness of the ice is tracked rather than the entire thickness distribution, simplifies the computational requirements. Initial models (e.g. Shulkes

1995) tracked the mean thickness and area fraction of both level and ridged ice categories providing information on the concentration of ice-covered waters in a region (or the area percentage covered with ice) and the amount of ridged ice. Further enhancements led to the five-category model of Haapala (2000) that tracks the mean thickness and area fractions of lead, level, rubble, rafted, and ridged ice categories.

The Canadian Ice Service and other sea ice forecast communities are interested in predicting ice thickness and concentration for shipping routes and thus much of the detail in the form of the IDR model is not of use to those communities. For this reason, IAE models have been incorporated in the Canadian Ice Service predictive model. For other sea ice research and applications, the physical shape of the ridged ice redistribution can be of importance. In climate models, the distribution of ridged ice into different thickness categories may affect the melt rates of ridged sea ice, the drag of ridged ice on currents and winds, and the strength of the ridged ice components. Predictions of extreme keel events for offshore construction also rely on accurate thickness distributions of ridged ice. It is necessary for these reasons that an understanding of the physical processes affecting the redistribution of sea ice is obtained and included in Arctic ice evolution models suggesting that IDR models may be more appropriate.

Savage (2001) noted that the underlying physics in redistribution models based on Thorndike et al (1975) has changed little in the past 25 years. He states that they "contain a significant amount of empiricism in the formulation of the redistribution mechanics that is both arbitrary to some degree, and difficult to verify" (Savage, 2001). Some researchers have used this as reasoning to exclude a physical representation of the formation of ridges altogether in favour of the simpler IAE models. While this approximation may be adequate for some purposes, I suggest that a physical representation of ridge formation is necessary in order to gain an estimate of the distribution of the thickness of ridged ice, to understand the physical factors influencing sea ice thickness, and to appropriately represent the ridged ice formed through a season. Through the development of a regional ice draft redistribution model, a new regional scale evaluation of the underlying physics affecting the draft distribution of sea ice has the potential to update IDR models for more accurate application to a variety of research problems.

SECTION B: THE WINTER REDISTRIBUTION OF SEA ICE IN THE BEAUFORT

3. APPLICATION TO THE BEAUFORT SEA

3.1. Geographic location

The Beaufort Sea (Figure 3-1) is an excellent location for studies of the redistribution of coastal sea ice. Normal circulation in the region is anti-cyclonic and the sea is bounded by land and land fast ice to the south and east. In average years, the sea is covered with first and multi year ice except for August and September (Figure 3-2) when marginal seas offshore become ice free due to easterly winds in early summer (Melling and Riedel, 1996b). This allows for the development of new level ice at the time of freeze up providing a natural experimental situation for the tracking of the development of first year level ice to ridged multi year ice. Further, during the winter, a large broad flaw leads open at the edge of the land fast ice due to storm events (Melling and Riedel, 1995; Melling and Riedel, 1996) which forms new level ice fields at varying times through the season. Ice motion in this area is largely divergent (Colony and Thorndike, 1984) such that new ice formed in the flaw lead should move offshore. Perhaps due to the offshore divergence and continued ridging, ice tends to be more heavily ridged further offshore (Melling and Riedel, 1996).

Exceptions to the normal summer ice circulation have occurred periodically (eight times from 1954-1991, Melling and Riedel, 1996b) where seasonal anomalies in atmospheric circulation have led to northerly winds reversing the anti-cyclonic circulation of the Beaufort Sea and closing the open water. This causes larger ice concentrations in the summer months and potential shipping difficulties (Melling and Riedel, 1996b). This change in circulation pattern also allows ice import from the northwest coast of the Canadian Arctic Archipelago, which is a region subject to high ridging, and thus increases the largest draft of ridge features observed in these years. Observations of ice in the Arctic show large inter-annual variability (Venegas and Mysak, 2000), which is often attributed to the ten-year period of the Arctic Oscillation (Flato, 1995). Of regional interest, some of the largest variations are often observed and predicted (Flato, 1995) in the Canadian waters of the Beaufort Sea with great impact on shipping and supply delivery for northern communities (Melling and Riedel, 1996b).

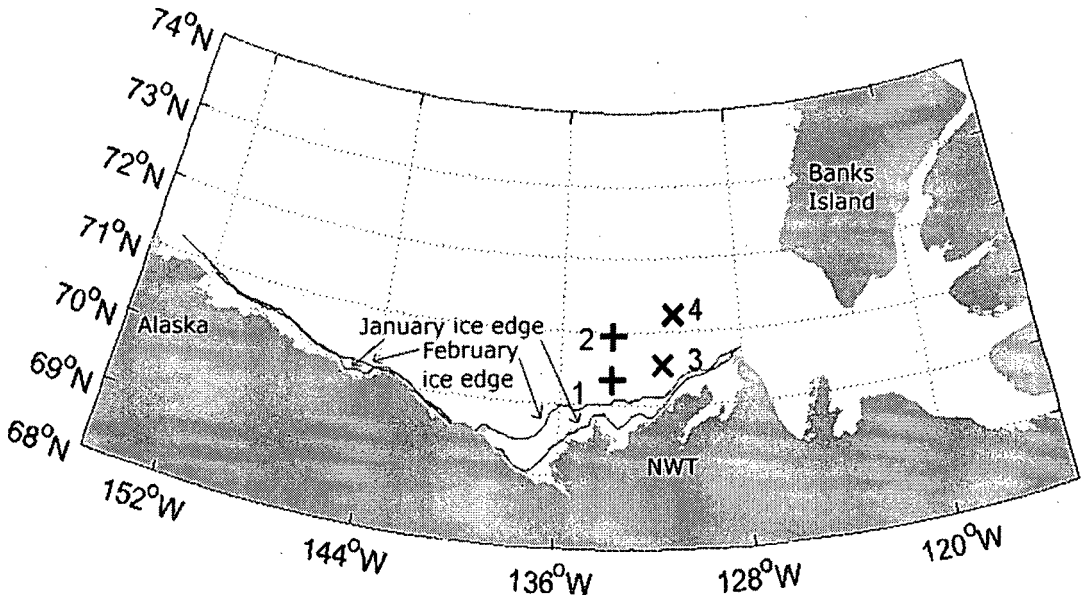

Figure 3-1: The Beaufort Sea area of the Canadian Basin. Mooring sites in the Beaufort Sea and the land-fast ice edge in January and February 1998 (from Regional Ice Chart, CIS). Ice data were acquired at Sites 1 and 2 during 1997-1998 and at Site 3 during 1991-1992. All four sites are located north of the land fast ice and the recurring flaw lead at the fast ice edge.

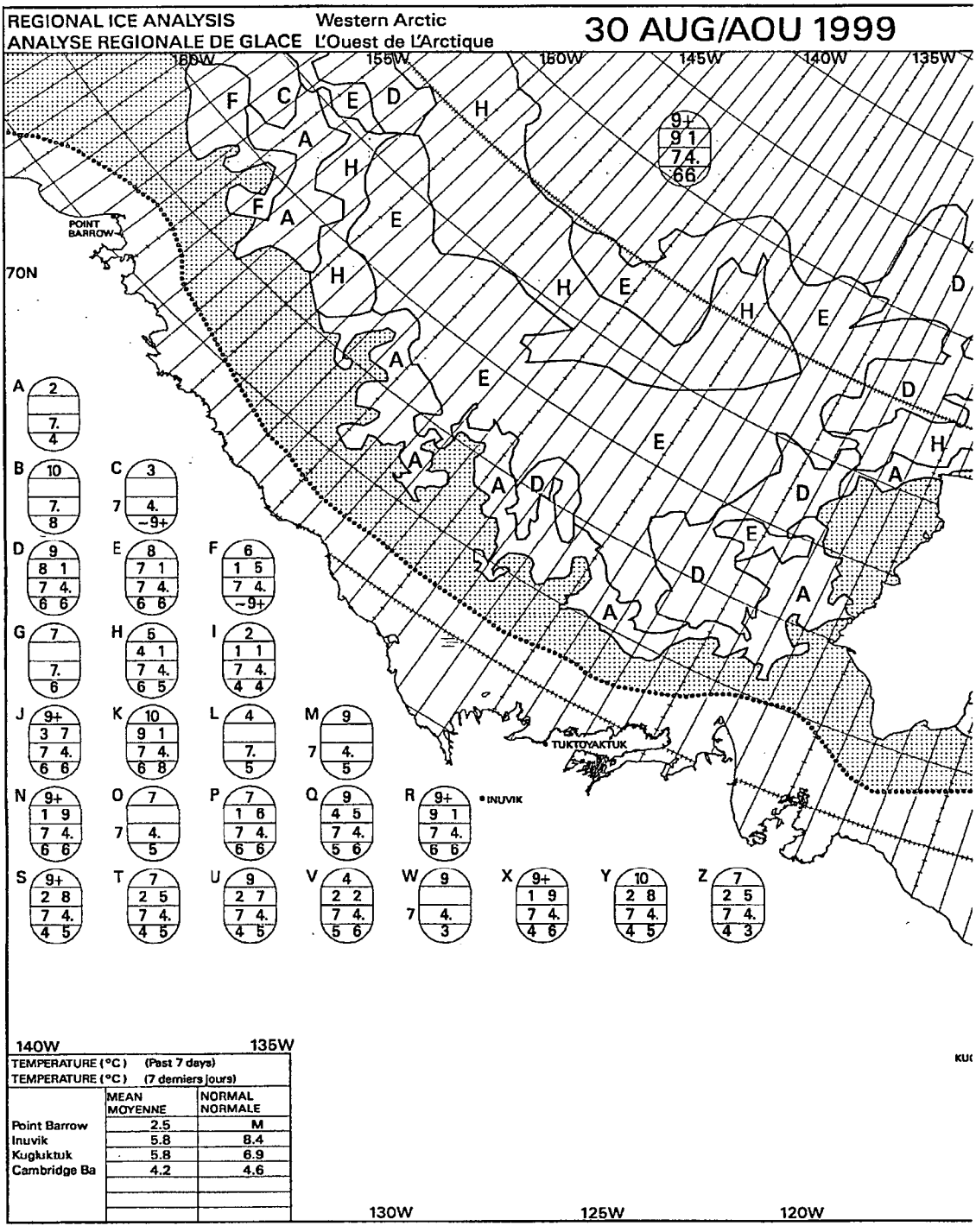

Figure 3-2: Partial ice chart for the Western Canadian Arctic on August 30th, 1999 from the Canadian Ice Service. The dotted area indicates the open water with less than 10% ice concentration while areas closer to the shore contains bergy water where total ice concentration is less than 10% cover.

3.2. Available data from moorings

To determine the evolution of sea ice on a scale of hundreds of kilometres, a tool such as undersea sonar offers general profiles of the thickness of the sea ice and ridge distributions for a region. Upward looking sonar on nuclear submarines has been utilized for several decades. This technique allows for spatial coverage of a region but requires multiple trips for temporal evolution and can be limited by shallow waters and political boundaries. To complement submarine data, upward looking sonars moored to the sea floor can provide ice draft profiles. This combines temporal and spatial coverage with the stationary sonar viewing new areas of ice due to pack movement. While this dependence on natural ice motion provides irregular spatial sampling intervals, the long time records allow for temporal evolution of a region's level and ridged ice distribution. Central to the ability to measure spatial distributions is the ice velocity, which allows for the mapping of draft values into a pseudo-spatial co-ordinate. It also provides valuable information on the recent kinematic history of the pack, particularly in relation to place of origin and interactions with the flaw lead and stamukhi zone to the south and east of the mooring sites. This is obtained with an acoustic Doppler current profiler (ADCP) used in tandem with an ice profiling sonar (IPS) to provide velocity and thickness data as described in detail in Melling et al., (1995) and Melling and Riedel (1994).

The moored IPS approach provides a better representation of the thickness distribution than other experimental techniques. Aircraft or satellite mounted sensors record only the profiles of above water ice, which consists of only 10% of the actual volume of ice (from buoyancy). The low sail to keel height and width ratios (Table 1-2) and the possibility for snowdrifts to conceal the true thickness distribution also suggest that measurements of the thickness distribution must take an "upwards-looking" approach. The method of electromagnetic induction, where the difference in conductivity between air and seawater can be utilized to determine ice thickness, does provide a "downward-looking" approach (Melling et al., 1995). Yet electromagnetic induction requires surveys by small planes, which is a costly and time-consuming way of obtaining the evolution of the sea ice draft distribution through a season.

A moored IPS transmits an acoustic pulse upwards and identifies the echo associated with the bottom of the ice or air-water interface. The IPS field of view from 50-m depth is approximately 0.8 m across (Melling, 1998b), small enough to have negligible effect in 'blurring' the

topography of keels that are tens of metres in width. The sonar detects the envelope of first returns, which in general defines the outline of a volume that may be as little as 70% ice (Melling et al., 1993). The travel time between the pulse and echo combined with data from tilt, pressure, and temperature sensors determines the draft of the ice. Challenges in determining the draft of the ice and extensive details of this instrument can be found in Melling and Riedel (1994).

The accuracy of the draft of sea ice determined by an upwards-looking IPS is sufficient to discern the changing draft of sea ice. The varying speed of sound in water throughout the year, due to seasonal changes in the water properties (Figure 1-4), can introduce errors in the calculated thickness of up to 0.2 m. However, calibration relative to open water data decreases this error to ± 0.02 m. The total error in the draft determination is approximately ± 0.05 m (Melling et al., 1995). Confidence limits for draft increase under compact ice conditions, whereas open ice conditions have a detrimental impact on confidence limits for velocity. As the ice evolution model in this thesis has a resolution of 10 cm, this accuracy is sufficient to provide excellent data for both model initial conditions and validation.

Measuring the velocity and direction in a water column is the often-used application of commercial ADCPs. The ice-water interface is a very strong target for the sonar similar to the signals obtained from the seafloor in ship mounted ADCP applications. The nominal accuracy of the Doppler velocities obtained in the data used in this thesis is ± 0.7 cm s^{-1} (Melling and Riedel, 1994).

While the resolution and nominal precision of the ADCP data is given as 0.25 cm $s^{-1}$and 0.7 cm s^{-1} respectively, additional error sources must be considered. The magnitude of the error introduced into the measured speed by the assumption of a constant speed of sound in the water column above the mooring is less than 0.5% and thus not a concern. The dominant source of uncertainty in the velocity determination is due to the error in measuring the Doppler shift, which was estimated as 0.01 m s^{-1} in each component for the ADCP used. Achieving this level of accuracy in the field was not always possible due to lowered signal-to-noise ratios, and an estimated error of ± 1 cm s^{-1} is reasonable.

Errors in the direction of the ice motion are also quantifiable. Due to the location of the moorings relatively near the magnetic north pole, the ADCP compass must be specially calibrated in a high latitude nonmagnetic enclosure (at Tuktoyaktuk, NWT; Melling et al., 1995), which reduces the error in the ADCP heading to a random error of ± 2 degrees. Additionally, sampling errors in each component of velocity contribute additional uncertainty independent of speed, leading to larger errors in low-speed drift (± 8 degrees at ice speeds of 0.05 m s^{-1}; Melling et al., 1995).

An eleven-year data set of ice draft profiles in the Beaufort Sea from moored subsea ice profiling and acoustic Doppler sonar is available and provides a rich data resource. Processing of the data was completed by David Riedel and Humfrey Melling (IOS, DFO, Sidney, BC) and provided to T. Amundrud for this thesis. A full discussion of the methods used for data processing can be found in the technical report by Melling and Riedel (1994). Of note to this research is the distinction that the ice evolution is sampled in time rather than space. For a thickness distribution to be constructed, the ice draft from the IPS must first be resampled in the spatial domain using the ADCP velocity record. Sufficiently long sections of the draft profile to allow for statistical reliability can then be used to produce ice draft distributions (Melling and Riedel, 1994).

The determination of the processes involved with summer ice degradation may only be partially elucidated by the draft profile record. The profiles provide no data on the consolidated layer depth, the ridge porosity, and characteristics of the water column below the ice. This limits the ability of the data to identify mechanical erosion and repacking events that respectively remove ice mass or conserve mass while decreasing porosity.

While the eleven-year data set provides much information about the sea ice draft at one location in the Beaufort Sea, the natural movement of ice past the moorings can lead to little insight on the evolution of a Lagrangian parcel (on the order of 100 km) of ice. Draft distributions through the Beaufort Sea are not homogeneous (as observed in the data). Ice can be formed locally in leads and polynyas, which introduces differing level ice types into a small parcel of ice. It becomes important to thus identify instances where a Lagrangian parcel of ice is viewed multiple times by the mooring such that the data provides a natural experiment where the temporal evolution of the ice can be determined.

3.3. Natural experiments

Wintertime ice drift in the southeastern Beaufort Sea follows a repeating sequence with three phases. In the first phase the pack may be almost or completely motionless for prolonged periods. Ice draft measured during these periods may be used to evaluate freezing algorithms in an IDR model. The first phase ends when strong easterly winds force the ice pack to the west-north-west, a heading with an offshore component in the area of study (Figure 3-1). Westward movement opens a wide flaw lead at the edge of fast ice (which is aligned in an east-west direction, Figure 3-3) and narrow leads within the drifting pack. Because open areas freeze rapidly under wintertime conditions, expanses of young weak ice form quickly. Northwesterly winds initiate the third phase in the sequence, pushing thick seasonal and perennial ice southward toward the coast to the accompaniment of heavy ridging of younger ice.

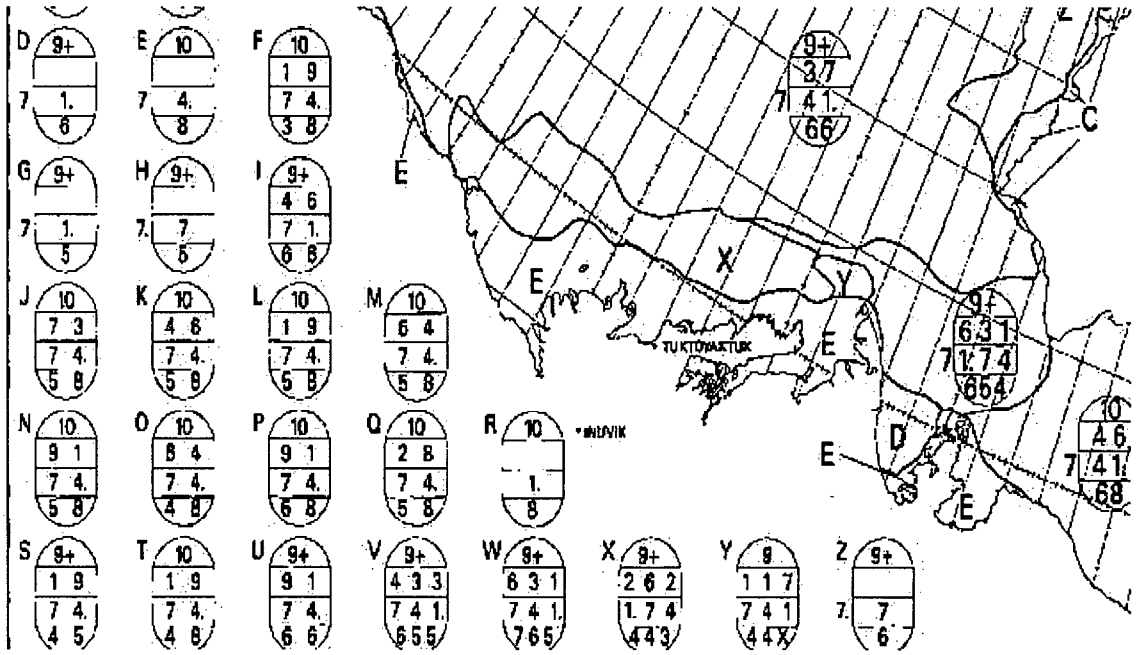

Figure 3-3: February 1st 1998 ice cover. The land fast ice is visible as area 'E' in this plot, the offshore ice in section 'X' is assumed to be homogeneous in an alongshore direction. The flaw lead is at the boundary between areas 'E' and 'X' but is not visible in the ice chart. Partial Ice Chart, Canadian Ice Service.

During the two active phases, an area of pack ice might possibly be driven landward then seaward along the same trajectory such that the same ice could be measured by sonar before and after the building of ridges. However, in general, our analysis is reliant upon the banded structure of the ice field that is established by the cyclic opening and closing of the flaw lead (Melling, 1998a). The nascent band is the flaw lead itself, a strip 10-20 km in width and 200 km in length, from the moorings at 134° W to Cape Bathurst in the northeast. The lead freezes over to form an alongshore band of uniform ice, typically located inshore of the bands from previous openings, which may have been ridged during prior events of convergence (Melling, 1998a). With the saw-toothed movement of the pack (onshore and offshore motion superimposed on the general westward drift, Figure 3-4), ice moving back over the mooring was formed further to the east, but within the same alongshore band as that initially viewed. We assume that the properties of ice bands are homogeneous in the alongshore direction, by virtue of identical age and deformation history. The critical 200-km length of the flaw lead in conjunction with westward average ice drift imposes an upper limit to the interval over which the assumption of alongshore homogeneity is valid.

There were three events during the winter of 1997-98 when an ice band was compressed against the land-fast ice, ridged and then blown offshore to be re-observed by the sonar at Site 2. This data set is particularly suited for verifying the mechanical ridging portion of the ice draft redistribution model because a separate data set is available from the mooring at site 1 located 70 km to the south (Figure 3-1). The first of these events occurred during January and early February 1998, and ice drift is indicated on Figure 3-4. Ice draft distributions were calculated from observations accumulated over approximately 50 km of ice at irregular intervals in time. The difference in north-south ice speed between the sites is the local north-south convergent rate of strain in the pack. Because the land-fast ice is close to the moorings and has an east-west orientation, the principal stress causing ice failure will be that resulting from north-south convergent strain. Ice movements in the east-west direction are not tightly constrained by land-fast ice or coastline.

The observed thermal growth of level-ice modes provides guidance in the selection of events for analysis of ice draft redistribution. At Site 2 during the winter of 1997-1998 the sonar tracked progressive growth of level ice only until the 65th day of 1998 (6 March; Figure 3-5). Because our

thermal growth model matches the observations until this date (Bellchamber-Amundrud, et al., 2002), we are confident that the assumption of alongshore homogeneity is valid. The subsequent thinning of level ice despite winter conditions indicates that a different population of ice has drifted over the mooring. Among the three events of high strain rate in 1997-1998, only the first ice motion event from days 9 to 32 of 1998 (Figure 3-5, 9th January to the 1st February) occurred while level ice was thickening as predicted via numerical simulation.

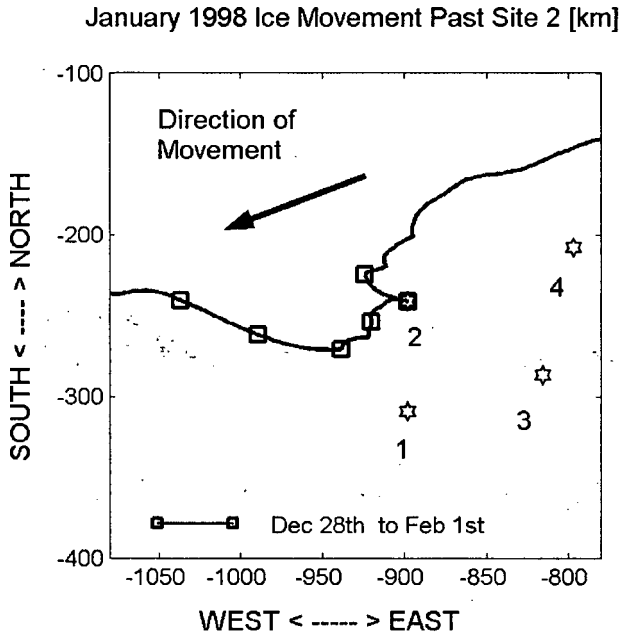

Figure 3-4: Eulerian displacement vector illustrating ice drift at Site 2 from December 28th, 1997 to February 1st, 1998. Stars indicate relative positions of moorings on December 28th. Squares mark the endpoints of track segments used to calculate distributions of draft.

Figure 3-5 clearly illustrates that the ice seen by the mooring throughout the winter is not all of the same age. How valid is it at any time to assume that the ice passing the mooring over a period of time is homogeneous and has grown under the same thermal conditions? Figure 3-6 shows the evolution of the probability density distribution from days 300 to days 461 during the winter 1991-1992. Similar to the winter of 1997-1998 (Figure 3-5) the inconsistent draft of the level ice peak after day 380 of 1991-1992 is visible in this plot of the evolution of draft distribution. Further discussion of the applicability of the data for comparison and validation of the modelled ice evolution will be discussed in chapter 4.2.

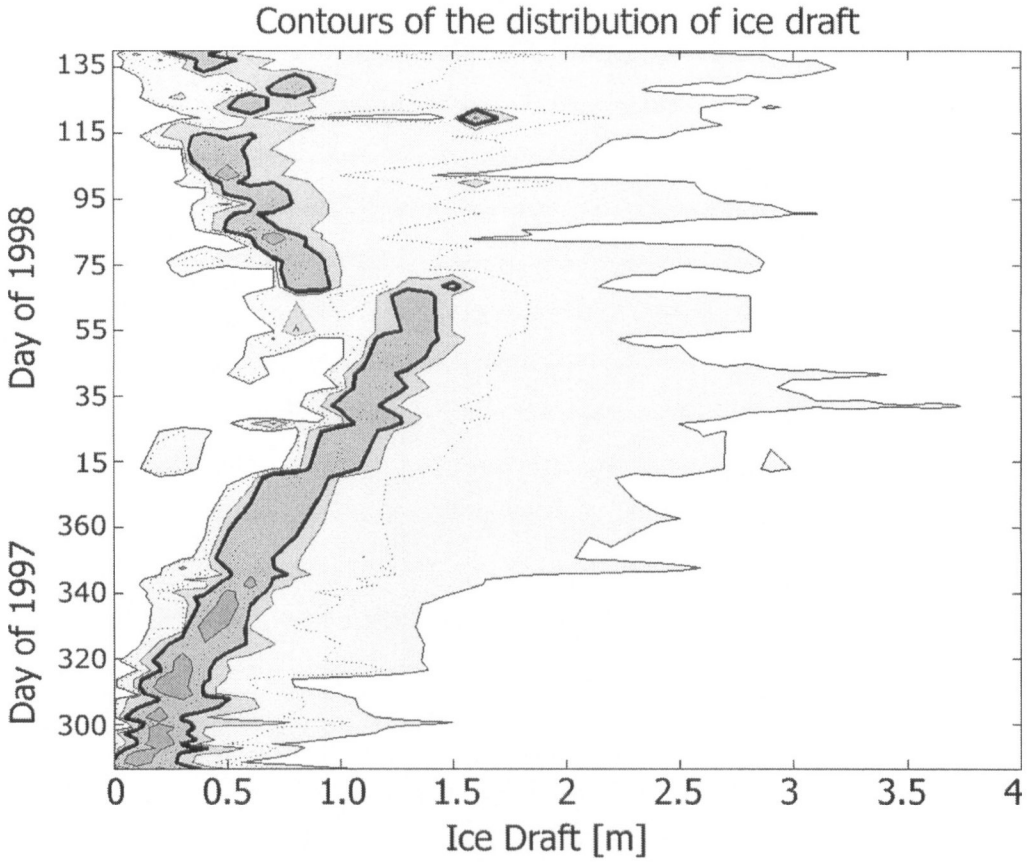

Figure 3-5: Evolution of ice thickness during the winter of 1997-1998 at site 2. Contours showing the discontinuity in level ice thickness. Progressively darker shaded regions contain 1, 5, 10 and 30% of the distribution (heavy black line is the 10% contour). The break in the seasonal level-ice mode is evident at Day 65 of 1998. Later level-ice modes track ice formed at other locations or at times after freeze up.

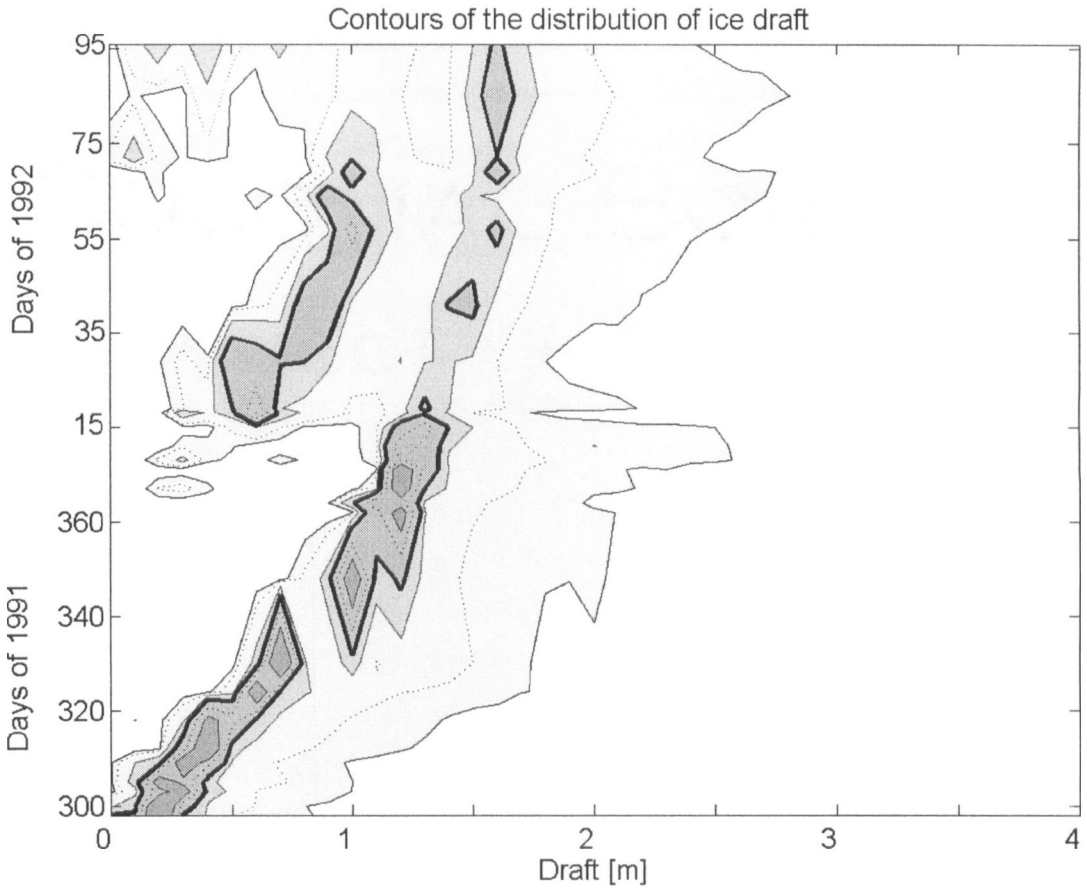

Figure 3-6: Eulerian versus Lagrangian ice perspectives. Contours showing the discontinuity in level ice thickness. Progressively darker shaded regions contain 1, 5, 10 and 30% of the distribution (heavy black line is the 10% contour). The inconsistent thermal growth of the level ice peak in a section of 1991-1992 data indicates that care must be taken in drawing conclusions from natural experiments.

4. A REGIONAL ICE DRAFT REDISTRIBUTION MODEL

4.1. General model

We begin with the general equation for the evolution of the thickness distribution, *g(h)* (Thorndike et. al., 1975):

$$\frac{\partial g}{\partial t} = -\nabla \cdot (\vec{u} g) - \frac{\partial}{\partial h}(fg) + \psi \qquad (4.1.1)$$

Here, the first term accounts for divergence of ice, the second for the thermal growth of the ice, and the third for mechanical redistribution. Equation (4.1.1) evolves the thickness distribution, however, embedded within the terms on the right hand side are conservation of ice mass and volume equations.

Thorndike (1992) has expressed (4.1.1) in discrete form, where the thickness distribution is defined as the distribution of ice within bins of equal increment in thickness, dh, represented by the vector G. The evolution of G with each time step, Δt, is expressed as:

$$\frac{G_{t+1} - G_t}{\Delta t} = [-divI + F + \Psi]G_t + divS \qquad (4.1.2)$$

where $divI$, F, and Ψ are the matrices representing divergence, thermal growth, and mechanical ridging, respectively. The time step Δt has been set to one hour, an approximation of the time required to build a small ridge. At a typical rate of strain (3% per day) 85 m of ice is consumed per hour, as the separation of moorings is 68 km. This is roughly the extent of the smallest floe participating in ridging (see chapter 5.3). A ridge may therefore be created in a single time step, but most ridges will require the accumulation of strain over several such steps. Model results are insensitive to increase of the time step to as long as 6 hours, which is the expected time for a ridge of maximum size to be created.

The matrix F, which controls the thermal evolution of ice thickness, is discussed in section 4.2. The matrix I is the identity matrix, which allows the thickness distribution to respond to the scalar value for the rate of divergence, div [s^{-1}]. In addition, a source vector, S, creates open water to

conserve area with convergent motion. The mechanical redistribution and divergence of the thickness distribution are discussed in section 4.3.

4.2. Thermodynamic ice growth

The change in ice thickness via thermal forcing is determined by the growth rate, $f(h)$, which varies with time. For each time step in the IDR model, $f(h)$ is calculated using the ice growth algorithms developed by Cavalieri and Martin (1994) and adapted to the observed increase in level ice draft in the Beaufort Sea by Melling and Riedel (1996) and forced by atmospheric data observed on the coast at Tuktoyaktuk (Canadian Climate Centre, Environment Canada). For the winter of 1997-1998, the growth rate is calculated assuming no oceanic heat flux and allowing the snow to accommodate 30% of the temperature difference between the ocean and the atmosphere. As the thermal conductivity of snow is 6-8 times smaller than the thermal conductivity of ice (Makshtas, 1998), the assumed snow thickness is less than 7% of the ice thickness, or 7 cm for 1 m ice.

Recent work (Lipscomb, 2001) has focused on the need for a new thermal growth algorithm that does not display the diffusive qualities (Figure 4-1) of traditional thermal growth redistribution methods (the Thorndike/Hibler approach; Thorndike et al., 1975; Thorndike, 1992; Hibler, 1980; and Flato and Hibler, 1995). Lipscomb's (2001) new remapping algorithm employs an additional tracked mean draft variable to reduce numerical diffusion of the sea ice draft distribution. Comparing the traditional Thorndike/Hibler thermal redistribution with the thermal remapping in a local redistribution model run with no mechanical forcing illustrates the effectiveness of the remapping algorithm in reducing diffusion of distribution peaks over short time scales.

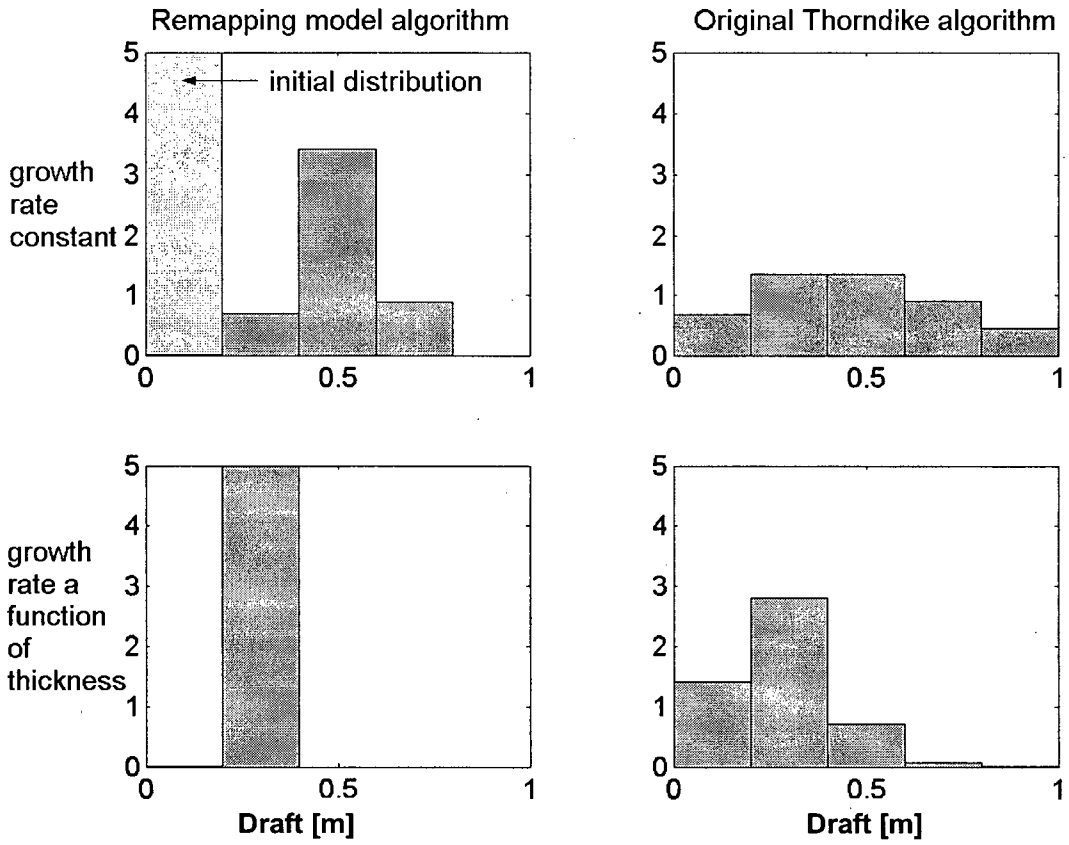

Figure 4-1: The Lipscomb (2001) remapping model algorithm (adapted from Lipscomb, 2001) applied to an assumed distribution function (note y-axis is the probability distribution of ice [m^{-1}]). The initial distribution is indicated in the upper left panel by the light grey bar. With a constant growth rate that does not change with ice thickness, the initial distribution grows to 0.5m and diffuses slightly. With the original Thorndike algorithm (upper right panel), the distribution spreads out over a range from 0 to 1m in draft. Using a growth rate that is dependent on ice thickness the Lipscomb remapping model grows ice to 0.25m in a sharp peak (lower left panel). The Thorndike algorithm grows ice to this height, but introduces significant diffusion (lower right panel).

The accurate observations of ice draft from the Beaufort Sea provide an excellent opportunity to evaluate the Lipscomb remapping algorithm using the IDR model. The mechanical forcing within the model is switched off by setting the strain rate to zero. Results from a run of the model for 17 October to 5 November 1997; when the rate of strain in the pack was weak, demonstrate the accuracy of the remapping algorithm (Figure 4-2a).

A second evaluation ran from freeze-up on 27 September to 20 November 1997. The observed and modeled ice-draft distributions have the same level ice peak (Figure 4-2b). Since the model was run without mechanical forcing to isolate thermal processes, there is no ridged ice in the modeled distribution at thickness greater than the 0.4-m level-ice peak. The obvious skill in simulating ice growth through freezing permits the change of the distribution of ice thickness associated with ridging to be isolated and independently simulated.

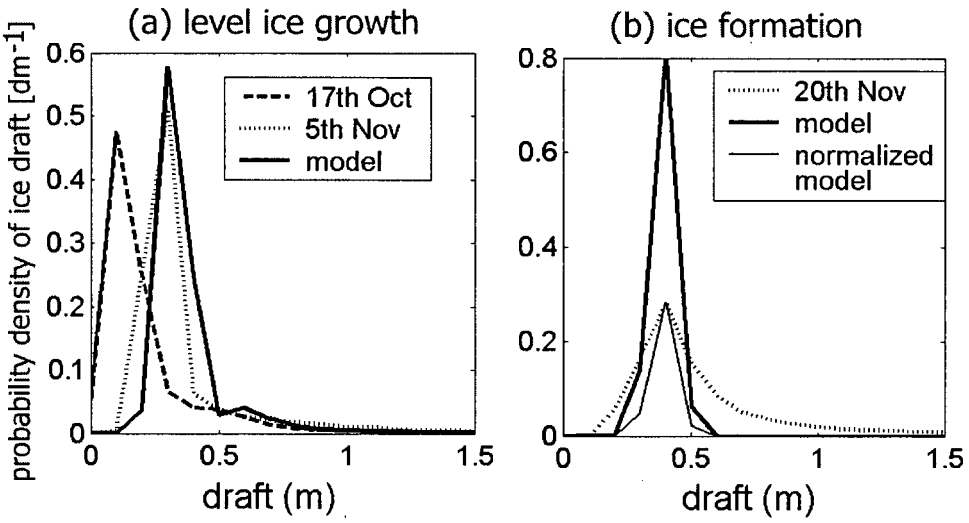

Figure 4-2: Observed and modeled probability density of draft (fraction per decimetre) for ice growing thermodynamically during the winter of 1997 at site 2. (a) Growth from conditions initialized using observations on 17 October. (b) Growth from an ice-free sea surface at the observed time of freeze-up. The model indicates more level ice than observations because mechanical redistribution is not active in these simulations.

Further evaluations of the ability of the thermodynamic component of the model are carried out using draft data from 1991. Figure 4-3 illustrates the improved performance of the Lipscomb scheme compared to the Thorndike/Hibler algorithm. Slight differences in the location of observed and modelled level ice peaks at day 348 may indicate small errors in the thermal growth rates or may be due to the comparison of Eulerian draft data with Lagrangian model output. Non-uniform growth of level ice throughout the winter season can be observed in the sonar data

indicating that the modal ice passing over the sonar may have been formed under slightly different conditions.

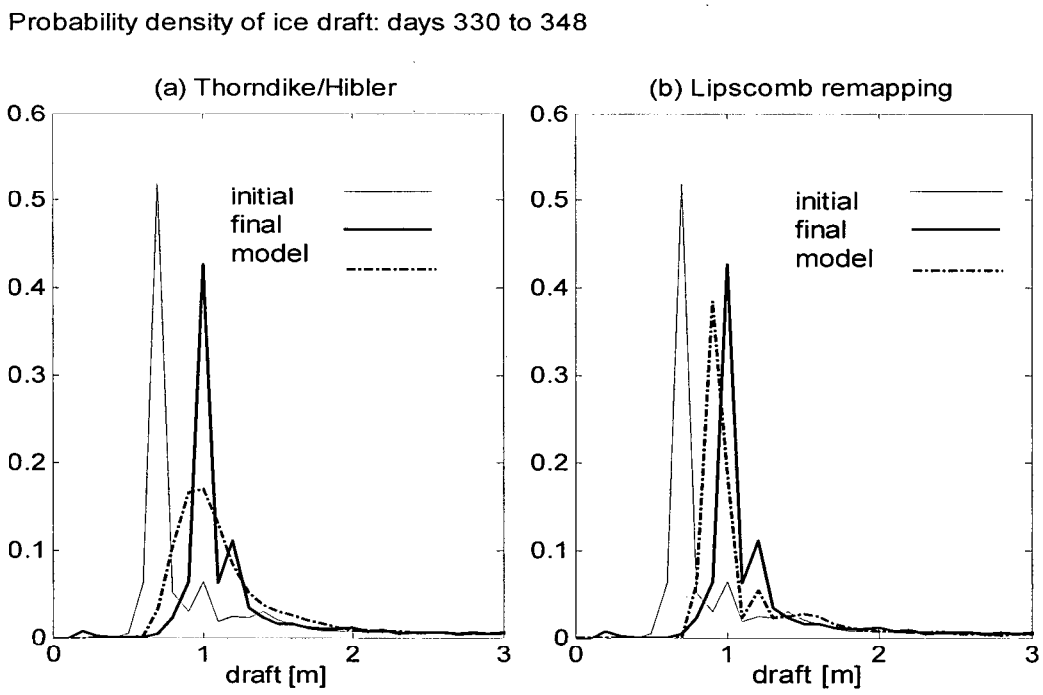

Figure 4-3: Results of the Thorndike/Hibler and Lipscomb thermal redistribution schemes (Lipscomb, 2001) on the final probability density distribution of sea-ice (fraction per decimetre). (a) Thorndike/Hibler approach. (b) Lipscomb approach.

Applying the redistribution model to the 1991 freeze-up season, the model is run from October 9th to November 26th beginning with open water and allowing divergence to continue to generate open water for new ice creation throughout the period. The 9th of October is chosen as the start of the simulation as there were no significant periods of possible ice growth observed in the meteorological forcing data from Tuktoyuktuk before this date. The observed and modelled sea ice draft distributions of November 26th match very closely (Figure 4-4). A slightly lower draft is observed for some of the level ice in the modelled distribution. This may be due to numerical diffusion or indicate that the thinner level ice is preferentially ridged.

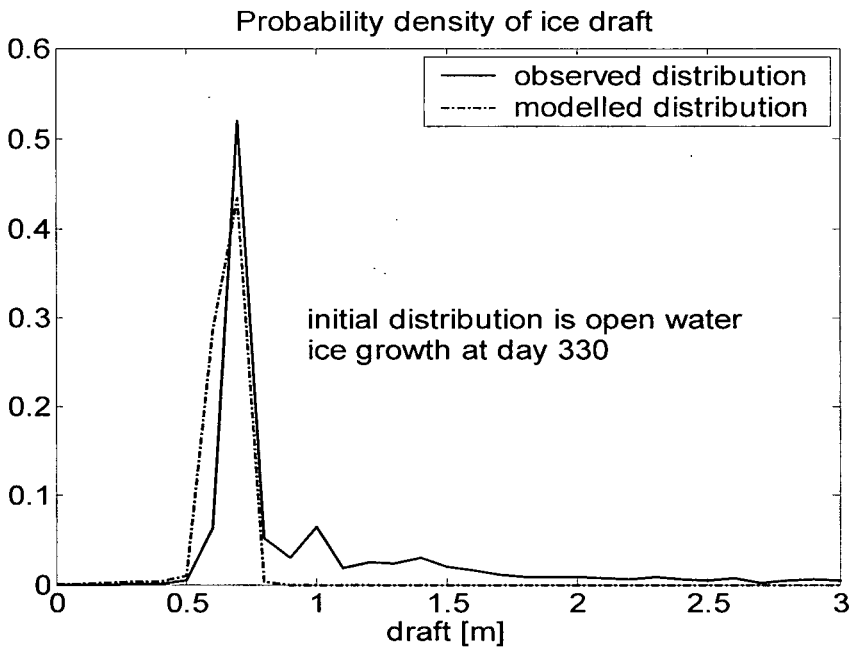

Figure 4-4: Modelled draft distribution and observed distributions on November 26th, 1991 (fraction per decimetre). The model does an excellent job recreating the level ice depth and shows little excess diffusion. Ice greater than the level ice peak is not present in the model distribution as rafting and ridging of ice was not permitted in this run.

4.3. Ice motion: divergence and ridging

We have adapted the ice thickness redistribution model of Thorndike (1992) to represent the ice draft observations in the Beaufort Sea. As the sonar was moored close to the edge of land-fast ice and because the pack is structured in shore-parallel bands of homogeneous ice, we assume that the component of motion perpendicular to the fast-ice edge is the dominant influence on the ice draft distribution. Ridging occurs in a two-dimensional world. Onshore displacements of the pack are convergent and re-distribute ice into ridges. Offshore displacements are divergent and create leads.

The rate of convergent strain was calculated from the difference in the offshore component of velocities measured at site 2 and site 1, about 70 km to the south. Because variance at frequencies exceeding 4 cycles per day was dominated by observational error, the time series of velocity were smoothed using a Butterworth filter with 6-h cut-off (see chapter 4.4). Episodes of prolonged compression and dilation of the ice cover were identified within a time series of uni-axial strain

rate. The divergent ice motion was incorporated into the model through the terms *–divI* and *divS*, where *div* is the divergent strain rate, set to zero during compressive motion.

Observations of open water by the ice-profiling sonar at site 2 provided an independent measure of recent local divergence. For the modelled ice motion event, the local measure of divergence was much smaller than the regional estimate (about 10%). We conclude that divergence was not uniformly distributed between the sites, but was concentrated at a large lead observed at site 1. The same scaling was not necessary during convergence; since the large lead moved rapidly south of site 1 where new ridging within it was no longer incorporated in the convergence calculated from velocities at sites 1 and 2. This is discussed further in chapter 6.5.

Compressive strain causes mechanical deformation. The matrix $\Psi(i,j)$ acts to distribute ice into ridges in proportion to the compressive strain rate, $\dot{\varepsilon}$ by taking ice from bin j and putting it into bin i. This matrix takes the form:

(4.3.1) $$\Psi_{0j} = a\dot{\varepsilon}$$

(4.3.2) $$\Psi_{jj} = -\dot{\varepsilon}$$

(4.3.3) $$\Psi_{ij} = pb(j)\dot{\varepsilon}, for\ 2(j-1)+1 < i < \beta(j)$$

Equation (4.3.2) is the participation term and acts to remove level ice from the categories participating in ridging. The participating ice, of draft h, is denoted in the matrix by the subscript j, where $h=(j\text{-}1)h^*$. h^* is the bin size or draft increment between elements of G. A 0.1-m value is used in this model, as the 95% confidence in the observations allows draft increments of this size in the observed distribution. In a Eulerian perspective, an ice-free area equivalent to the area of ice "lost" to ridging must appear during convergence.

The constant 'a' conserves area. On short time scales, 'a' is set to zero, implying that ice-free area created by local convergence appears somewhere else, likely far to the north, and is not measured by the sonar. In this approach, we do not conserve area, but instead re-normalize the thickness distribution at each time step.

The ice redistribution operator, Ψ, is applied over all participating level ice thicknesses, j, via a participation function that describes which level ice thicknesses participate in ridging. The participation function divides the amount of strain that is accommodated by ridging among the thickness bins judged to be level ice. Ice-free leads are closed first. Thorndike et al., (1975) and Hibler (1980) allow the thinnest 15% of ice to participate in ridging. They use a weighting coefficient that decreases linearly with increasing thickness, in order to ridge thinner ice preferentially. Thorndike (1992) argues that the appropriate range for participation is all ice thinner than the thermodynamic equilibrium. This assumption is used in the IDR model, implying that all level first-year ice is available for ridging. Thin ice is more likely to fail than thick ice since the buckling strength of a floating plate increases as the square of its thickness (see chapter 5.3). To approximate this sharply rising disincentive to ridging thicker floes, a participation function inversely proportional to thickness squared is applied to the strain rate $\dot{\varepsilon}$ over the range of ice draft participating in ridging.

The level ice "lost" during convergent motion is redistributed into thicker ice according to a transfer function, *b(j)*, where j is the index of the thickness bin wherein ridged ice is created. Traditionally *b(j)* is a constant, moving an equal area of ice into each ridged ice category. This implies that ice is piled into ridges of triangular cross-section and maximum possible draft (Figure 1-3). (Thorndike, 1992). The value of *b(j)* is chosen to conserve ice volume:

$$b(j) = \frac{j-1}{\sum_{i=2(j-1)+1}^{\beta(j)} i} \tag{4.3.4}$$

New ridges are poorly consolidated in most cases and have a high fraction (30%) of ice-free void space (e.g. Lepparanta et al., 1995). We multiply *b(j)* by a fixed factor, p, so that the volume occupied by the ridged ice exceeds the volume of ice within the ridge. This factor facilitates the comparison of model results to observations acquired by sonar that delineates the envelope of first returns from ridges. The inclusion of porosity does not change the geometries of the keels or the distribution of ridged ice, affecting only the proportion of ridged to level ice.

A further component of (4.3.3) is the range over which the transfer function is applied, here written as $2(j\text{-}1)+1 < i < \beta(j)$. Ice is ridged into a range of drafts that extends from double the draft of participating level ice (rafting) to some maximum possible ridge draft. Thorndike has defined the maximum to be a fixed multiple, k, of the participating level-ice thickness (Thorndike, et al., 1975; Thorndike, 1992) where k is the truncation factor. Hibler (1980) used a maximum thickness that is the product of the truncation factor and the square root of the thickness of participating level ice. Initially, we use the IDR model to examine the effect of a constant truncation factor, setting the maximum keel draft to 20 times the square root of the level ice participating such that $\beta(j) = 20\sqrt{(j-1)/h^*}$ (where h^* is the bin size, here 0.1 m, and j=1 is the open water category).

The transfer function and truncation factor control the shapes and dimensions of ridges and thereby are essential to a model's ability to reproduce observed thickness distributions for ridged ice. Failure of a model to replicate observations may imply incorrect formulation of these algorithms.

4.4. Observational errors

Observational errors in the probability draft distribution are calculated as outlined in Rothrock (1986) and depend on the decorrelation distance of the ice profile, which for all ridged ice can be found to be approximately 5 m, or 5 samples as the ice profile is in 1 m spatial increments. Thus the number of independent samples of ice, $\mathcal{N}(h)$, within a profile is $1/5^{th}$ the observed number of samples of ice at that draft range, h. Following from Rothrock (1986) and Melling and Riedel (1995), the percent error on the distribution for ridged ice is

$$\% \ error = \left[\frac{(1-g(h))}{g(h)\,L/5}\right]^{1/2} \tag{4.4.1}$$

where L is the total number of samples in the ice profile. For ridged ice, as $(1\text{-}g(h)) \sim 1$ and $g(h)L/5 \sim \mathcal{N}(h)$, (4.4.1) can be estimated as $\mathcal{N}^{-1/2}$.

The velocities used in the model to calculate the strain rate are smoothed using a Butterworth filter with 6-h cut-off. The power spectrum for the raw ice motion data at site 2 is shown in Figure 4-5. Visible in the spectrum is the semi-diurnal tidal signal. The noise due to the sampling

error ($\pm$ 1 cm s^{-1}) of the Doppler ADCP translates into a noise level in the power spectral density (Emery and Thomson, 1998) of approximately 5.28 x 10^4 cm^2 s^{-1} $cycles^{-1}$, which the spectrum crosses at approximately 4 cycles per day (~ 4.7 x 10^{-5} cycles s^{-1}). While the noise level would suggest using a six-hour filter, the validity of including tide-driven ice motion could also be questioned. Running the model with either a 6-hour or 24-hour cut-off for the Butterworth filter (Figure 4-6) makes no visible difference to the results, as the average strain over the period of the simulations does not change. The tidal oscillations are thus included in the model.

Total error in the strain rate, before smoothing velocities, is 0.02 day^{-1}. This signal is smaller than the strain rate at most times (except during periods of no motion) and, as velocities are smoothed before the strain is calculated, the error in the strain rate is expected to be small. Additionally, in the model, the mechanical forcing is a cumulative process, such that random errors in the strain and divergence should be smoothed further by temporal integration.

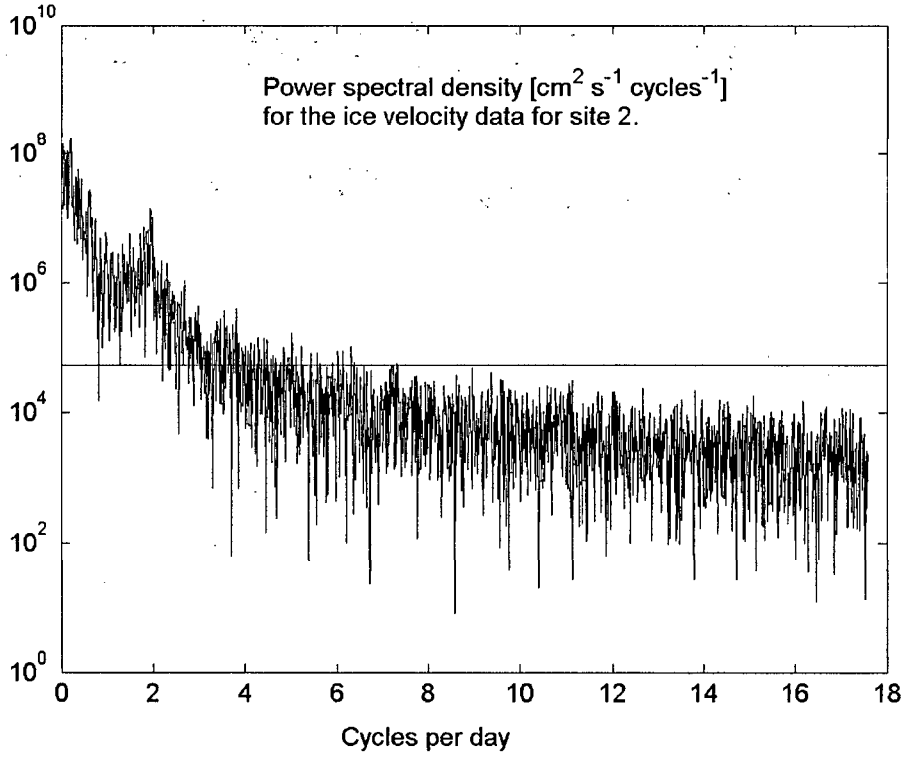

Figure 4-5: The power spectral density for the north-south ice velocity data at site 2 during the winter of 1997-1998. The semi-diurnal tidal peak is clearly visible. The horizontal line represents the noise level associated with the sampling error of 1 cm s^{-1}.

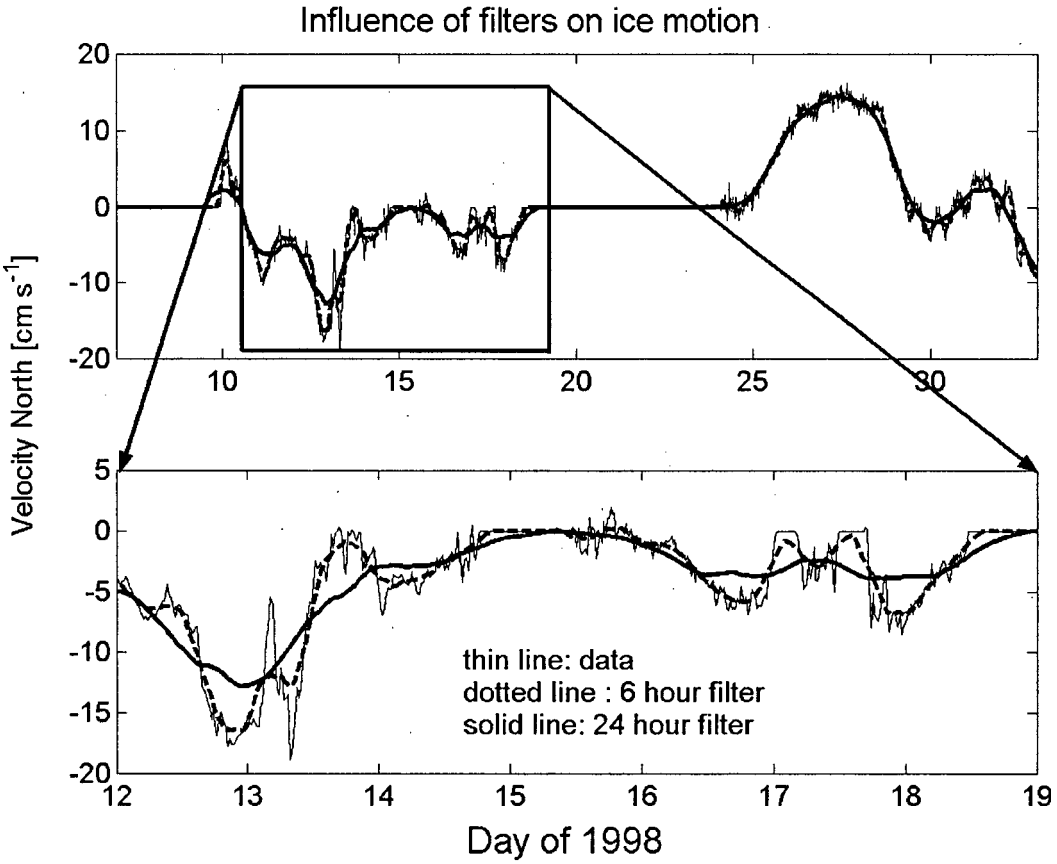

Figure 4-6: Influence of 24 (heavy solid line) and 6 (heavy dashed line) filters on the north-south ice velocity data from site 2. Lower panel is an expanded section of upper panel to clearly show daily oscillations in data.

SECTION C: GEOMETRIC CONSTRAINTS ON ICE RIDGING

5. CONTRIBUTION OF ICE FEATURES TO ICE EVOLUTION

5.1. Maximum keel draft

The IDR model was run for the period 9 January to 1 February 1998 using Thorndike's transfer function with $b(j)$ (4.3.3) a constant (Thorndike et. al., 1975; Hibler, 1989, Bitz et al., 2001, and Babko et al., 2002). This algorithm clearly apportions far too much ice into the thick end of the distribution (Figure 5-1) and too little into the 3-5m draft range. Confidence bounds on the constructed distribution from the observed ice pack represent one standard deviation due to sampling error and are calculated as described in chapter 4.4. A constant transfer function places an equal amount of ridged ice in each bin up to the maximum.

This comparison of model results with observations suggests that the constant values used for the transfer function and truncation factor embody inappropriate assumptions about keel shape and size. Here we explore the assumption concerning maximum keel draft as a source of the overestimate in the fraction of thick ridged ice.

There is a statistically significant truncation of the commonly observed exponential roll-off in the occurrence of ridged ice at large draft (Melling and Riedel, 1996a). The truncation has been ascribed to the finite strength of the level ice from which ridges are built (Melling and Riedel, 1996a; Hopkins, 1998). Hopkins (1998) asserts that the maximum height of a ridge sail is reached when the force needed to push another ice block beyond the top of the ridge exceeds the force that will buckle the level ice next to it. At this point a section of level ice will fail and contribute fragments either to widen the existing ridge or to begin construction of a new one.

Observations provide circumstantial evidence in support of Hopkins' (1998) argument (Melling and Riedel, 1996a). Adding recent data from almost a decade of ice-draft observations in the Beaufort Sea, a relationship between the maximum observed draft for ridges and the draft of level ice contributing to them can be established with some confidence. Figure 5-2 shows the draft of the deepest keel observed within each of approximately one thousand 50-km topographic transects versus the draft of the level ice adjacent to it. Note that because only the deepest keel of each transect has been plotted, most of the keel population is not represented. A plausible upper bound to the keel draft is 20 m $^{1/2}$ $h^{1/2}$, where h is the draft of the adjacent level ice. Hibler (1980)

and Hopkins (1994, 1998) proposed a similar truncation curve via geometrical arguments and via numerical simulations of ridging, respectively.

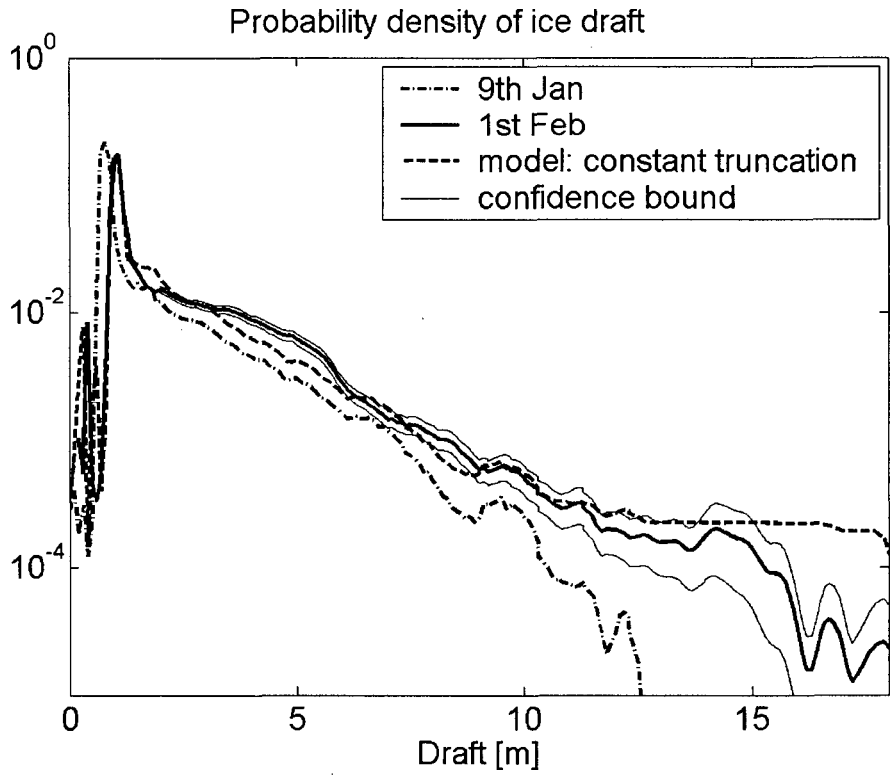

Figure 5-1: Probability density of draft (fraction per decimeter) from a model run with customary assumptions that all ridge keels are built to a draft of 20 $m^{1/2}$ $h^{1/2}$ and have triangular shape, for site 2 in 1998. Relative to observations, far too much ice of draft exceeding 10 m is created. Thin lines are confidence bounds representing +/- one standard sampling error based on degrees of freedom.

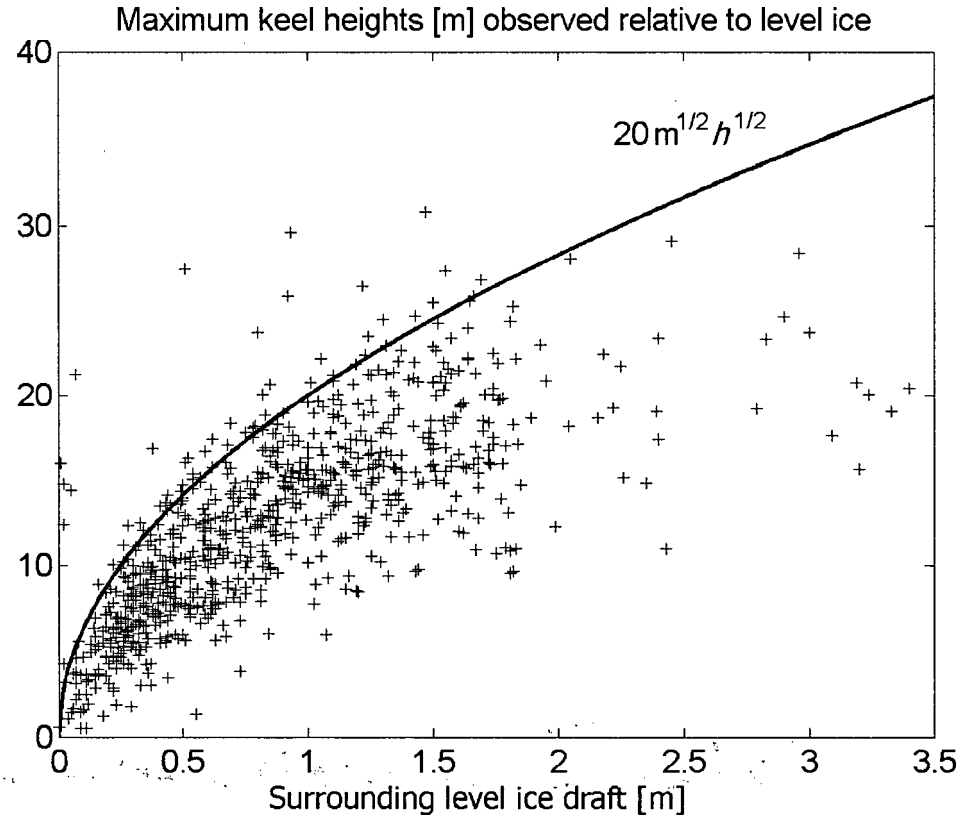

Figure 5-2: Empirical relationship between the draft of large keels and that of level ice adjacent to them, based on observations of seasonal pack in the Beaufort Sea during the 1990s. The curve indicates truncation of keel development at a draft of 20 $m^{1/2} h^{1/2}$.

Less than 4% of the data in Figure 5-2 lie above the truncation curve. These points could be associated with pinnacles on keels or could result from a mistaken identification of ice in a re-frozen crack near the ridge as material used in building it. They could perhaps be associated with ridges built from stronger multi year ice, although care was taken to disregard such features for this study of ridging in seasonal pack ice.

Many of even the biggest keels fall below or to the right of the curve representing the maximum. There are four possible explanations for such a shortfall. The ridge may be old, so that the adjacent level ice has grown thicker since it was fractured to build the ridge. All available thin ice may have been incorporated in the ridge, leaving only nearby thicker ice that is too strong to fail.

The keel may have lost draft since formation through mechanical collapse or melting. Finally, some constraint may have prevented the keel from ever growing to maximum draft.

5.2. Floe size and thickness

A ridge will develop to maximum size only if several conditions are met. First, there must be sufficient contiguous level ice to provide raw material for the ridge. Second, the stress developed by the action of wind and current must be sufficient to cause structural failure of the ice. Third, the critical stress must last long enough to complete building the ridge. In this section we explore the implication of finite floe size as a constraint on keel size.

Rapid sampling by sonar in this study has provided fully resolved topographic profiles of pack ice. The shapes and dimensions of keels and of level floes, along the direction of drift, can be readily determined. Level ice floes were identified using the criteria that the floes must be greater than 10 m in extent and vary by less than ±0.25 m in draft (Melling and Riedel, 1996a). Floes are delineated by expanses of appreciably thinner (refrozen or open leads) or thicker ice (ridges). Adjacent floes separated by less than 1 m with drafts within one standard deviation were merged, since a small piece of rubble separating floes is not expected to hinder ridging. Ice floes of draft exceeding the maximum growth for first-year ice at the time observed were not counted. In a final selection, only those floes sandwiched between thicker level ice capable of transmitting a critical stress for buckling were included. Ensembles of thin floes of differing draft, surrounded by thicker ice were considered a single expanse of ice with draft equal to the average over the ensemble.

If a ridge keel has a triangular cross-section of width, W, equal to four times the draft, H, (Timco and Burden, 1997), the extent of level ice needed to construct a ridge of maximum draft can be calculated by conserving cross-sectional area. In two dimensions, the area balance between floes of length f_L and draft h and a keel of draft H and porosity p will be:

$$f_L h = \frac{1}{2} HW(1-p) = 2H^2(1-p) \tag{5.2.1}$$

Substituting the relationship H=20 m$^{1/2}$ $h^{1/2}$ into (5.2.1), the minimum size of floe necessary to build a solid keel of maximum draft is 800 m, independent of level-ice draft. However, with a

porosity factor of 30%, typical of new ridges (Timco and Burden, 1997), at least 560-m of level ice is incorporated into a keel of maximum draft. Continued ridging of a wider floe would increase the keel's width, but not its draft (Hopkins, 1998).

Based on floe-size data from Sites 1 and 2 in 1997-1998 (Figure 5-3), approximately 25% of the floes are sufficiently large to form keels equal to the maximum size H=20 $m^{1/2} h^{1/2}$ controlled by buckling failure. Thus it is not a shortage of large expanses of level ice that cause the biggest keels to fall short of maximum draft.

On the other hand, 75% of the floes are too small to build a ridge of maximum size. Thus conventional redistribution models, which consider the supply of level ice to be unlimited, place too much ice in the categories of deepest draft. It follows that the draft of keels created by ridging in models should be constrained by the level ice available.

When re-arranged, (5.2.1) takes the form:

$$H = \left[\frac{f_L}{2(1-p)}\right]^{1/2} h^{1/2} \tag{5.2.2}$$

Which is analogous to the equation for the maximum possible draft of ridge keels, H=20 $m^{1/2} h^{1/2}$. We thus propose constraints on maximum keel draft dependent on both the 20 $m^{1/2} h^{1/2}$ restriction from ice strength and the $(f_L /2(1-p))^{1/2} h^{1/2}$ restriction from floe size.

A truncated lognormal function provides a good fit to the histogram of observed floe size (Figure 5-4) constructed from the floe sizes in Figure 5-3. Since our definition of level ice excludes floes less than 10 m across, the truncation value is 2.3. The histogram of floe size does not vary with draft over the range 1-1.3 m. The histogram also appears to be invariant for thicker floes, although it is sparsely populated by the data available.

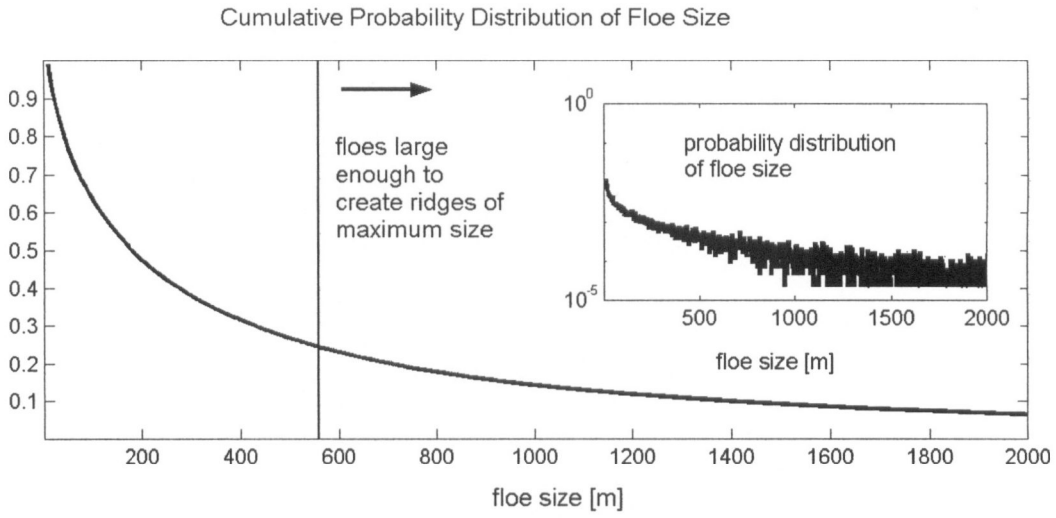

Figure 5-3: Cumulative distribution of floe size (fraction per floe size) in the Beaufort Sea during 1997-1998 at Sites 1 and 2. All floes larger than 560m are capable of forming a ridge of maximum size. Inset: probability density function of floe size (fraction per metre on a logarithmic scale).

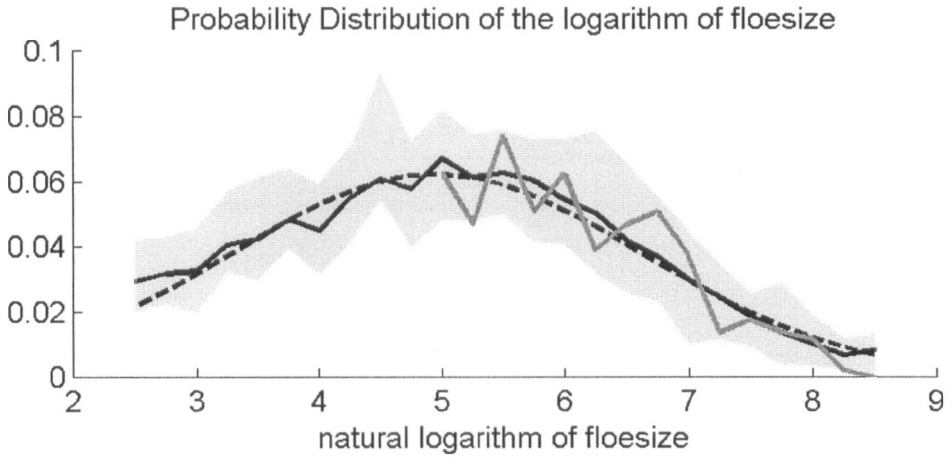

Figure 5-4: Probability density of the logarithm of floe size (in m) for all (0-1.3 m) drafts of level ice (solid line). The log-normal curve (dotted line) has a mean of 4.95 and a standard deviation of 1.7. The shaded area encompasses probability densities of floe size of specific draft by 0.1 m increment in the range 0-1.3 m. The gray line is the mean probability density of size for floes of 1.3-2.0 m draft. The truncation of data at a 10 m floe size reflects the minimum scale used in the definition of level ice.

5.3. Characteristic floe length in buckling

The mechanical failure of an ice floe in buckling is commonly modeled as the failure of an elastic plate (ice) floating on an elastic foundation (seawater) where buoyant forces are analogous to the elastic restoring force of a simple spring (Sanderson, 1988). In ridging, we assume that the ice floe is a rectangular plate and that the force is applied evenly over one edge of the plate. The bending energy of the plate and the energy stored in the buoyant foundation can be calculated (Den Hartog, 1952) and an expression for the critical buckling stress derived:

$$\sigma = \frac{E\pi^2(m^2+1)^2}{12(1-n^2)m^2}\frac{h^2}{f_L^2} + \frac{\rho_w \breve{g}}{m^2}\frac{f_L^2}{h} \tag{5.3.1}$$

Here E is Young's modulus, n is Poisson's ratio, ρ_w is the density of water, $\breve{g}$ is the gravitational acceleration (to avoid confusion with the probability distribution, $g(h)$), and m is a mode number ($m \geq 1$).

The minimum buckling stress for a fixed thickness occurs where $\partial\sigma/\partial f_L = 0$. The corresponding floe length is:

$$f_L{}^4 = \frac{E\pi^2(m^2+1)^2}{12(1-n^2)\rho_w \breve{g}} h^3 \tag{5.3.2}$$

The smallest size satisfying (5.3.2) occurs for m=1 when the floe buckles as a single arc. This is the characteristic length L_C,

$$L_c = \left[\frac{4E\pi^2 h^3}{12(1-n^2)\rho_w \breve{g}}\right]^{1/4} \tag{5.3.3}$$

Buckling of floes smaller than L_C is unlikely because the buckling stress varies in this range as the inverse square of floe size.

The minimum buckling stress, evaluated using (5.3.2) in (5.3.1) decreases with mode number.

$$\sigma = 2\pi\left(\frac{m^2+1}{m^2}\right)\sqrt{\frac{E\rho_w \breve{g}h}{12(1-n^2)}} \tag{5.3.4}$$

The lowest stress corresponds to the highest integral mode number satisfying $m^2 \leq 2\cdot(f_l/L_c)^2-1$. Equation (5.3.4) is equivalent to the buckling force for a beam derived by Kovacs and Sodhi (1980) and used in two-dimensional simulations by Hopkins (1998).

Equation (5.3.3) is greater than past derivations of the characteristic length (Hopkins, 1998) by a factor of $[4\pi^2/(1-n^2)]^{1/4}$ due to the formulation of buckling of the floe as a plate rather than a beam (Kovacs and Sodhi, 1980; Hopkins, 1998). Since the width of the ice floe is expected to add stability, the inclusion of this factor is appropriate.

The characteristic lengths for various thicknesses of ice can be calculated using estimates for Young's modulus and Poisson's ratio. Poisson's ratio for ice is often given as 0.3 (Hopkins, 1998, Fox and Squire, 1991). Estimates of Young's modulus range from 1 GPa to greater than 6 GPa (Hopkins, 1998; Fox and Squire, 1991; Dempsey et al., 1999). Sea ice is a complex, multiphase material near its melting point and traditional strength parameters such as E and n vary with temperature and salt content such that single definitive values for E and n cannot be assigned. For purposes of approximation, Young's Modulus is assumed to be 2 Gpa, as found by Fox et al., (2001) in Antarctic sea ice. Using these parameters, the critical buckling stress (5.3.1) for a level ice floe can be plotted for various floe sizes and mode numbers (Figure 5-5) illustrating the minimum buckling stress (5.3.4) needed to buckle the ice.

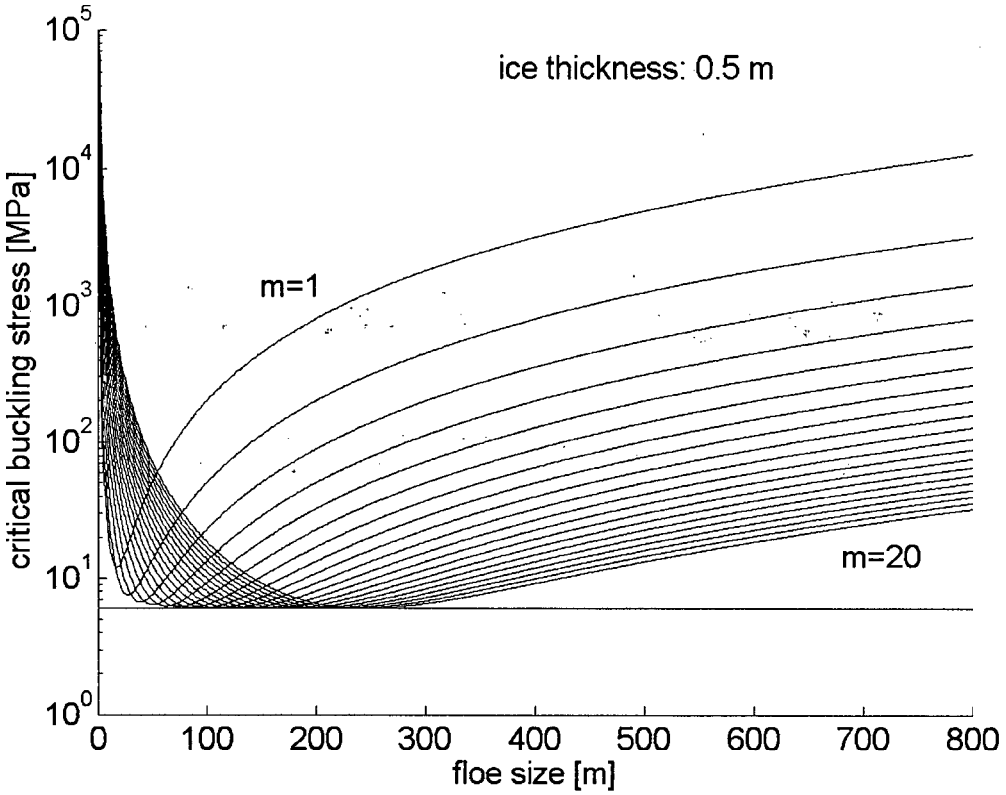

Figure 5-5: Critical buckling stress (in MPa) for a 0.5 m thick level ice floe, indicating the expected critical buckling stress for level ice (5.3.1). Visible is the minimum buckling stress (for floes larger than L_C, (5.3.4)) given as the solid horizontal line.

5.4. Truncation of ridge building via limits on ice available

We incorporate the limitation on raw material for ridge building into the IDR model via a stochastic approach. Initially, for each time step and for each bin of thickness that participates in ridging, the model randomly samples a floe size from the empirical lognormal distribution. The selected size is compared with the characteristic length for buckling for this thickness category. The selected floe size is not used if it is less than the characteristic length for a particular bin; replacement values are selected randomly from the floe-size distribution until a value large enough to buckle is obtained.

Ridging continues with this floe size in subsequent time steps until the entire extent of the floe has been consumed. At this point, a new floe size is chosen using the above criteria, and ridging

begins using this new floe size for a truncation constraint. This process is outlined in the flow chart in Figure 5-6.

The randomly selected floe size is mapped to a value for the truncation constant, β, where

$$\beta = \sqrt{\frac{f_L}{2(1-p)}} \tag{5.4.1}$$

and $H=\beta h^{1/2}$. Values of β from (5.4.1) that are greater than 20 $m^{1/2}$ are set equal to 20 $m^{1/2}$ to reflect the constraint of ice strength on keel draft.

Use of a keel-draft truncation factor based on floe size within the IDR model decreases the fraction of ice in the deep ridged categories. Results are displayed in Figure 5-7. The inclusion of the random selection of floe size introduces some variance between model runs. This is shown in Figure 5-7 on line d as one standard deviation from the mean after 500 simulations. The implementation of the floe size constraint on ridge building begins to decrease the amount of the deepest ridged ice for drafts exceeding 11m (Figure 5-7; line b). The improved concurrence of these modeling results with observations suggests that finite size of level floes may indeed influence the draft of large keels that develop in first-year pack ice.

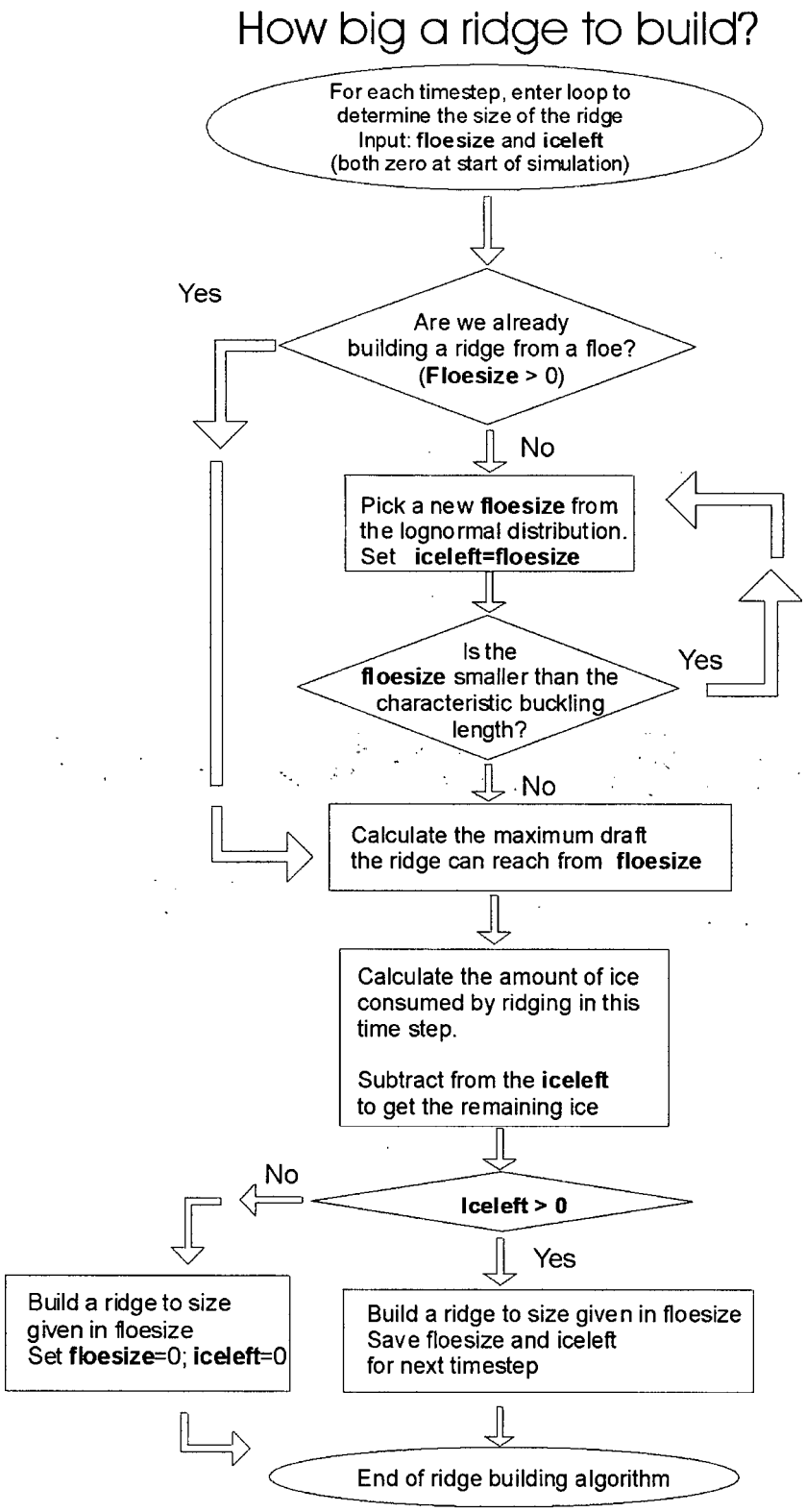
How big a ridge to build?
For each timestep, enter loop to determine the size of the ridge
Input: floesize and iceleft
(both zero at start of simulation)
Are we already building a ridge from a floe?
(Floesize > 0)
Yes
No
Pick a new floesize from the lognormal distribution.
Set iceleft=floesize
Is the floesize smaller than the characteristic buckling length?
Yes
No
Calculate the maximum draft the ridge can reach from floesize
Calculate the amount of ice consumed by ridging in this time step.
Subtract from the iceleft to get the remaining ice
Iceleft > 0
No
Yes
Build a ridge to size given in floesize
Set floesize=0; iceleft=0
Build a ridge to size given in floesize
Save floesize and iceleft for next timestep
End of ridge building algorithm

Figure 5-6: Flow chart illustrating the decision process for deciding the value of the floe size to be used in the truncation constraint (previous page).

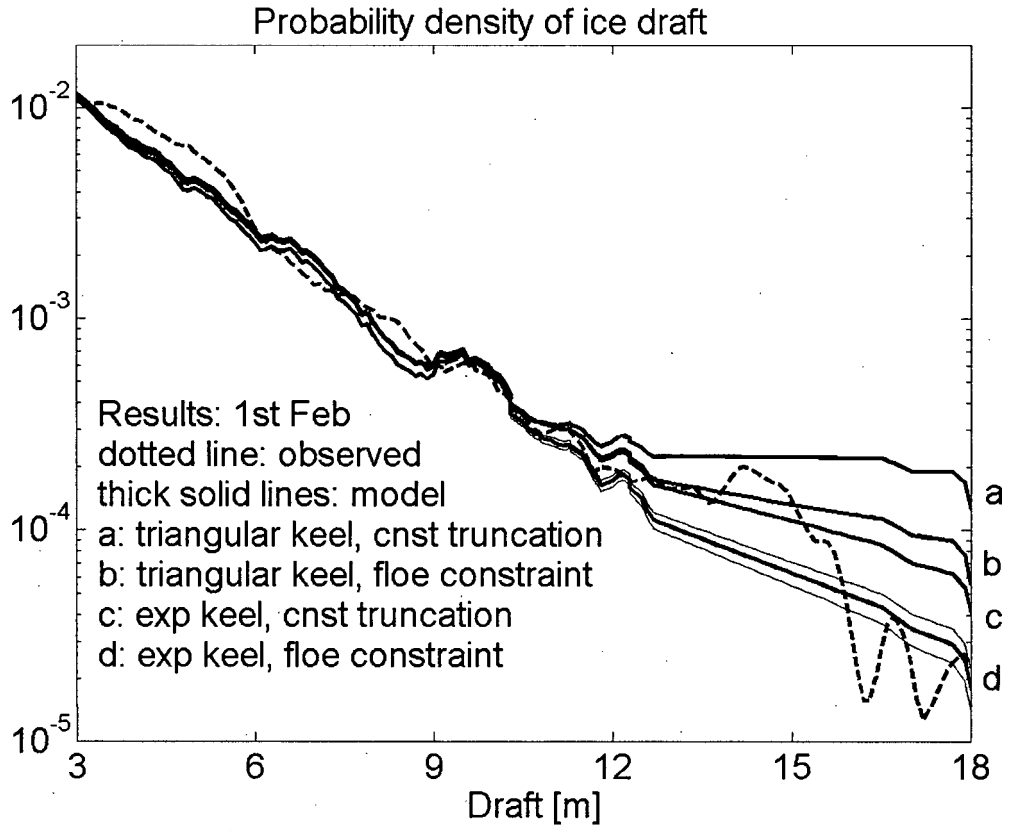

Figure 5-7: Mean probability density of draft (fraction per decimeter) for ridged ice calculated with various geometrical constraints on ice ridging. Model is run from the 9th January to the 1st of February 1998 at site 2. Comparative curves are shown smoothed with a 5-point running average for runs with (a) uniform volume distribution and a constant truncation (b) uniform volume distribution and the floe-availability constraint, (c) exponential (6-m scale) volume distribution and a constant truncation, and (d) exponential (6-m scale) volume distribution and the floe-availability constraint. Thin lines indicate the variation between 500 simulations using the floe availability constraint indicated as one standard deviation. Similar variation is found for curve (b).

5.5. Keel shape

Ice-thickness redistribution models commonly assume a constant value for the transfer function. This assumes that the cross-sectional shapes of ridge keels and sails are triangular. Melling and

Riedel (1995) noted that the empirical exponential form both of the probability density of ice draft and of the occurrence frequency for keel draft has implications for the average cross-sectional shape of keels. Assuming that width of a keel is proportional to its maximum draft and that its shape is independent of draft, then observations indicate that the probability density of draft within keels must on average also be exponential. Melling and Riedel (1995) found the average distribution of ice within 21 keels exceeding 20 m draft to be exponential with a 15-m e-folding scale. However, the shape of individual keels is extremely variable (Melling and Riedel, 1995; Timco and Burden, 1997; and Lepparanta and Hakala, 1992).

In an IDR model, the keel shape for features of all sizes is required, not just for the very large keels. To extend the shape analysis of Melling and Riedel (1995), keels surrounded by level ice were identified in the ice-draft profile for days 330 of 1997 to day 59 of 1998. Keels were identified as ridged ice greater than 0.25 m thicker than the adjacent level ice and with maximum drafts deeper than three times level ice draft (to exclude rafted ice). An average keel shape was defined by searching data for all keels within five ranges of maximum draft: 5.0±0.5, 7.5±0.5, 10.0±0.5, 12.5±0.5 and 15±0.5 m. The populations of the categories were 578, 202, 64, 20, and 9 keels, respectively. Exponential curves fitted to the average draft distribution for each size range have mean e-folding scales of 2.7, 3.9, 4.3, 6.0, and 6.5 m respectively. The large variation in the shape of individual keels is visible in Figure 5-8; the variation in the draft distribution for individual keels is more than an order of magnitude about the mean. However, on average, within a ridge, ice of deepest draft is less common than that of shallowest draft by as much as an order of magnitude for deep keels. The fraction of ice in the deepest bin of a 10 m keel is 58% lower than the fraction in the same bin if ice is uniformly distributed.

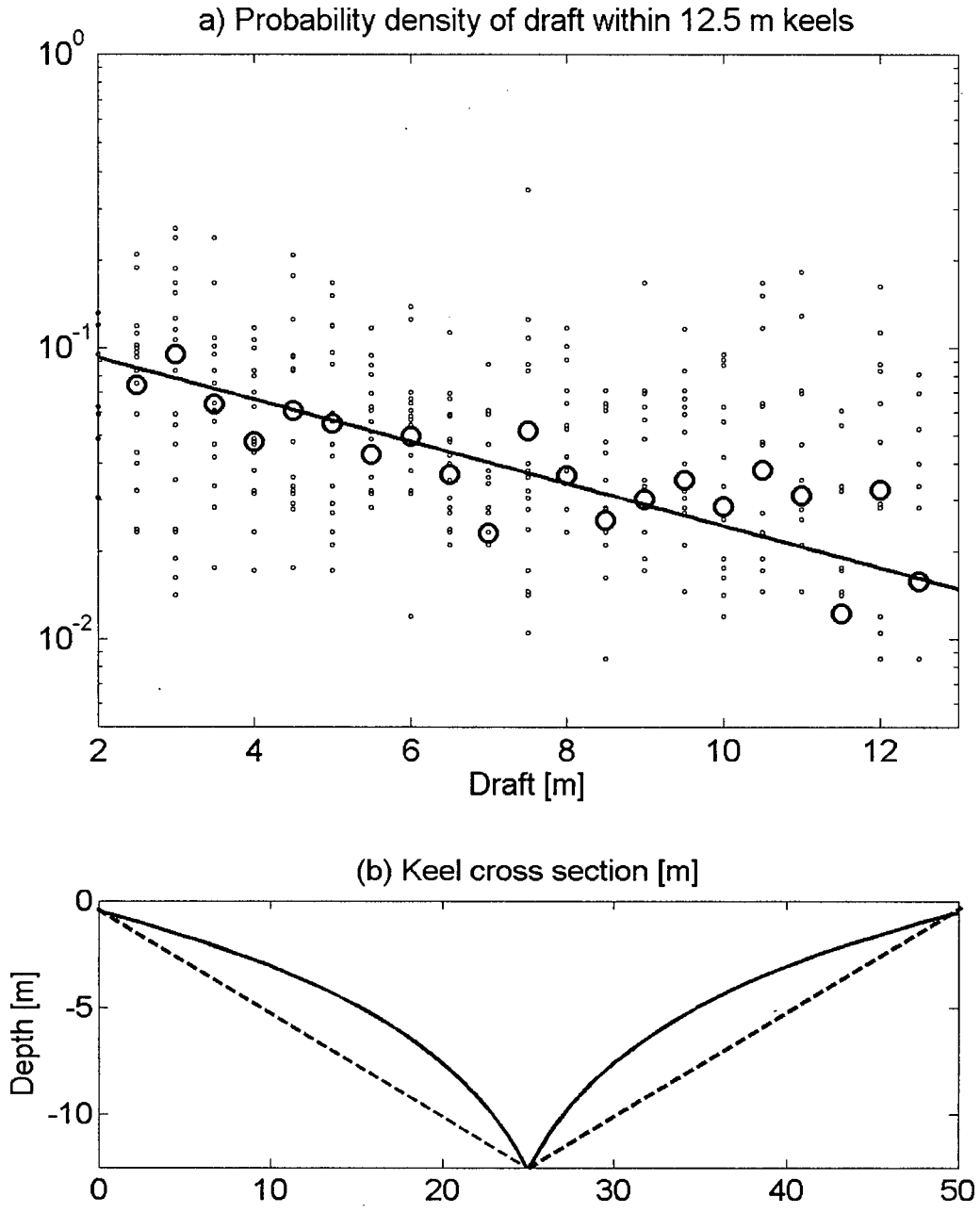

Figure 5-8: Probability density of draft (fraction per 0.5m) within 20 keels of 12.5+0.5 m maximum draft. Small circles represent individual keels and large circles show average values. An exponential curve with 6.0 m e-folding scale fits the average. (b) Cross-sectional shapes (cusped and triangular) corresponding to negative exponential and constant probability density of draft within keels.

In our stochastic IDR model the approximation of ice distribution within a ridge as exponential with characteristic scale λ=6 m for all keel drafts is appropriate to our present purpose. The e-folding scales found may suggest including a depth dependent truncation factor; however for simplicity, a constant value of 6m is used. This value is representative of the e-folding scales for large keels and is easily implemented. The transfer coefficient in (4.3.3) becomes:

$$b(j) = b_o e^{-z/\lambda} \tag{5.5.1}$$

where b_o is a constant to conserve volume and z is the draft in the range $2h$ to $\beta(h)$, where h is the level ice and β is the truncation point. With this transfer coefficient (cusp-shaped keels) and a constant truncation value, the IDR model produces an ice-draft distribution in agreement with the observations up to 15-m draft, but does not match the distribution of the thickest ice (Figure 5-7; line c) similar to the results using the floe availability truncation. With (5.5.1) and the floe-availability truncation algorithm (5.4.1), the IDR model reproduces the observed ridged ice distribution within observational error bounds. In addition, the underestimate in ridged ice within the 4-6 m range is decreased as the constraints place more ice in shallower drafts (Figure 5-7; line d).

Figure 5-9 shows the percent difference in volume fraction of thick ice between the modeled and the observed data. The constant keel truncation and triangular shape results in a 55.5% overestimate of ice volume for ice greater than 9 m. Note that the apparent equivalency of all models for ice thinner than 12 m in draft is due to the short duration of the simulation. Except for the thickest ice, the initial distribution of ice, rather than the newly ridged portion dominates the distributions. Using an exponential keel shape alone, and with a floe availability truncation, decreases the discrepancy by 75% for each case; to a 12.5% overestimate and a 12.5% underestimate, respectively. Over just 23 days, using geometrical constraints, significantly less ridged ice area and volume (2.8% and 8.8% respectively) are placed in drafts exceeding 9 m.

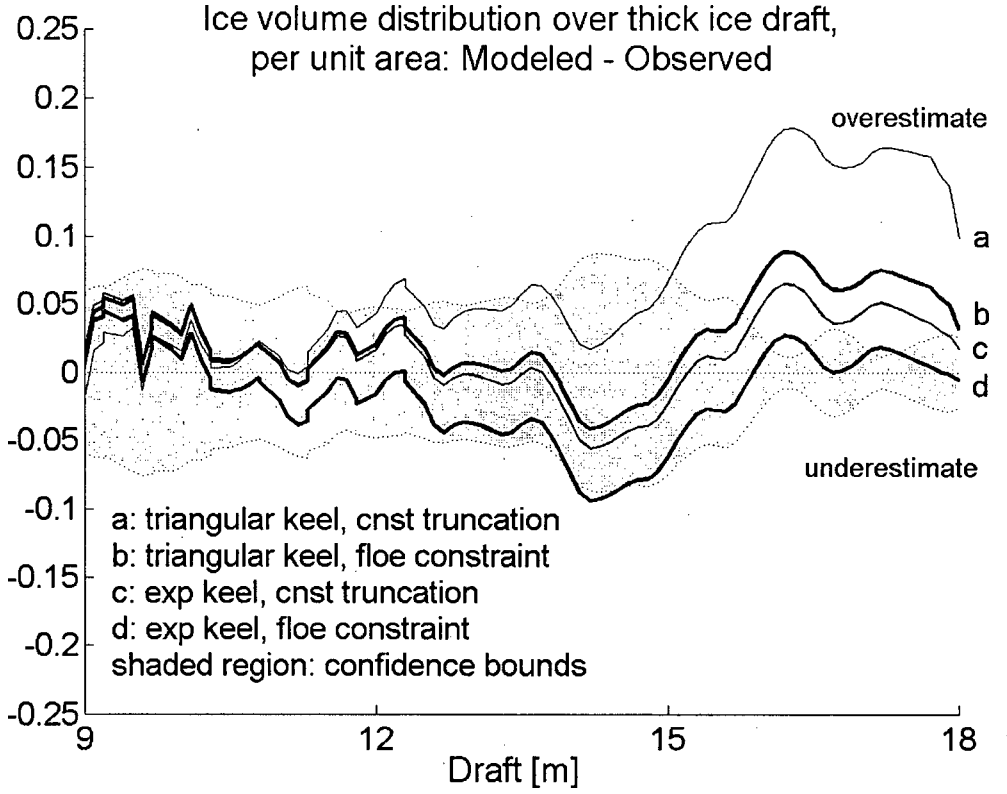

Figure 5-9: Difference in ridged ice volume between the modeled and observed density of ice volume at each draft (volume fraction of ice greater than 9 m thick). Model is run from the 9th January to the 1st February 1998 at site 2. Comparative curves are shown smoothed with a 5-point running average for runs with (a) uniform volume distribution and a constant truncation (b) uniform volume distribution and the floe-availability constraint, (c) exponential (6 m scale) volume distribution and a constant truncation, and (d) exponential (6 m scale) volume distribution and the floe-availability constraint. Combining the exponential volume distribution with the floe-availability constraint, curve (d), produces the best ice draft distribution at both thin and thick ridged ice drafts. Shaded region indicates confidence bounds on the observed distribution representing +/- one standard sampling error based on degrees of freedom.

6. DISCUSSION

6.1. Simulation of pack-ice development during 1991-1992

Conditions of ice drift suited to simulation using the IDR model were encountered also during the winter of 1991-92 (see Figure 3-6). Ice draft and movement were observed at Site 3 to the southeast of Site 2 (Figure 6-1). Beginning on day 324 of 1991, the ice moved shoreward and then seaward in a circle that returned it to the same location on Day 362 (Figure 6-1). Under this unique circumstance, the assumption of along-shore homogeneity in pack ice properties was not required.

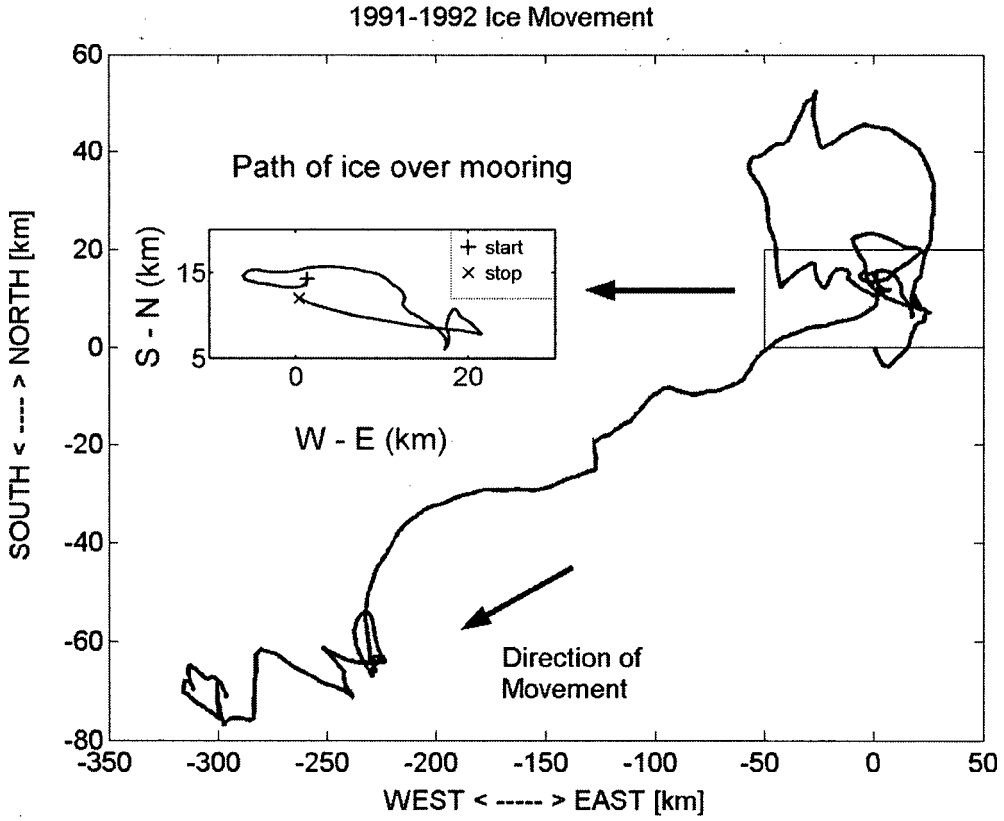

Figure 6-1: The ice motion across mooring site 3 during the winter 1991-1992 is plotted as accumulated displacement. The natural experiment from days 330 to 348 of 1991 when the ice pack remained in the vicinity of the mooring, is used for the verification of the thermal growth model. The trajectory of ice drift over the mooring during this period is shown in the inset (plus sign indicates start of ice motion event).

For this event, observations of ice motion were not available shoreward of Site 3, where changes to the distribution of the ridged ice occurred during the 38-day period. However, because Site 3 was only 29 km from the edge of land-fast ice (Regional Ice Chart, Canadian Ice Service), the average strain rate of ice within the zone was computed from the velocity at Site 3, assuming zero motion at the edge of the fast ice. The 1991 simulation used the same parameters as that for 1997, except that the snow cover in 1991 was set to account for only 5% of the temperature difference between the ocean and the atmosphere, to match observed level ice growth. As before, the calculated divergence was scaled by $1/10^{th}$ to reflect local estimates of opening based on observations of new ice. This scaling implies that most of the strain has been accommodated by opening of a flaw lead at the edge of land-fast ice to the south of the sonar mooring site (Melling, 1998a).

Results are presented in Figure 6-2. The model result on 28 December is a good replica of the observations. The model truncates the distribution at 17 m draft, beyond the deepest observed draft. The difference represents an absence in the transect of only 10 m of ice profile in this draft range. This loss may be explained by the statistics of sampling.

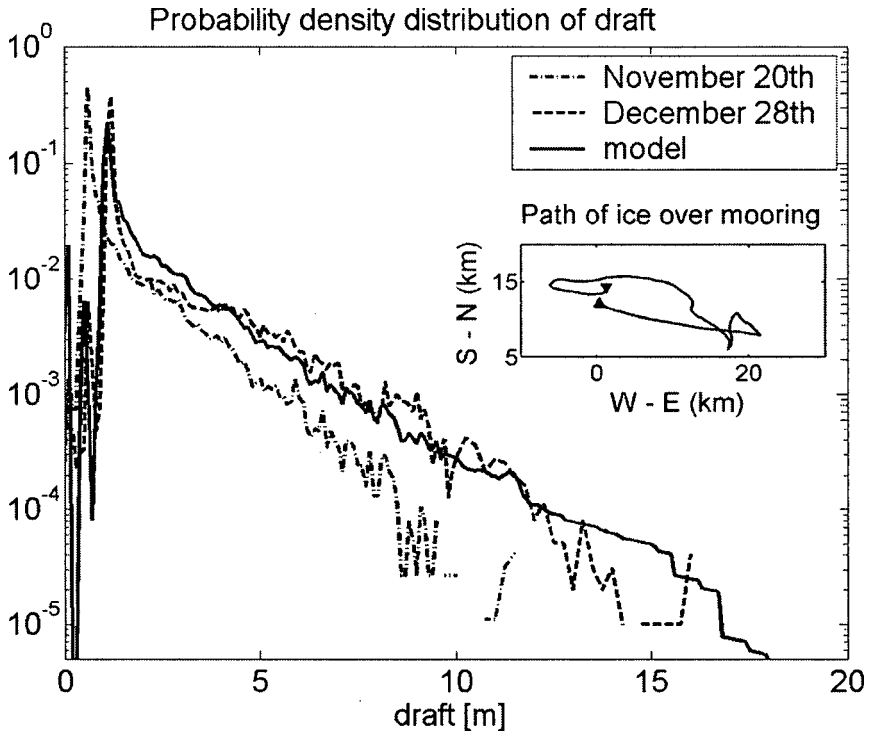

Figure 6-2: Probability density of ice draft (fraction per decimeter) using the floe-availability constraint and assuming an exponential keel shape to simulate pack-ice development in the winter of 1991-1992. The trajectory of ice drift over the mooring is shown in the inset (arrow heads indicate direction).

6.2. An idealized simulation of pack-ice evolution in winter

We now present an idealized simulation of the development of seasonal ice over a four-month period, without observational initialization or verification. An initially ice-free sea surface develops ice as a result of atmospheric forcing observed at Tuktoyaktuk during 1997-1998. The ice is compacted at a constant rate of 1% per day.

Results from the IDR model, with keel-draft truncation based on floe availability (5.4.1) and constant (triangular shaped) and exponential keel draft distributions, are displayed 90 days after initiation (mid January) in Figure 6-3. The combination of the floe size constraint and cusped keel shape produce a distribution with significantly less deep ridged ice. Ice deeper than 10 m covers only 48% of the area and contains only 45% of the volume of the corresponding ice produced by the unconstrained keel and truncation algorithm. This represents a significant portion of the

ridged ice, with 20.5% of the volume of ridged ice exceeding 10 m for the floe size constraint and exponential keel shape compared with 49.4% of the ice exceeding 10 m for the unconstrained case. Because all approaches create the same volume of ridged ice, the area of ridged ice is greater when using the floe size and keel shape constraints and the average draft of deformed ice is less. Such differences may have important implications for the simulation of pack ice in climate models.

After 90 days, the floe size constraint and cusped keel shape have generated an exponential distribution for draft between 3.0 and 18 m, with a 3.11 m e-folding scale. The impact of the maximum-draft constraint, $H=20\ m^{1/2}\ h^{1/2}$, is visible as steps in distribution above 10 m representing the maximum keel size ($20\ m^{1/2}\ h^{1/2}$) that could be formed from the growing level ice draft. The e-folding scale is similar to observations previously reported from the Beaufort Sea in mid-January (Melling and Riedel, 1995; 1996a). The exponential distribution of ice in keels and the floe-size constraint cannot generate realistic draft distributions for ice when used alone and must be used in tandem.

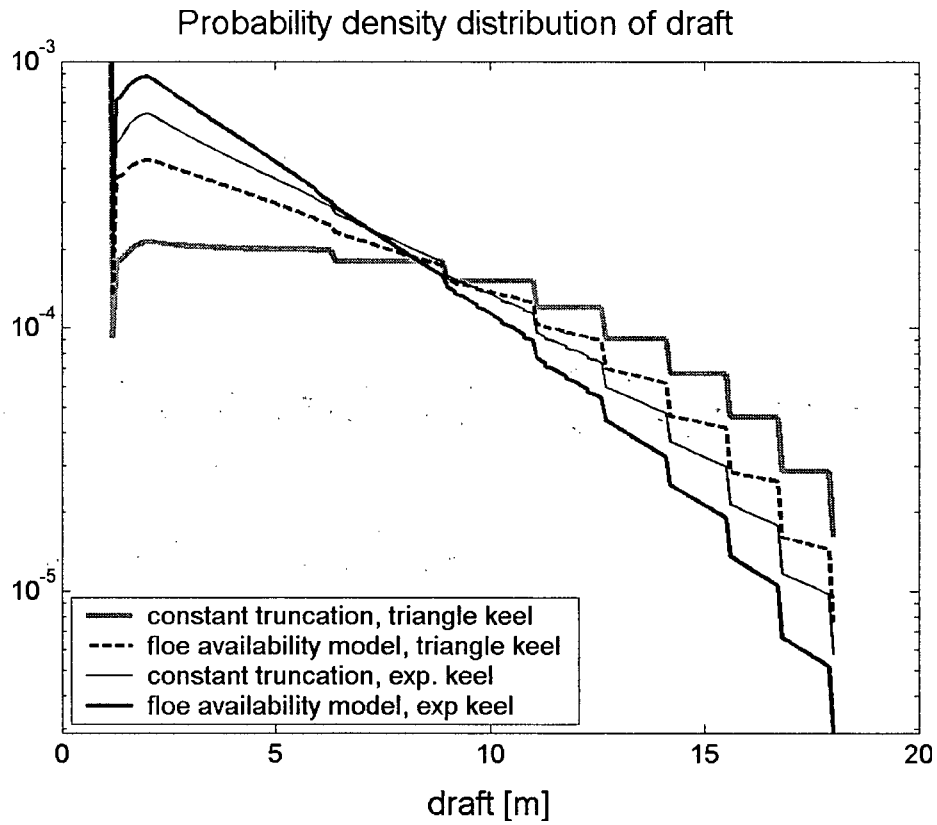

Figure 6-3: Probability density of ice draft (fraction per decimeter) from simulation of idealized pack-ice development over 90 days, assuming various combinations of the truncation model and transfer functions. Best-fit exponential curves with e-folding scales of 4.81 and 3.11 m are found for the floe availability model with triangular and exponential keel shape functions respectively; for exponential keels with a constant truncation the e-folding scale is 3.89 m.

6.3. Convergent motion and ridging

In our present simulations of ice draft redistribution, the onshore compression of pack ice between mooring sites is assumed to be the sole contributor to ice ridging. Confirmation of the validity of this assumption can be made by comparing the amount of level ice consumed by ridging during the simulation with the change in level ice area from initial to final observation. With reference to Figure 5-1, the model "consumes" approximately 27% of the area of level ice and the observations indicate a 25% decrease in level-ice area. The level-ice area lost to shoreward motion is adequate to generate the observed increase in ridged ice volume, without requiring appreciable ice ridging from alongshore compression or shear.

6.4. Keel shape

Runs of the IDR model with an exponential distribution of cross-section versus draft within keels (6-m scale length), but with no constraint on keel draft from floe size, do reproduce the observed change in ice-draft distribution over tens of days. However, runs over longer periods create a draft distribution with too much thick ice: after 90 days the e-folding scale over drafts of 3-18 m is 3.89 m (Figure 6-3). The e-folding scale representative of smaller drafts is larger because the modeled draft distribution without floe-size constraint tends to the 6 m e-folding scale typical of keels, far in excess of the 2-3 m scale typically observed (Melling and Riedel, 1995; 1996a).

The use of an e-folding scale of 6m for creating ridges less than 10m in maximum draft may seem inappropriate based on observed mean e-folding scales, however 40% of all 5m keels have e-folding scales that exceed 5m indicating that this assumption may be acceptable for smaller keels. In addition, running the model with a keel shape e-folding scale of 3m does not visibly change the modelled distribution within the 3-10 m draft range and thus using a constant value seems a reasonable approximation.

Simulations of ridging by other researchers, without restriction on the amount of level ice, build ridges with a trapezoidal shape (Hopkins, 1996a). The draft distribution for these ridges may have more ice at the maximum draft than in the thinner keel flanks, in contrast to the observed exponential roll-off with draft in real ice fields (Figure 6-4). The floe-availability constraint and cusped keel shape constraint, which limit the draft and width of keels, create draft distributions in agreement with observations.

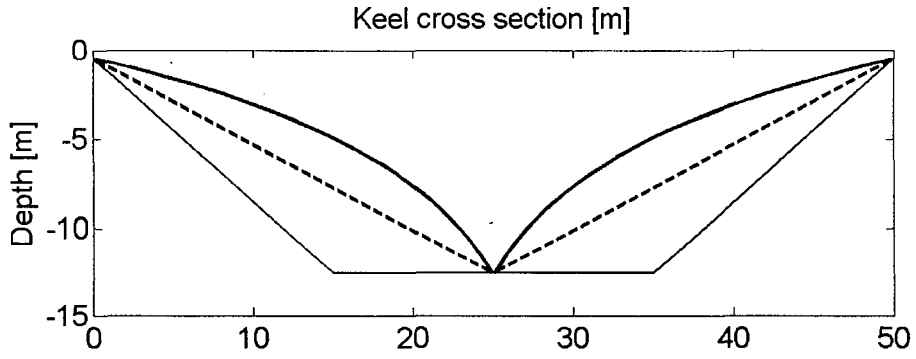

Figure 6-4: Schematic of ridge shapes illustrating the varying distribution of ice with draft. The exponential roll-off (heavy solid line) places far less ice at the thickest keel drafts than the triangular keel shape assumed by Thorndike et al., (1975) or the trapezoidal keel shape of Hopkins (1996a).

The observed e-folding scales of the 5, 7.5, 10, 12.5, and 15 m keels increase with draft (as 2.5, 3.8, 4.3, 6.7, and 5.8 m respectively. The draft-dependent increase in λ was not included in the IDR model for simplicity, and the constant value of 6 m was chosen to ensure that the distribution of ice in the thickest keels would be compatible with observations.

What would be the impact of varying λ with h? For keels with smaller drafts, more ice would be placed in the thinner keel edges, thus increasing the distribution of ice in the smaller draft ranges (<10 m). However, during the simulations in this thesis, as the distribution of ridged ice is on short timescales and the amount of ridged ice already at these drafts is appreciable, the difference in draft when λ was decreased was not visible. In contrast, for the ice thicker than 10 m, changing λ will greatly affect the visible amount of the thickest ice as the ridging in the model makes up a large proportion of the ice at those drafts.

The assumption is also made that the e-folding scale will not change seasonally. As the distribution of level ice flow size is not seen to vary with thickness, and thus season, we assume that keels are created with similar constraints on level ice availability throughout the season. Yet a 5 m keel in the early winter is likely to have been created by a large expanse of thin ice according to (5.2.2), as thicker ice is not present in the seasonal Beaufort Sea. However, in midwinter, floe size availability (Figure 5-3) suggests that a 5 m keel is more likely created by the

available thicker ice, as limited by floe extent. The importance of level ice extent on keel shape is not known. To investigate this, a model similar to the particle model of keel formation developed by Hopkins (e.g. 1998) could explore the evolution of keel shapes with level ice consumption during ridging. However, such work is beyond the scope of this thesis.

The seasonal variation in keel shape may be due to observational limitations. Ice draft profiles used to identify keels may not separate adjacent keels that do not have thinner level ice or open water between them. Extended edges of keels may consist of smaller ridges formed at a later time from ice abutting the large keels, features not resolved by the keel criteria. Thus a keel initially formed with an e-folding scale of 6 m could be observed to have a greater e-folding scale after subsequent ridging events.

Finally, it must be noted again that the variability in e-folding scales between individual keels far exceeds the variability in average e-folding scales with draft. Keel shapes vary by orders of magnitude, and the e-folding scale used in the IDR model is a parameterization of the average ridged ice distribution, not a representation of the shape of an individual keel.

6.5. Importance of divergence on the local characteristics of the ice pack

In developing and adapting the IDR model to the mooring data in the Beaufort Sea, two changes in the formation of open water are made to the model from the standard equations. In (4.1.2), open water is created directly in response to the divergence of the ice pack. In addition, open water is created in ridging to balance the loss of ice area due to convergence. Both of these open water terms are necessary to balance the area of ice lost during ridging and divergence. For mooring data, such as the 1997/1998 ice profile record at site 2, both these sources of open water are not visible in the probability draft distributions during the onshore-offshore motion event A and thus are excluded or reduced in the model.

During event A, the ice first moves southwards compacting against the coast over both sites 1 and 2 (Figure 6-5). While the ice is moving south, the relative motion between the mooring sites is both divergent and then convergent in the first 10 days. According to (4.1.2), open water should be created through divergence from days 11 to 13, and then created to balance area lost through ridging during days 14 to 16. Yet in the distribution observed between day 25 and day 27, no

open water or newly grown level ice is observed at site 2 (Figure 6-6). At site 1, over 80% of all ice observed is less than 0.2 m in thickness. At this time of year, ice will grow to 20 cm in less than 5 days (calculated from thermal growth model of Melling and Riedel, 1996). This indicates that the new level ice observed on day 25 at site 1 (Figure 6-6) was created after day 18 and this is not from the earlier divergent motion around day 12-13 (Figure 6-5).

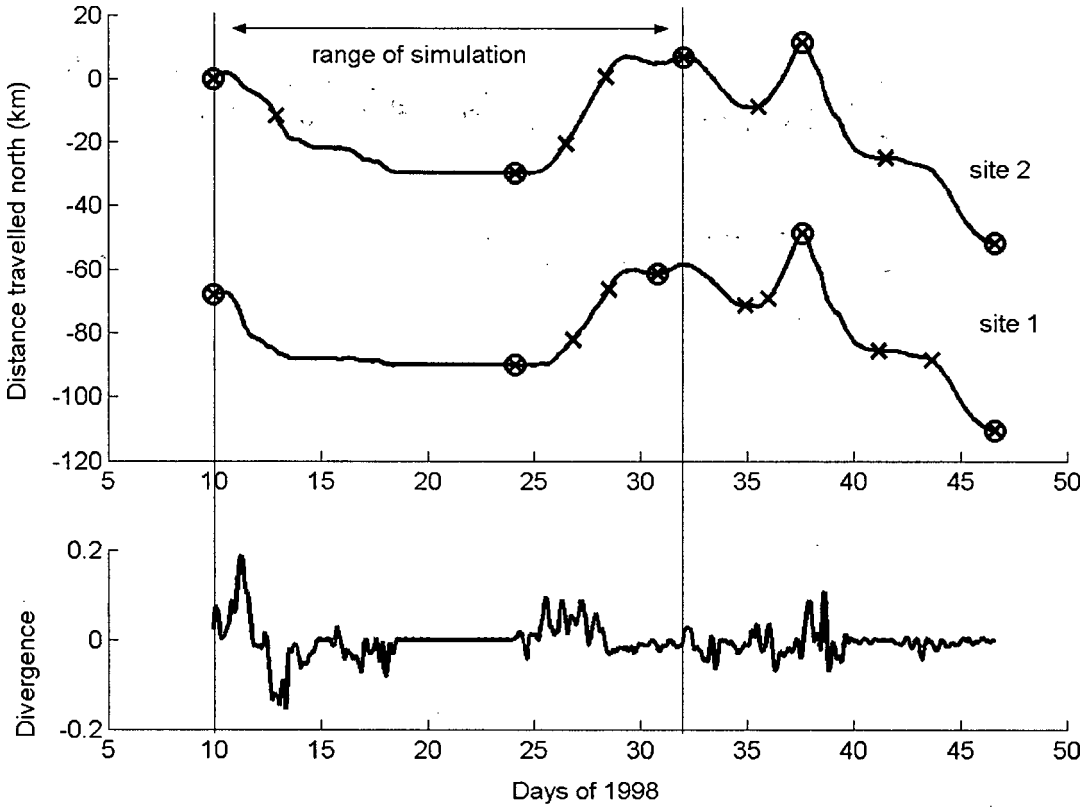

Figure 6-5: Motion of ice over sites 2 and 1 during event A in 1998. Upper panel displays the northward motion of ice across the moorings from days 10 to 47. The IDR model simulates the evolution of the distribution of ice from days 10 to 32. Crosses indicate the temporal start point of the ice profiles used to construct the statistically independent density distributions of draft. Circles indicate distributions plotted in figure below. The lower panel displays the divergence [day^{-1}] calculated as the velocity difference between the sites divided by the distance (68 km).

Where is the open water created during divergence and ridging? While ridging occurs locally at moorings, divergence may not. Riding is assumed to occur at many locations during

compression, as supported by the success of the floe availability constraint for ridging that creates multiple ridges of varying sizes. Divergence may occur by leads opening in more localized regions. If the moorings do not observe these leads because they lie between the sites, then no record will appear in the data.

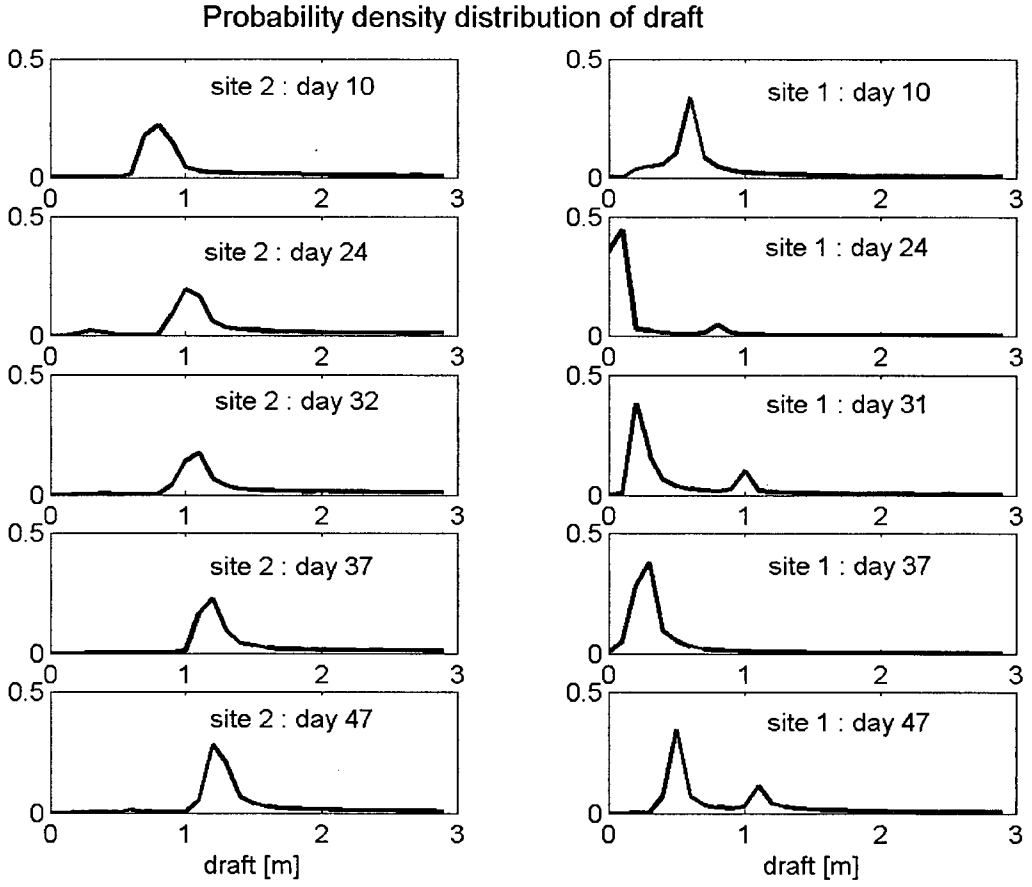

Figure 6-6: Probability density of draft distributions (fraction per decimeter) for sites 2 and 1 during and after convergent-divergent event A. Days (of 1998) listed represent the start date of the data profile used to create the distribution.

The second divergent motion even between days 24 to 29 (Figure 6-5) may create open water at the site 1 mooring. The event accounts for a 12% expansion of the ice between sites 1 and 2 over 3.1 days. Although no evidence of this open water is seen in any distributions at site 2, or in distributions after the divergence event at site 1, the open water and new ice at day 24 may be created by this divergence event (Figure 6-6). The distribution of ice starting at day 24 is

constructed from a profile stretching to the end of day 27. During days 25 and 26, the ice is undergoing divergence and opening water, which may be observed at the mooring site. If that lead is situated over site 1, it could explain the large area of open water or thin 10 cm ice covering 80% of the ice area profiled.

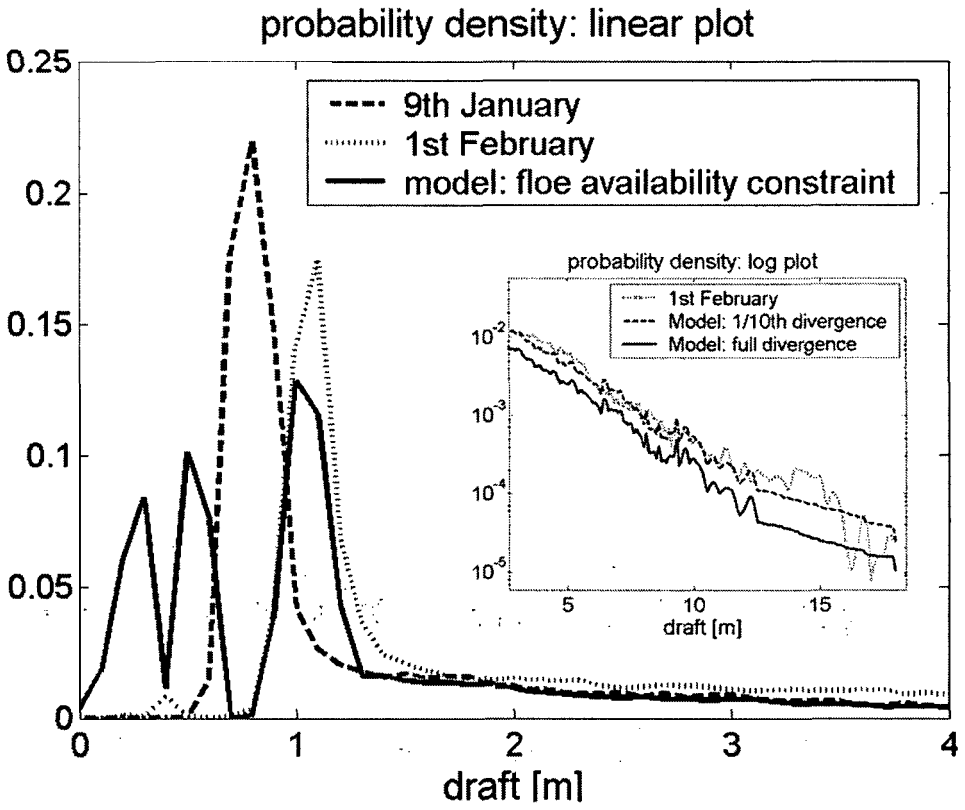

Figure 6-7: Probability density draft (fraction per decimeter) of ice evolving from the 9th of January to the 1st of February. The divergence in the model is equal to the total divergence observed between sites 1 and 2, and ridging is assumed to create open water in the same area as the observed ice. The impact of the divergence on the ridged ice is seen in the inset figure. While the total amount of ridged ice decreases (area conservation), the shape of the ridged ice does not change.

The origin of the open water and thin ice observed between days 24 and 27 at site 1 cannot be confirmed; however, it is clear that open water caused by divergence or ridging is not seen at site 2. For this reason, the IDR model adapted to evolve the distribution of ice at site 2 during event A does not include all of the observed divergence between the sites. For the IDR model the

divergence is set to one-tenth the total amount and is an estimate of the divergence that creates open water locally to the ice observed at site 2. This $1/10^{th}$ fraction prevents excess open water from being created and produces thin ice in agreement with observations. Running the model with the total amount of divergence and allowing ridging to create open water produces far too much thin level ice (Figure 6-7).

While the assumption that the divergence seen by the sonar at site 2 is only 10% of the total is arbitrary, for the purposes of this research, it is unimportant. Increasing or decreasing the percentage of divergence assumed to be observed at site 2 would increase and decrease the amount of thin level ice, and inversely impact the amount of ridged ice. However the shape of the ridged ice is determined by the ridging algorithms in the matrix Ψ, and is generally unaffected by the divergence (Figure 6-7). Large changes in the divergence would have the potential to change the shape of the ridged ice distribution; as large amounts of thin ice would lead to smaller ridges being created. This is not apparent in changing the divergence fraction by a factor of 10 on short timescales of weeks.

6.6. Stress levels in the ice pack.

With the distribution of floe sizes established and the critical stress for ridging found to be independent of floe size once the characteristic buckling length is exceeded, the possibility for ridging to be limited by stress levels in the ice pack is considered. The determination of ice stress within a region is not easily obtained. While the patterns of stress observed at different sites show temporal correspondence, the magnitudes of stress varies greatly between sites (Richter-Menge et al., 2002). In addition, thermal ice stresses are often on the same order of magnitude as mechanical stress (Richter-Menge et al., 2002) and stress measurements vary greatly between sites on a single floe (Richter-Menge and Elder, 1998). As such, no observations are available of the distribution of ice stress through a region and the estimates are from limited observations.

Observations of the stress during a ridging event in a large, thick (3.5 m) floe were made in the spring of 1989 (Comfort and Ritch, 1989). From these data, a mean background stress can be estimated from the stress levels observed immediately after a ridging event. A mean background stress of 20 kPa was observed after widely varying residual stresses from the experimental set-up

were subtracted from the sensors. Peak ice stresses during the event varied greatly with the location of the sensors. The maximum stress recorded by any sensor was 240 kPa, and remained at 150 kPa for approximately 30 minutes at one site. The shear stress was, on average, one third of the maximum stress.

A similar mean background stress of 20 kPa was observed late in the season during the SHEBA and SIMI experiments in the Beaufort Sea north of Alaska (Richter-Menge et al., 2002). Baseline stress returned to zero between events before mid-November, after which a gradual increase in baseline stress was observed. This was attributed to the continual increase of compressive strength of the pack due to mechanical thickening of the ice. During ridging events much higher maximum stresses are recorded, reaching values of 100-200 kPa (Richter-Menge and Elder, 1998). Commonly reported mean stress levels during ridging events are reported in the ranges of 45 to 50 kPa (Comfort and Ritch, 1989) and 30-60 kPa (Richter-Menge et al., 2002).

For stress to be a limiting factor on ice ridging, the stress must be less than the critical buckling stress ((5.3.4), Figure 5-5) for the ice floe. An estimate of this using the values of 2 GPa for Young's modulus and 0.3 for Poisson's ratio is 5 MPa. So is ridging limited by buckling stresses? The maximum stress levels recorded in a floe are almost an order of magnitude smaller than the predicted critical stress. Yet ridges are common features in sea ice, and it seems likely that the high stresses needed to instigate ridging are localized in thin ice, not suitable for direct measurements of stress and existing only for brief periods of time before being dissipated at ridge initiation. To ascertain if ridging is limited by stress levels, a series of observations of stress in new thin ice would be needed.

6.7. Time and distance scales

The possibility exists that ridge development could be limited by the time scale of convergence, or by the amount of strain during a coherent motion. This seems unlikely when we look at Figure 6-8. For a ridge to be formed with a maximum truncation factor of 20 $m^{1/2}$, just 560 m of ice must be consumed. As we can see in the Figure 6-8, convergent motion events exceed the 560 m limit before motion changes direction.

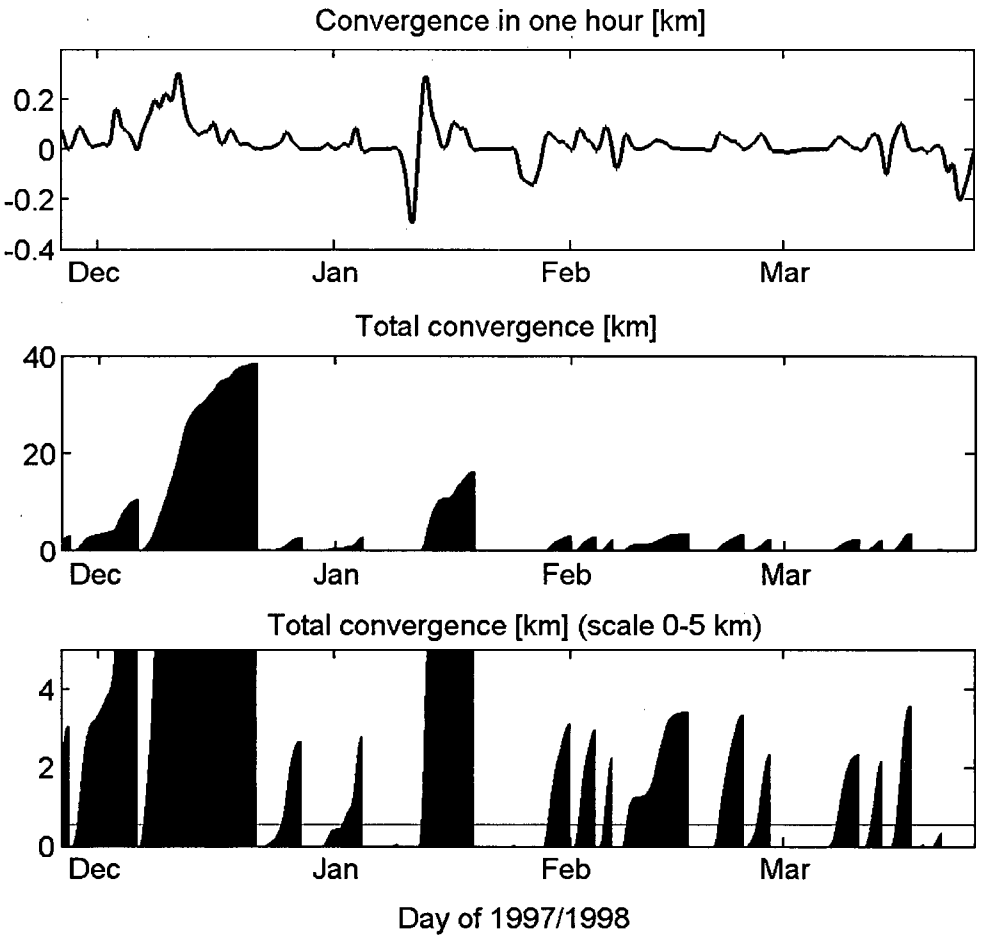

Figure 6-8: Onshore and offshore convergence travelled by ice during the winter of 1997/1998. Upper panel demonstrates the convergence (km) travelled in one hour. Lower panels illustrate the convergence (km) travelled in one direction before the motion changes direction. Lower panels are identical except for vertical scale. The convergence travelled exceeds 560 m for all but one convergent (and therefore ridging) event.

6.8. Model limitations

The incorporation of a cusped keel shape and floe availability into the redistribution algorithm provides a better simulation of the amount of deep ridged ice but does little to improve replication of the bulge of ice exceeding the exponential distribution in the 3-5 m draft range (visible in Figure 5-7). Perhaps the bulge is an indication that the ice viewed at the end of this event may have come from a population different from that used to initialize the model.

This bulge between 3-5 m might also be an indication of ice rafting in response to pack-ice compression, a process not incorporated within our model. By including rafting, Babko et al., (2002) were able to improve agreement between model and observations for ice drafts in this range. Further work evaluating the combined effects of rafting, floe availability constraints and keel shape may be more definitive in determining the mechanical redistributor over the entire ridged ice distribution.

7. CONCLUSIONS: GEOMETRIC FACTORS INFLUENCING RIDGE FORMATION

An ice-draft redistribution (IDR) model has been developed to simulate the development of seasonal pack ice observed by a moored ice-profiling sonar in the Beaufort Sea. Deformation episodes selected carefully from the data record, which spans more than a decade in this area, are natural "experiments" on ice-draft redistribution. These observations provide a unique opportunity to evaluate thermodynamic and mechanical redistribution algorithms.

The IDR model uses thermal growth algorithms that utilize a remapping approach (Lipscomb, 2001). These simulations track the observed growth of drifting level ice without exhibiting numerical diffusion. The only prior evaluations of ice-growth algorithms have been based on observations of land-fast ice in shallow water or multi year sea ice. However, the IDR model creates too much ice in the thickest draft categories when using current algorithms for ice-thickness redistribution through ridging (Thorndike et al., 1975; Hibler, 1980). Such algorithms assume an unlimited supply of ice for ridging. Our analysis of the lognormal size distribution of level floes in the Beaufort Sea indicates that large expanses of ice are in short supply. Three quarters of the level floes observed in the Beaufort Sea are too small to form ridges of the maximum draft possible for their thickness.

Our IDR model uses a random selection of floes from the empirical size distribution to determine the draft of the keel to be built next. Minimum ridge size is constrained by the characteristic length of a floating plate in buckling. The floe availability model is a simple geometric constraint on ridge formation. It improves the capability of the model to reproduce the distributions of ridged ice, suggesting that floe size is an important constraint on ice ridging.

The cross-sectional shape of keels also has a significant impact on the draft distribution for ridged ice. Although underwater shape of observed keels varies widely, the average distribution of draft for larger keels can be represented as an exponential with a 6-m e-folding scale, truncated at maximum keel draft. Replacement of the usual uniform draft distribution in keels (triangular keel shape) with an exponential form improved the model's simulation of deep ridged ice. Idealized simulations indicate that over longer timescales the use of cusped keel shape is not in itself sufficient to replicate observed distributions of ridged ice.

The combined implementation of the floe-availability and the exponential-keel-shape constraints in ice-draft redistribution produces the best results. Using this approach, the volume of thick ridged ice is 8.8 % (for draft exceeding 9 m) over a 23-day "natural" experiment and 20.5 % (for draft exceeding 10 m) over a 90-day idealized experiment. These differences will have an impact on the strength of the pack ice and on its response to thermodynamic forcing via consolidation and melting.

SECTION D: SUMMER RIDGE EVOLUTION

8. ADAPTING THE ICE DRAFT REDISTRIBUTION MODEL TO SUMMER MELT

8.1. Winter 2000

The ice draft redistribution model developed in the Sections B and C of the thesis can provide valuable insight into summer ridge ablation processes when adapted to the melt season. Suitable ice motion events where the ice remained in the region of the moorings through June and July of 2000 suggest that the model be compared with observations from that year. To develop confidence in the suitability of the IDR model for the year 2000, the model was first adapted to the midwinter season (January-February). During the first 50 days of 2000, the ice moved south approximately 55 km (Figure 8-1). Subsequent to this movement, no offshore ice motion was found, so the ice was not re-viewed by the sonar. Instead, after ice ridging, the model results are compared to the observed distributions at both site 1 and site 2, as the initial ice surveyed now lies in between the two sites.

The winter 2000 model is similar to the 1997-1998 winter model with differences only in the divergence fraction. During mid-winter, the divergence is not set to $1/10^{th}$ the observed divergence, as was done for previous modelling cases. This is due to the simulated ice motion event. Both the 1997-1998 and 1991-1992 simulations of events included significant onshore and offshore motions, where the ice returned to the initial offshore distance. The year 2000 motion event moves ice in the onshore direction, without a significant offshore divergence that could create a large open water lead. As offshore divergence was not present, the assumption that divergence opens a large flaw lead, which was not visible to the sonar, is invalid. The small divergent motion events superimposed on the convergent motion may open up water throughout the ice pack. The divergence fraction is thus set to 1 on the assumption that no single lead dominates the divergence.

The results of the winter ridging model in the year 2000 are shown in Figure 8-2. The modelled level ice thickness lies between the observed level ice thicknesses at sites 1 and 2 suggesting that thermal ice growth is accurate. The ridged ice thickness matches the ridged ice distribution at site 1, 15 km south of the final location of the modelled ice distribution. The agreement between modelled and observed distributions of level and ridged ice for days 1-50 of the year 2000 shows that the model is applicable to ice motion events observed during the winter season.

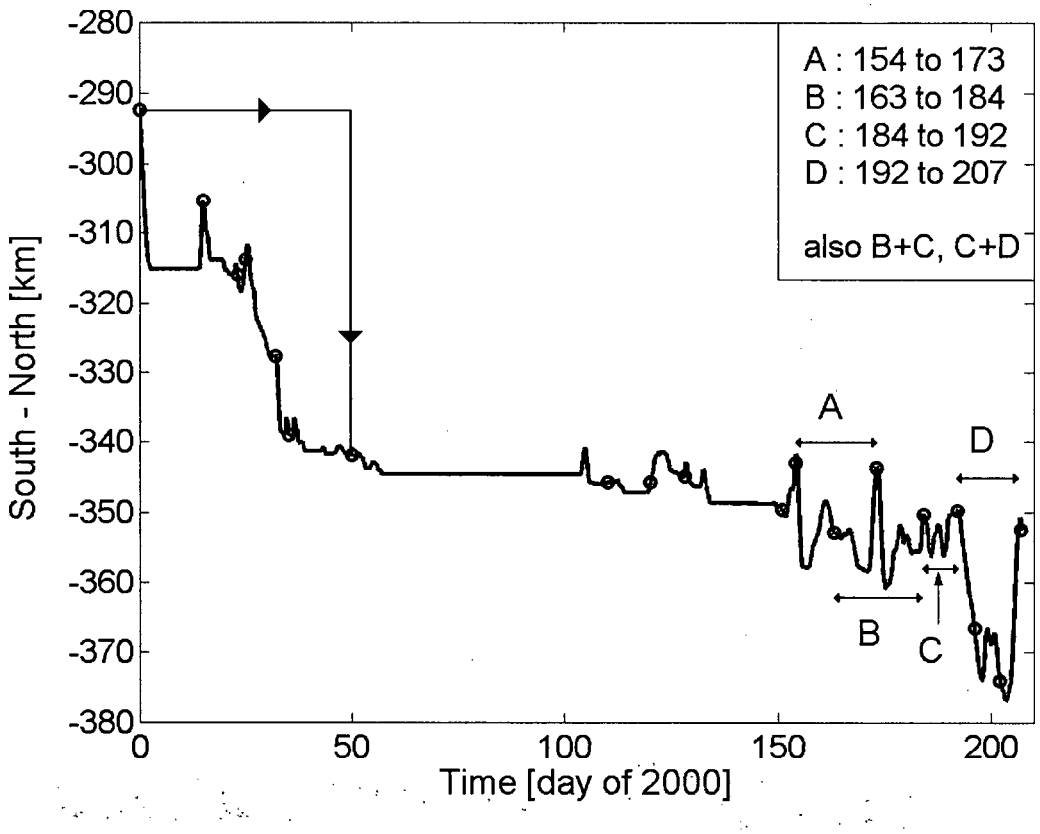

Figure 8-1: North - South motion of ice over mooring site 2 during the first half of the year 2000. Observed ice draft distributions are centred at points indicated by circles on the path. Initially, during January and February, ice moves south compacting against the coast before remaining relatively stationary in the north-south direction (thin lines with arrows indicate range of motion). Melt begins around day 150 and four ice motion events are identified where the ice moves in an onshore-offshore pattern (indicated by lines double ended with arrows).

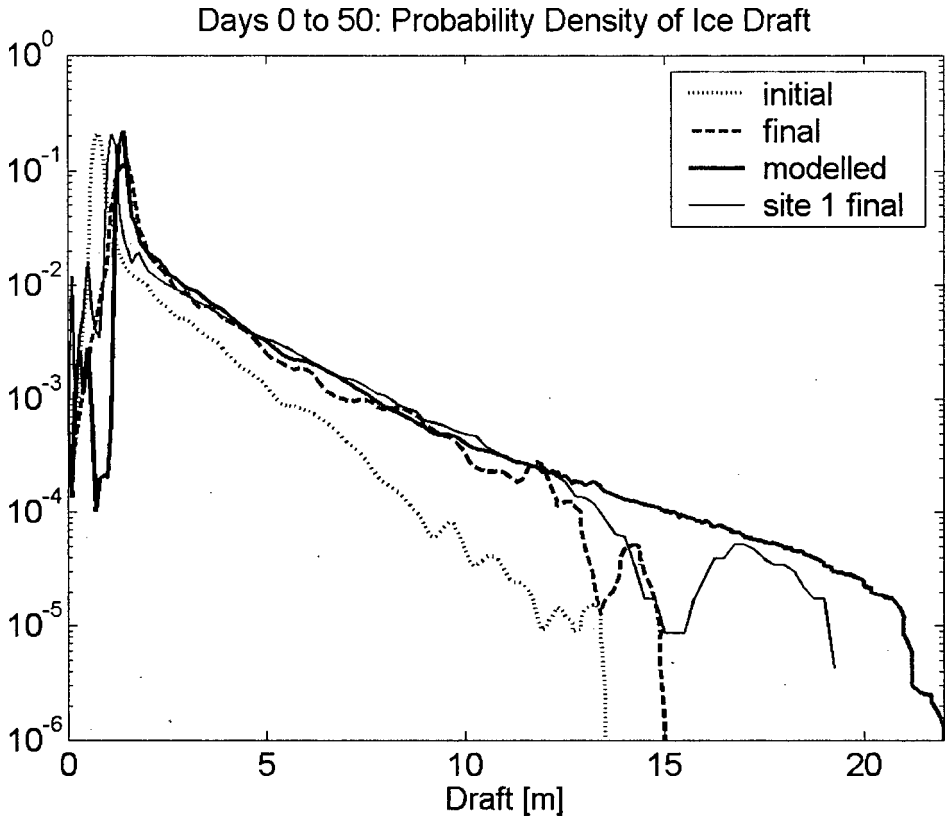

Figure 8-2: Probability density of ice draft (fraction per decimeter) for the results of the IDR model at site 2 during the first 50 days of 2000. Note that the model (heavy solid line) reproduces the level ice growth of the final ice viewed at site 2 (heavy dashed line) and the thickest ridged ice at site 1 (thin solid line), 15 km south of the final location of the modelled ice distribution

8.2. Level ice melt

The thermodynamic ice growth model used to predict winter ice growth (Section 4.2) is not relevant to summer melt conditions. Unlike growth, which occurs only at the ice-water interface, melt also occurs at the ice-air interface. This surface melt, along with the changing snow cover characteristics, introduces seasonal variability to the surface albedo due to the varied upper ice surface. Attempts to parameterize the albedo and the sensible heat flux have been addressed in detail by other researchers. (e.g. Perovitch et al., 2002; Curry et al., 2001; Flato and Brown, 1996; and Dumas et al., 2003).

The pattern of annual variation in ice and snow thickness can be observed in landfast ice measurements at Cape Parry (70.15° N, 123.33° W), as shown in Figure 8-3. Data are from the Canadian Ice Service Archives and span the years 1959 to 1992. In an average year, snow begins to melt at the start of May and has disappeared by July. Ice melt onset lags snow melt by approximately 2 to 4 weeks, beginning in the latter half of June, in agreement with observed level ice draft melt which began around day 150 (May 29th) of 2000 (Figure 8-4). While snow depth and melt can vary regionally, we expect that during ice motion events A to D (Figure 8-1) the snow cover insulating the ice is decreasing in a similar manner to Figure 8-3.

Along with the insulating properties of snow, the albedo of the snow-ice surface begins to vary due to wet snow and an increasing number of melt ponds, which have low albedo and act to absorb more shortwave radiation than snow or ice. Extensive research during the SHEBA experiment compared the results of eight albedo parameterizations of varying complexity with the observed SHEBA averages (Curry et al., 2001). Curry et al., (2001) note that a "surface albedo parameterization with more complex dependence on surface features can give a degraded simulation of surface albedo if the simulation of surface features is unknown." Of all eight parameterizations, a constant albedo parameterization of 0.75 and 0.5 for snow and ice, respectively (Parkinson and Washington, 1979) was found to be one of the more accurate. This is similar to the results of Dumas et al., (2003) who found that a constant albedo of 0.55 for melting ice was the best at reproducing the evolution of ice thickness in the central Arctic. Moored sonars provide no information about the surface features (melt ponds, snow cover) of ice, thus allowing level ice melt to be modelled with no more accuracy than the simplest parameterizations.

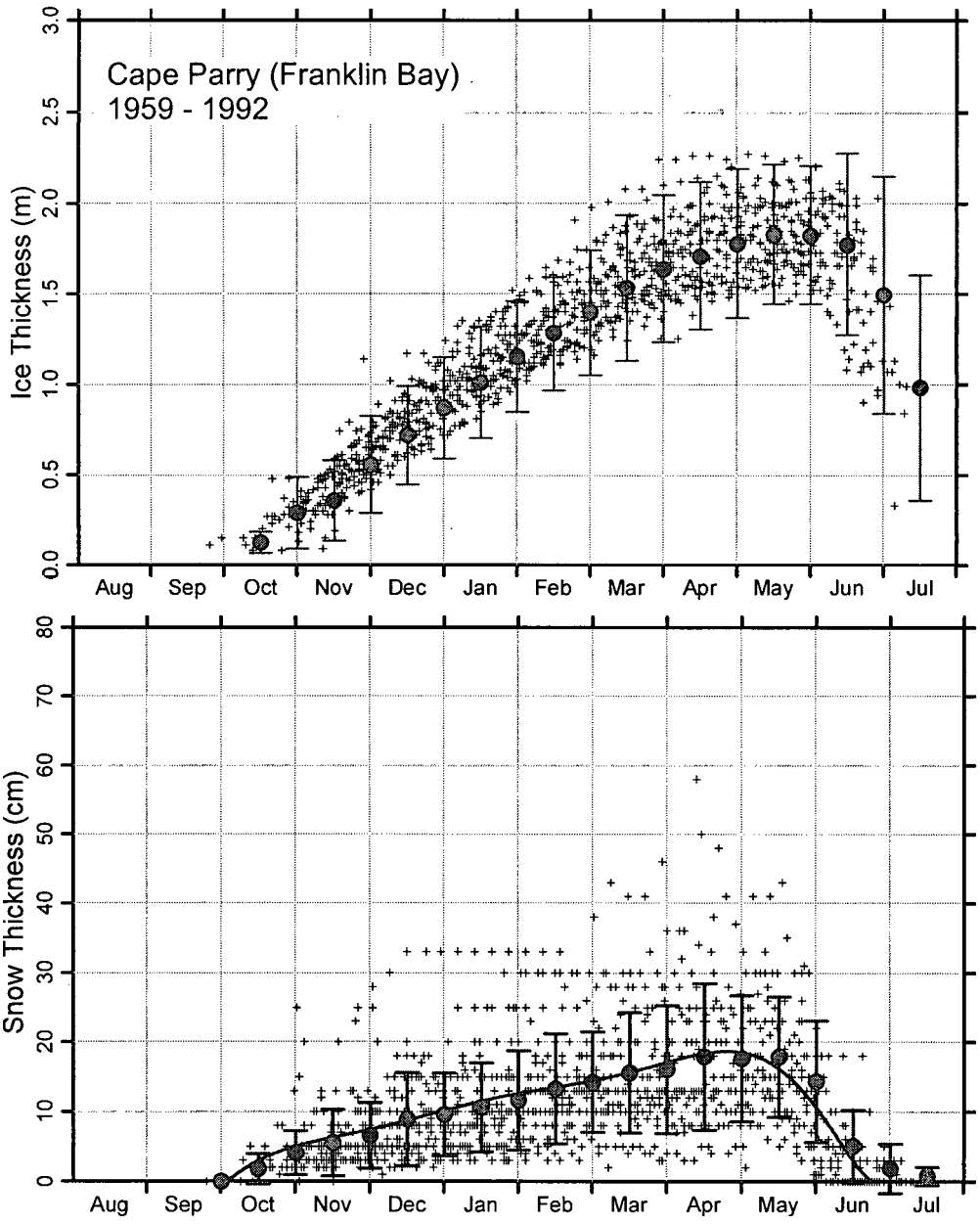

Figure 8-3: Ice and snow thickness observed at Cape Parry from 1959 to 1992. The decrease in snow cover can be seen in early May, preceding the decrease in ice thickness by two to four weeks. Error bars indicate +/- one standard deviation from the mean (large circles). These raw data are from the Canadian Ice Service Archives, http://ice-glaces.ec.gc.ca/App/WsvPageDsp.cfm?ID=210&Lamg=eng. (Figure courtesy of Humfrey Melling.)

Fortunately, accurate modelling of level ice melt is not essential for the investigation of processes enhancing ridged ice melt that are addressed in this thesis. Observed level ice melt rates can be used as draft independent melt rates for all ice thicknesses and provide an upper bound on the thermodynamic melt of thick ice without considering ridge specific processes. The observed relation between level ice draft and time can be approximated with a quadratic and is shown in Figure 8-4. Melt rates are then approximated as a linear function (Figure 8-4, inset) with slope and intercept -0.0004 m day^{-1} and 0.044 m day^{-2}.

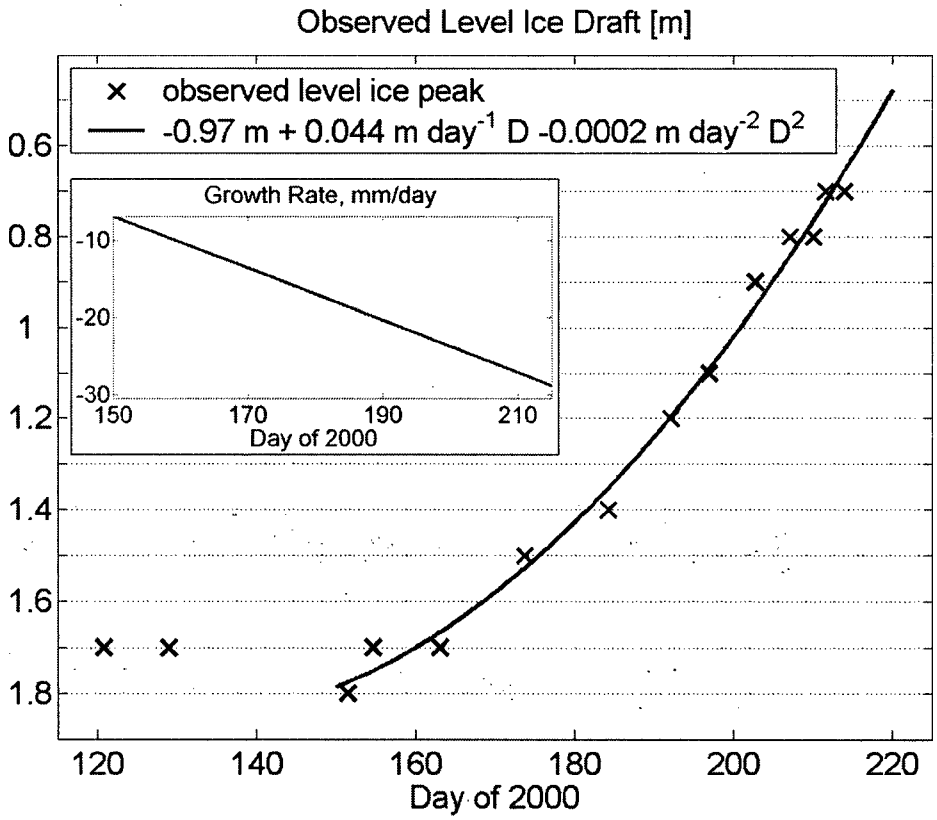

Figure 8-4: Observed level ice draft (dominant mode) and quadratic best-fit curve used to estimate level ice melt rates. D is the day number of year 2000. Inset figure shows the increasing melt rates (as negative growth rates) as the season progresses.

8.3. Model predictions

During the year 2000 melt season, four potential ice motion events are identified (Figure 8-1) where the same ice, with the assumption of alongshore homogeneity, is viewed multiple times by the sonar. In order to allow convergent strain forces to be estimated, the motion of the ice must

be first onshore and then offshore where strain is calculated from onshore velocities. Events A and D are preferable for modelling and bracket the beginning and end of the melt season. Event B is less suitable; as the ice parcel moves offshore of the mooring and accurate compressive strain information is not available during this time. Event C is excluded due to the short time scale of the motion, the initial and final observed draft distributions are constructed from adjacent sections of the ice profile reducing confidence in the observed ice evolution.

The maximum draft of ridges created during the melt season will be lower than the draft of ridges created from the same thickness of level ice during the winter season. Sea ice strength is a function of the brine volume within the ice. As the temperature approaches the freezing point, the brine volume will increase as saline ice pockets begin to melt, and the sea ice strength will decrease. This has implications for the maximum draft of ridges, which during the winter is set at $20\ m^{1/2}\ h^{1/2}$, and represents the point during ridge creation when the force needed to push another ice block beyond the current ridge draft exceeds the force needed to buckle adjacent level ice (Hopkins, 1998). Decreased level ice strength will cause the maximum ridge draft to be reached at a lower multiple of $h^{1/2}$.

Estimates for the appropriate expression for the maximum keel draft are very difficult to obtain. Ice strength estimates are consistently found to be lower in the field than in small laboratory samples (Dempsey et al., 1999) and the temperature of the ice during the events simulated here is not known. During event A, at the start of the melt season, air temperatures had recently surpassed freezing and ice strength would be starting to decrease. In event D, in early July, air temperatures had been above freezing for over a month. Initial estimates for keel truncations can be found by looking at the maximum draft of level ice observed during these melt periods, and using the dominant mode of level ice during these events to estimate the relationship between keel draft and level ice. For event A, a maximum keel draft of 15.2 m is observed, with level ice draft at 1.8 m, indicating an upper bound on keel draft may be $H=11\ m^{1/2}\ h^{1/2}$. For event D, a maximum keel draft of 10.2 m is observed, with level ice draft at 1.3 m, indicating an upper bound on keel draft of $H=9\ m^{1/2}\ h^{1/2}$. The largest observed ice keels may be remnants of keels formed earlier in the winter season, such that these maximum keel drafts that can be created during the events are overestimates. During events A and D we can be reasonably confident that no ice is created thicker than predicted by these truncation points based on observations.

Further insight into the maximum drafts of level ice can be found from ice strength measurements (Johnston and Frederking, 2001) conducted using borehole jack tests in the Canadian Eastern Arctic Archipelago (71° 14.7 N, 97° 09.2 W) in first year sea ice. From the 14th of May to the 11th of June, 2001, the ice strength at a depth of 30 cm decreased by over 50%, from 22 to 10 MPa. At larger depths, similar decreases occurred. An extended data set from 2000 shows further decreases in ice strength to mid July. By day 200 of year 2000, ice strength at all depths was less than 5MPa, with only 25% of the ice strength in the upper layer during May. These values suggest that the ice strength during events A and D will be considerably less than the mid-winter strength. It appears that reasonable choices for the relationship between maximum keel draft and level ice for events A and D are 11 $m^{1/2}$ $h^{1/2}$ and 9 $m^{1/2}$ $h^{1/2}$, respectively.

During the simulations of events A and D, (Figure 8-1), the divergence is set to 1/10th the observed values (see discussion in Chapter 5) and the models are run with and without ridging. Results are plotted in Figure 8-5 and Figure 8-6. Observed and modelled level ice peaks match, as ice melt is fixed at observed rates. Large discrepancies between the observed (dashed) and modelled (heavy and thin solid lines) distributions of thick ice are evident.
Including ridging and melt processes, the modelled distribution of thick ice increases for both ice motion events indicating that ridging dominates over melt driven changes. However, observed distributions of thick ice show a decrease in density up to an order of magnitude greater than the decrease predicted by melt alone (thin solid line). It is evident that level ice melt is insufficient to account for the observed melt of level ice even if no ridging is occurring and that contributions of ablation processes specific to ridged ice must be important.

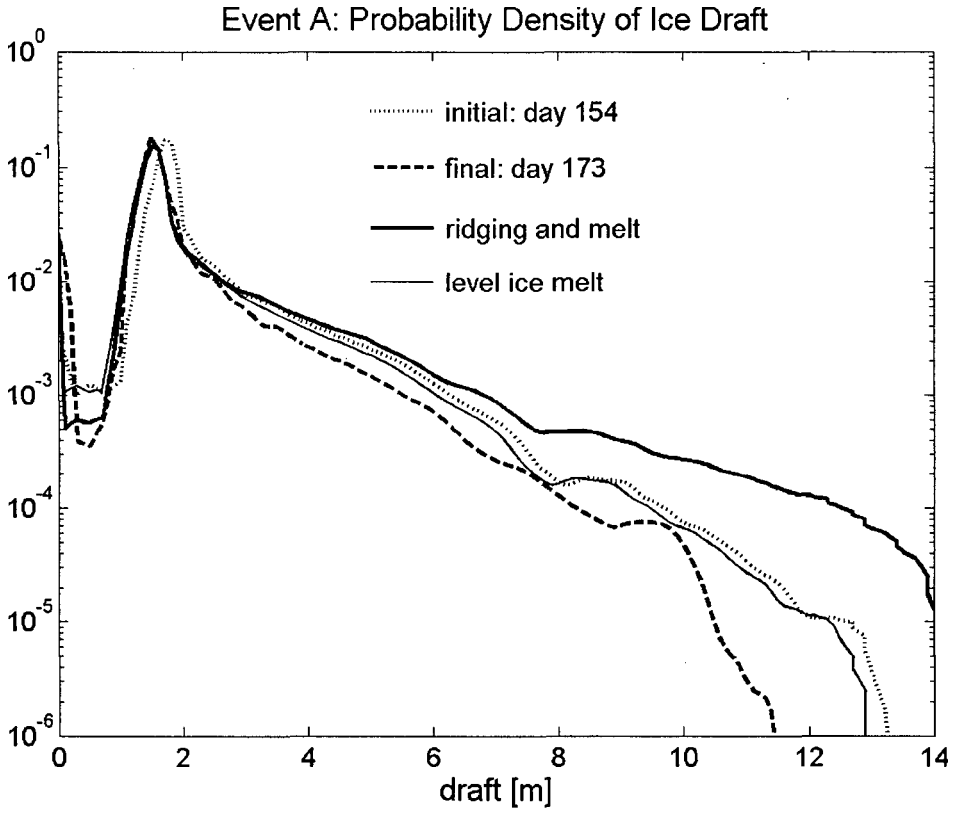

Figure 8-5: Probability density of draft (fraction per decimetre) for the modelled change in the distribution of ridged ice during summer melt from days 154 to 173. Allowing ridging to occur, the model predicts an increase in thick ice due to ridging (heavy solid line). Without ridging the model predicts a decrease in ridged ice density expected from observed level ice melt rates independent of draft (thin solid line). The observed thick ice shows evidence for an enhanced melt process, with density at large drafts decreasing faster than predicted (dashed line).

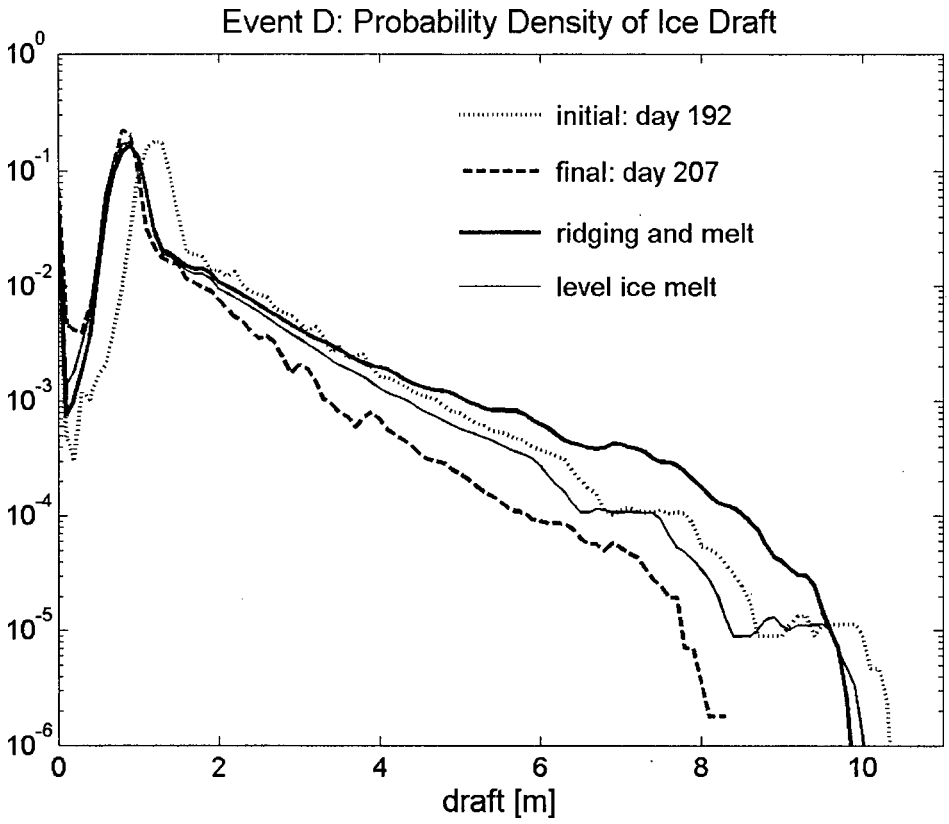

Figure 8-6: Probability density of draft (fraction per decimetre) for the modelled change in the distribution of ridged ice during summer melt from days 192 to 207. Similar to the results for event A, the amount of ridged ice is greatly overestimated by the model (heavy solid line). The model was run again without ridging (thin solid line) and the melt of ridged ice is clearly underestimated by the model.

8.4. Evidence for enhanced melting

Enhanced ablation rates of ridged ice in the draft distributions can be quantified from the shift in the cumulative draft density distributions, which are defined as all ice thicker than a draft value (in contrast to conventional definitions of cumulative distributions). For example, over event D, from days 192 to 207, the cumulative distributions shift to the left, indicating that ice is ablating (Figure 8-7).

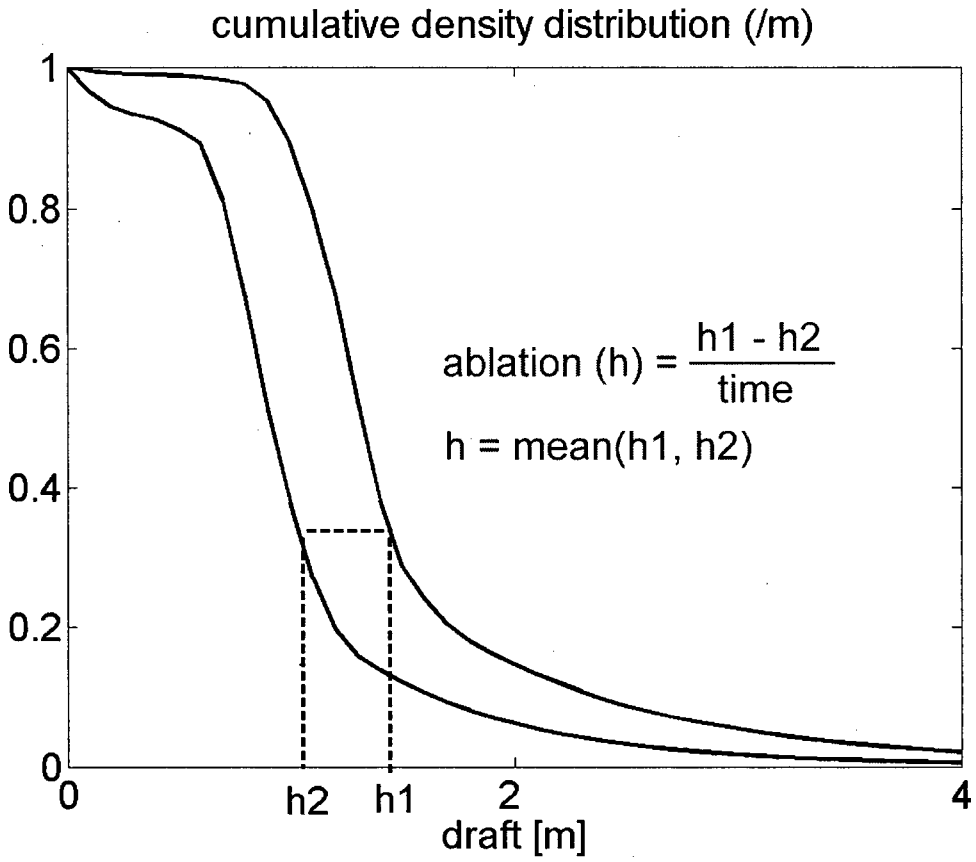

Figure 8-7: Determining ablation rates from the cumulative density distribution. Here the cumulative density distribution is defined to reach unity for the thinnest ice (open water), as the thickest ice is least prominent. The ablation rate can be found by subtracting the level ice thicknesses ($\Delta h = h1 - h2$) associated with a chosen value of the cumulative density and dividing Δh by the time separating the two distributions.

A lower bound for the ablation of ridged ice can be computed from observations, assuming that no new ridge building has occurred. Real melt rates will be considerably higher, as ridging acts to increase the distribution of ridged ice (Figure 8-5, Figure 8-6). However, as the truncation for maximum keel draft due to ice strength is unknown, ridging cannot be estimated with enough accuracy to predict true melt rates. Therefore, we use the observed ablation rates for the ice motion events (Figure 8-1) where the same ice is viewed consecutively as a lower bound. Values are plotted against draft in comparison for level ice melt rates in Figure 8-8.

The increase in melt with draft is visible in Figure 8-8. During event D (heavy dashed line), from days 192 to 207, the level ice melt is approximately 2-3 cm/day, while the observed ablation reaches up to 15 cm/day. Clearly, the melt rates needed to reproduce observed ablation are far greater than accounted for by one-dimensional thermodynamic level ice melt models.

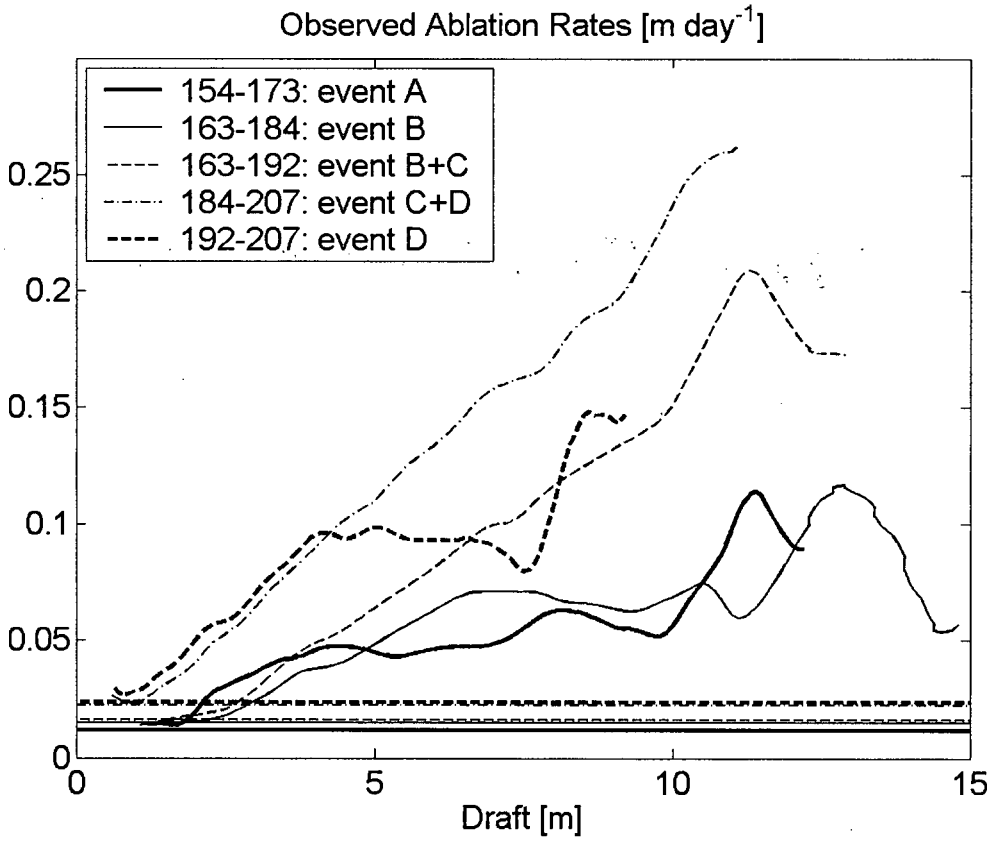

Figure 8-8: Observed ablation rates as a function of draft during four ice motion events. Level ice melt for these time periods is indicated by the dotted line of the same pattern. Both level ice melt rates and ridged ice ablation rates increase throughout the melt season.

Errors in the observed melt are calculated similar to section 4.4. Following Rothrock (1986) and Melling and Riedel (1995), the uncertainty in the cumulative distribution can be found as:

(8.4.1) $$\sigma(h) = \left[\frac{\Sigma g\,(1-\Sigma g)}{L/5} \right]^{1/2}$$

Where L is the total number of samples in the ice profile, the summation is over H to h, and the decorrelation distance for ridged ice is approximately 5 samples (see section 4.4). Using this estimate for the error in the cumulative density profiles, the maximum error on the observed melt can be found (Figure 8-9). This error is a generous overestimate, as the error in the initial and final cumulative density profiles should be independent, and thus should scale in quadrature. However, this error estimate demonstrates that observed melt rates are, at all times, much greater than the predicted melt rates of level ice.

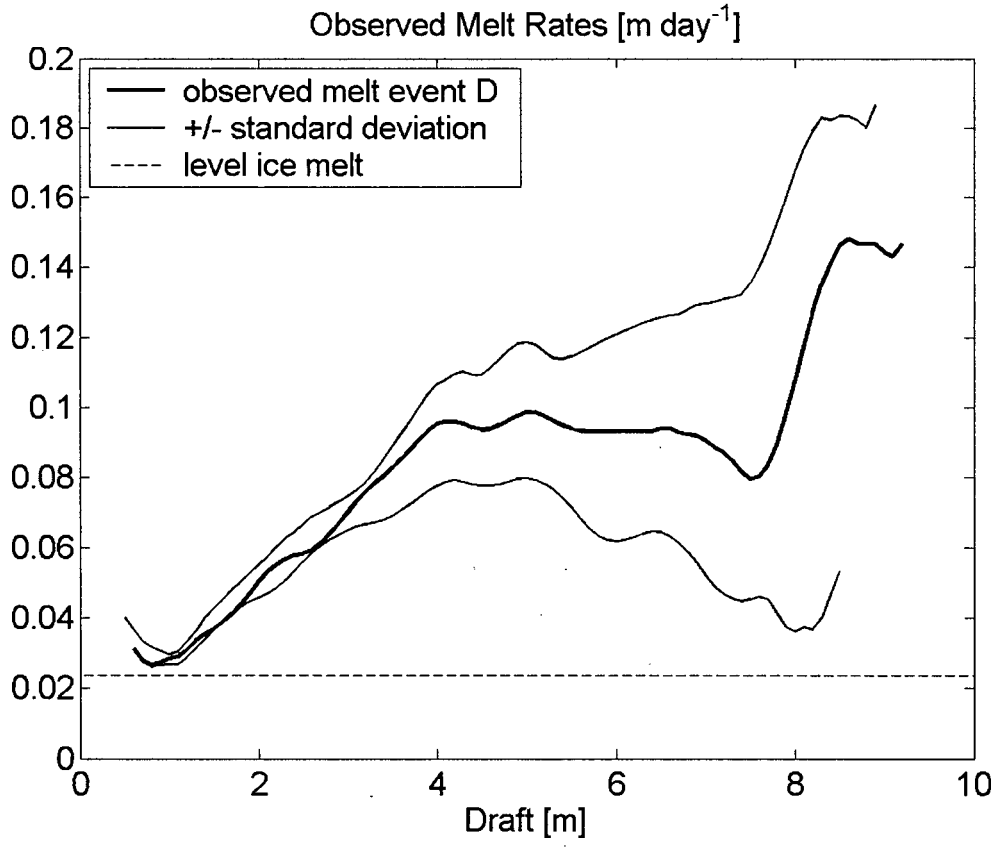

Figure 8-9: Observed melt for event D (thick line) with error (thin lines) representing the maximum errors using one standard deviation from the cumulative density distributions.

9. SUMMER RIDGE ABLATION PROCESSES

9.1. The influence of internal ridge geometry on ice melt

The observed enhanced melt rates of ridged ice (Figure 8-8) suggest that additional melt processes must work in tandem with level ice melt to ablate ridges. Several processes for enhanced melt have been proposed, such as increased surface area and enhanced flow past keels; common to each of these processes is the oceanic source of heat. Observational evidence supports this hypothesis; for example, Melling (2002) attributes observations of limited amounts of very thick ice within the Canadian Northern Arctic Archipelago (northeast of the region studied in this thesis) to melting from oceanic heat sources, rather than local surface atmospheric processes.

Schramm et al., (2000) used numerical models to investigate the importance of increased keel surface area to melt rates. The sloping sides of the keel were found to enhance thermal melt of ridged ice as much as three times that of level ice, but only for unrealistically narrow keels. This increase is insufficient to account for the present observations. An additional potential contributor to enhanced melt is accelerated flow in the upper ocean past ridge keels. The motion resembles a two-layer flow past an obstacle (Lawrence, 1993) and can be represented with hydraulic terminology. Using lab models designed to reproduce oceanic conditions, Pite et al., (1995) found enhanced flows past keels as predicted by hydraulic theory, with the flow characteristics dependent on mixed layer depth and upstream flow velocity. The enhanced flow has the potential to increase the turbulent heat transfer to the keel. However, quantifying this heat transfer is difficult.

It is likely that the increased turbulent heat flux generated by the two-layer flow past keels is a significant contributor to ice melt, however, results from the simulations of Skyllingstad et al. (2003) suggest that this may not account for all of the observed melt. Simulations of flow underneath ridge keels were compared with observations made during the SHEBA experiment by Skyllingstad et al., (2003). They found that keels caused both an increase in velocity and heat transfer near or at the keel. Modelling the interaction of the 0.5 m fresh layer and a keel extending 0.54 m deeper than the surrounding level ice showed heat flux values increased at the keel crest, to greater than 80 Wm^{-2}, during July 1998. Unfortunately, no large keels were simulated during this time period.

During the March 1998, the impact of a 10.8 m keel on the turbulent heat flux was simulated. Increased across-keel velocities at the keel crest of 0.5 m s^{-1} represented a significant increase on the average velocity of 0.1 m s^{-1}. Turbulent heat flux within the water column (Skyllingstad et al., 2003; Figure 7) indicates that for a freezing temperature departure of 0.05 °, upstream heat flux reached values of 120 W m^{-2}, whereas downstream values reached only 40 W m^{-2}, leading to average values of 80 W m^{-2}. As temperature scales linearly with heat flux, increasing the temperature departure to the expected July values of 0.2 ° (see 9.2) implies that heat flux could reach 320 W m^{-2}. If all of that heat were used to melt ice, the melt rates would be approximately 9 cm day^{-1}. Figure 8-8 suggests that events in July (days 183 to 213 of 2000) will have net ablation rates much higher than 9 cm day^{-1}, with total melt rates that are greater than 20 cm day^{-1}. It seems likely that turbulent heat flux is not the sole contributor to ridged ice melt and another process may play an equal or larger role.

We propose that an additional process contributing to enhanced melt of ridge keels is melt within the porous keel structure due to internal flow. Ice keels are constructed of blocks of ice that form porous structures with irregular envelopes. Fractal dimensions of the underside of first year sea ice (2.57 ± 0.06, Melling et al., 1993; 2.50 ± 0.05, Melling and Riedel, 1995, and 2.44 ± 0.064, Bowen and Topham, 1996) indicate that the envelope around a keel is rough with a high surface area to volume ratio. As undersea sonars measure only the envelope of the keel and do not recognize interstitial voids in the keel structure that are shadowed by lower blocks, the actual surface area to volume ratio is even higher than this estimate and the fractal surface is continued throughout the keel.

This fractal geometry is observed as porosity, which in first year sea ice ranges from 20-45% (Bowen and Topham, 1996) with a mean of approximately 30% (Timco and Burden, 1997). Studies of vertical ridge structure indicated that the porosity is highest in the keel sections, likely due to the lower relative gravitational packing forces in ridge keels compared with ridge sails (Lepparanta and Hakala, 1992; Melling et al., 1993). Measurements on Baltic first year ridges indicate that there exists a porous, non-consolidated keel bottom during the melt season (Hϕyland and Lϕset, 1999) with the consolidated layer expected to extend to 1.3 – 1.7 times the depth of the level ice. For large Beaufort Sea keels, this implies that most ridged ice has a porous structure.

During the winter of 1990, the evolution of a first year ridge in the Baltic Sea (Lepparanta et al., 1995) was monitored until its break-up in early May. The keel depth decreased from 5.28 m to 3.12 m over three visits spanning the period from the 4th of February to the 19th of April. During this time, the consolidated layer increased from 0.52 ± 0.19 m to 1.02 ± 0.31 m, reaching a final thickness slightly over 1.75 times the level ice thickness. While the overall ridge porosity decreased from 28% to 17% over the course of the two months, the porosity of the unconsolidated portion did not decrease and the change in porosity was due to the increasingly large volume fraction of consolidated ice. Porosity below the consolidated layer remained relatively constant at 31%, 29% and 32% for each of the three visits (Lepparanta et al., 1995). Immediately under the consolidated layer there was some evidence for decreasing porosity (to a minimum of 20%) due to packing rearrangements, but porosity was found to increase in the lower half of the keel (Lepparanta et al., 1995). Therefore, we can assume that porous ice is found in the lower regions of the keel throughout the entire melt season.

With such relatively high porosities in the lower portions of ridge keels, oceanic water may flow through the keels and transport heat to the central portions of thick, ridged ice. The relative rapid percolation of warm water "short circuits" the conductive transfer modelled by Schramm et al., (2000). A conceptual model is developed in chapters 9.3 to 9.7 to estimate the potential melt rates due to internal flow. We explore the potential of the combination of the fractal surface of the keels and the penetration of warm oceanic water into the keel structures to account for enhanced melt observed in ridged sea ice.

9.2. Under-ice ocean characteristics

The potential for melt within porous ridged ice depends on the physical characteristics of the upper layer of the ocean. For melt to occur, ice motion relative to ocean currents must be strong enough to induce flow through the porous keel and the ocean must be warm enough to melt the ice. While no upper ocean data are available from the Beaufort Sea during the 2000 melt season, comparisons with observations from previous years will be used to provide estimates for current speed and temperature.

Measurements taken from the 13th to 18th of April, 1989 in the Beaufort Sea Shelf using an ADCP attached to the ice (data courtesy H. Melling) provide average velocities with depth. The ice drifted at average velocities of 0.13 to 0.17 m s^{-1} in a westward direction within the regions bounded by 70.5 – 71.1 °N and 130.9 – 133.4 °W. This region includes site 3 (Figure 3-1). Ocean current speeds relative to the ice show mean speeds of 0.069 m s^{-1}, without significant variations in speed or direction with depth to at least 45m (Figure 9-1). There will be a reduction of ocean speeds at depths less than 10 m due to a non-slip boundary condition at the ice-ocean surface. However, for simplicity, the current velocity relative to the ice is assumed constant with depth as a first approximation.

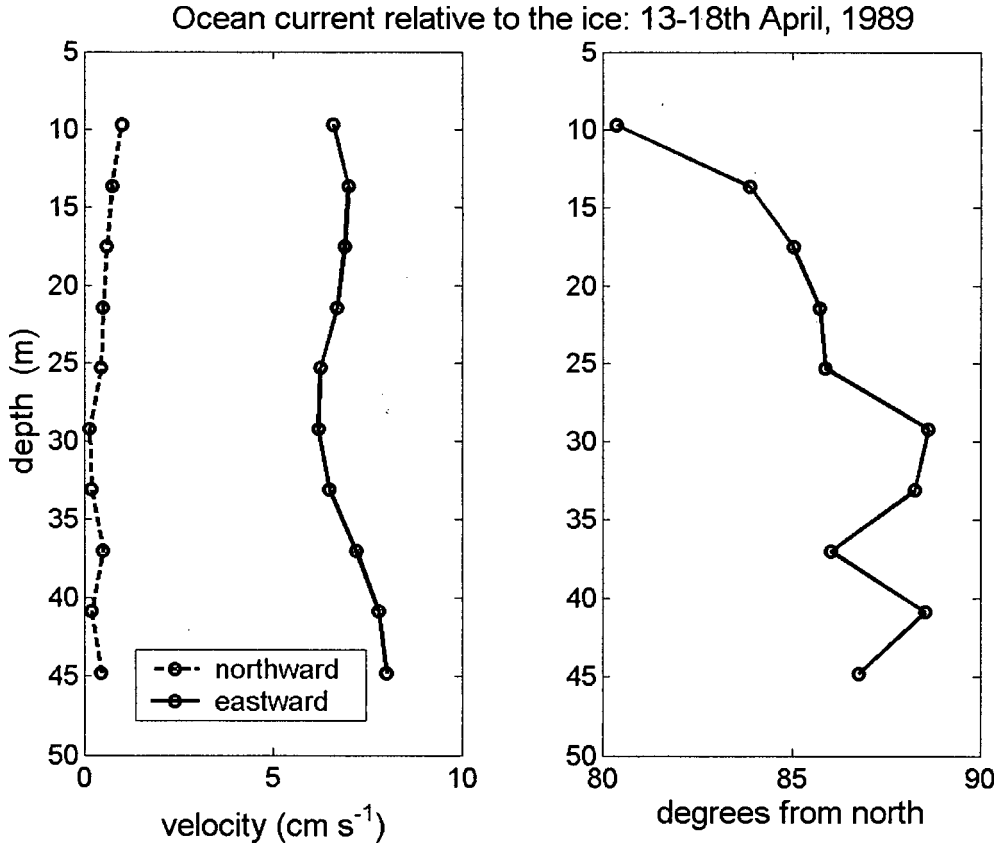

Figure 9-1: Components of oceanic velocity relative to level ice, 13-18th April 1989 in the Beaufort Sea. Level ice depth is 1.5 m, water depth is 54.6 m, and ice is moving westward. The direction and magnitude of the velocity remain relatively constant below the ice, with a mean speed of 6.9 cm s^{-1}. Data courtesy of H. Melling.

Deep ocean data from 1998 are available as part of the SHEBA (Surface Heat Budget of the Arctic Ocean) project (SHEBA data were provided by the SHEBA Project Office, Univ. of Washington. http://sheba.apl.washington.edu/). During the spring of 1998, data were collected at the SHEBA ice floe located within the area 74.6 – 80.5 ° N and 143.9-168.1 ° W. As part of that project, an oceanographic mast experiment was installed to measure the mean and turbulent ocean currents beneath the SHEBA ice floe. Instrument clusters were mounted on a pole 4 m apart below the ice surface. The mean velocity from the 5±1 and 9±1 m clusters provides a time dependent profile of the oceanic current speed through the melt season (Figure 9-2). Mean currents in April 1998 at 6 and 10 m depth were 0.12±0.02 m s^{-1} and 0.10±0.03 m s^{-1} respectively, higher than 1989 values (Figure 9-1). However, the current meters did not record currents below 0.05 m s^{-1}, increasing the apparent mean value.

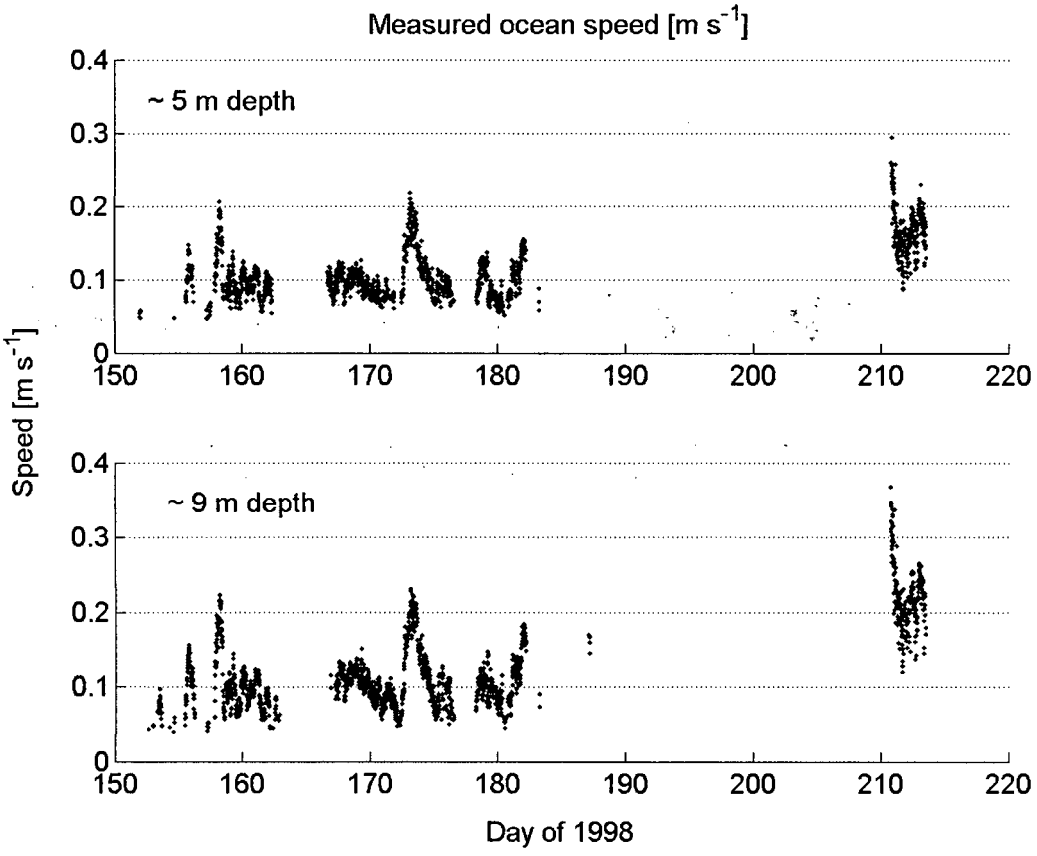

Figure 9-2: Velocity measured during turbulence measurements for the SHEBA program

Values of mean and standard deviations for the currents during the melt season are shown in Table 9-1. In June, the depth of the instruments was raised approximately 2m (at day 176). No data were collected during most of July, from days 185 to 210, due to biofouling and low currents that prevented data collection. The increased velocities at the end of July did not remain at that magnitude during August (Table 9-1) and may have resulted from a storm event during that three-day period of data collection.

Month	Depth (m)	Mean current (m s^{-1})	Standard deviation (m s^{-1})
June	4-6	0.102	0.028
	8-10	0.106	0.034
July	4	0.166	0.035
	8	0.218	0.045
Aug	3	0.135	0.033
	7	0.144	0.054

Table 9-1: Mean currents observed with depths during the SHEBA mast experiment in summer 1998.

The time series in Figure 9-2 suggest that the maximum expected oceanic current will be ~ 0.25-0.3 m s^{-1}, with more common speeds at 0.10 m s^{-1}. We assume that the mean current of 0.10 m s^{-1} will be aligned in a random direction to the keel axis. The component of velocity in the across keel direction will then be the average of 0.10 $\cos(\theta)$ m s^{-1} over the range of angles from 0 to an angle close to $\pi/2$ radians. For this range, the mean of $\cos(\theta)$ is 0.63 and the average velocity perpendicular to the keel is 0.063 m s^{-1}.

Ocean temperature and salinity profiles are also available from the SHEBA dataset. An automated CTD winch recorded profiles throughout the 1998 melt season. The ten-day mean temperature and salinity profiles during June and July, spanning days 150 to 210 of 1998, are plotted in Figure 9-3. It is expected that the upper 15 m of the water column under the ice will interact with ridge keels observed during this time. This layer appears to be homogeneous, with the mixed layer getting shallower through the melt season. For the salinity profiles, an upper fresh layer generated by ice melt begins to appear only after day 200. Temperature is largely independent of depth in the upper 15 m, with values increasing with time.

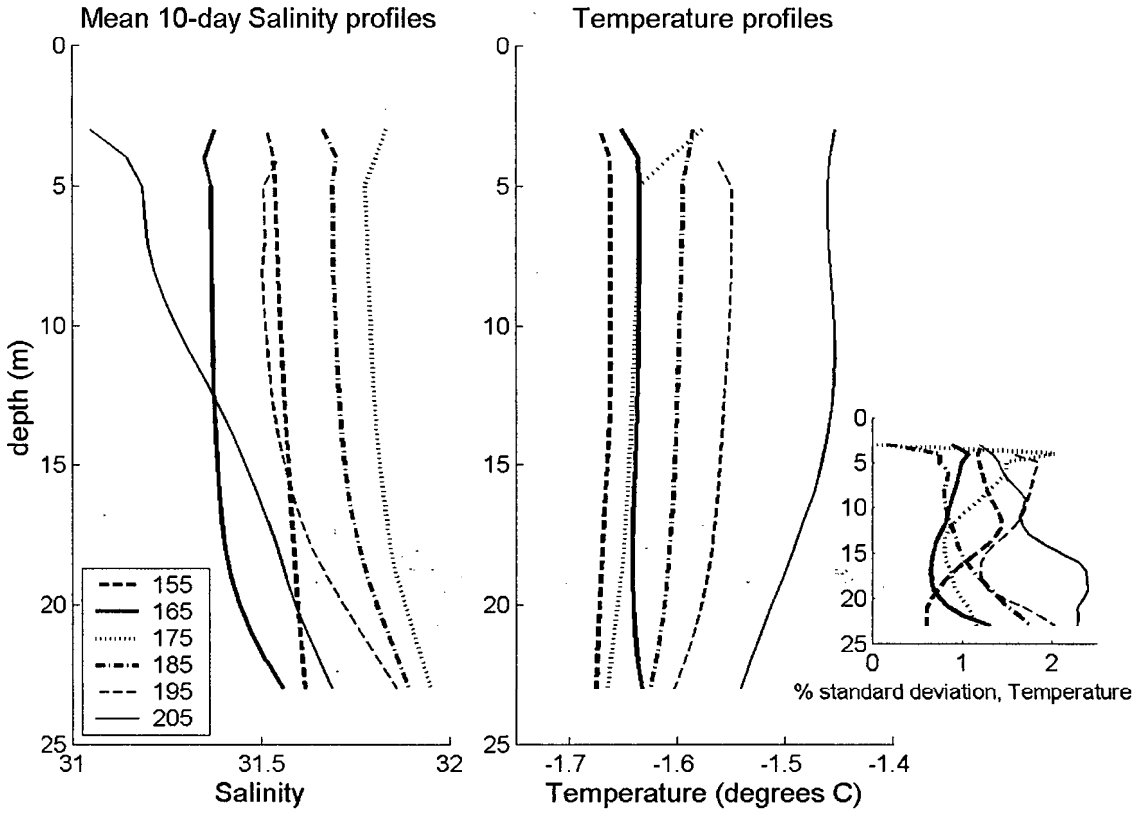

Figure 9-3: Mean temperature and salinity profiles from automatic CTD profiles collected during the SHEBA program in June and July 1998. Profiles show mean values over ten days, centred at days 155, 165, 175, 185, 195, 205.

Midpoint (day of 1998)	155	165	175	185	195	205
Mean temperature 3-10 m [°C]	-1.66	-1.64	-1.63	-1.59	-1.55	-1.50

Table 9-2: Mean ocean temperature over a ten-day period for depths 3m to 10m

The freezing point for seawater with a salinity of ~ 31.5 (over depths of 5-15 m) is approximately -1.73 °C. For all temperature profiles, the mean departure from this freezing point is sufficient to cause melt (Table 9-2). For the purposes of model development, the temperature anomaly above freezing is set at 0.18°C, similar to the observed mean temperature anomaly on day 195 in 1998.

9.3. Porous flow through the ice

The fractal envelope of ridged ice is the external manifestation a porous internal structure. Flow through porous media is well studied in groundwater and engineering literature and results can be adapted to the geometries of ridged ice. Consider the schematic of a ridge shown in Figure 9-4. Across-ridge flow is in the direction $\hat{x}$. As the orientation of the sonar survey line to the keels varies, the cross section viewed by the mooring sonar is generally significantly wider than the keel width. Further discussion of ridge cross-sections can be found in Section 11.1. Within the keel, the average direction of flow is assumed to travel in a net $\hat{x}$ direction and is similar to flow through any porous media. To estimate porous flow, Darcy's Law is used to describe the discharge velocity through a fluid filled medium.

$$V = KI_H \tag{9.3.1}$$

Where V is the discharge flow velocity, K is the constant of hydraulic conductivity [m s^{-1}], and I_H is the hydraulic gradient, given the subscript *'H'* to differentiate it from the identity matrix in section B, and related to the pressure gradient as (Batchelor, 1967, pp 224):

$$-\frac{1}{\rho_w \breve{g}}\frac{\partial P}{\partial x} = I_H \tag{9.3.2}$$

Here, P is pressure, ρ_w is the density of seawater, and ğ is the gravitational acceleration. Darcy's Law is valid when the Reynolds number, Re = uL/ν, is less than 1. The characteristic velocity within the pores is related to the discharge velocity, $u=V/p$ where p is the porosity, L is the length scale of the pores, and ν is the kinematic viscosity of seawater, $1.8\text{x}10^{-6}$ m^2 s^{-1}. For most groundwater systems, Re <1, and Darcy's Law is sufficient to predict porous flow. Ice keels, assuming pore length scales on the order of 1-20 cm (see Appendix B) and velocity scales on the order of 0.005-0.025 m s^{-1} (see section 9.5) will have Reynolds numbers ranging from 25-3000, indicating non-Darcy flow is occurring.

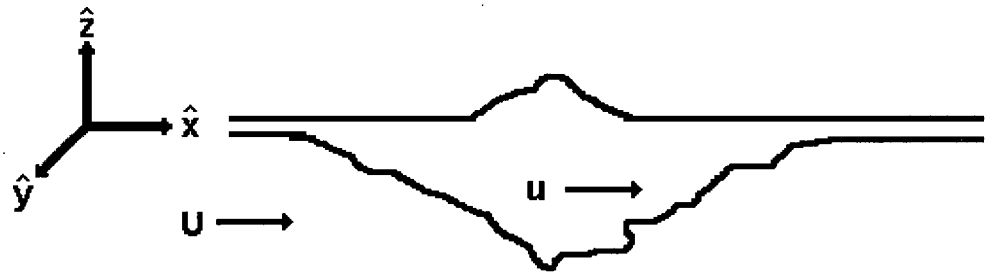

Figure 9-4: Keel schematic showing the definition of axes used in the theory. The oceanic velocity relative to the ice, U, and the porous flow through the ice, u, are in the direction of the ice motion $\hat{x}$.

An extension to Darcy's Law for slightly turbulent flows, the Forchheimer equation, includes an inertial component (Burcharth and Andersen, 1995).

$$I_H = K^{-1}V + K_I \,|V|\,V \tag{9.3.3}$$

where K_I [$s^2\,m^{-2}$] is an inertial coefficient.

A physical understanding of (9.3.3) can be obtained by examining the 1-dimensional steady flow case of the Navier-Stokes equation (Burcharth and Andersen, 1995). Consider the horizontal Navier-Stokes equation in one dimension for a non-rotating system (Gill, 1982)

$$\frac{Du}{Dt} = -\frac{1}{\rho}\frac{\partial P}{\partial x} + \nu\nabla^2 u \tag{9.3.4}$$

Where u is the velocity, ρ is the fluid density, and ν is the kinematic viscosity. As the flow is steady, we drop the time dependent terms. Rewriting (9.3.4) in terms of the hydraulic gradient (9.3.2):

$$-\frac{1}{\rho\breve{g}}\frac{\partial P}{\partial x} = \frac{u}{\breve{g}}\cdot\frac{\partial u}{\partial x} - \frac{\nu}{\breve{g}}\frac{\partial^2 u}{\partial x^2} \tag{9.3.5}$$

The first term on the right hand side is an inertial term while the second is a viscous term. Following Burcharth and Andersen (1995), we can relate (9.3.5) to the Forchheimer equation (9.3.3) by defining characteristic length (L) and velocity (u) scales for the fluid through the pores. This suggests an equation of the form:

$$I_H = \alpha \frac{\nu}{\breve{g}} \frac{u}{L^2} + \beta \frac{1}{\breve{g}} \cdot \frac{u^2}{L} \tag{9.3.6}$$

Here u is the pore velocity in the $\hat{x}$ direction, related to the discharge velocity, V as $u=V/p$. The characteristic pore length, L, is defined as the hydraulic radius, R_H, the ratio of pore volume to pore surface area. Burcharth and Andersen (1995) derive R_H for spherical granules. In the case of rectangular blocks of thickness h:

$$R_H = \frac{p}{(1-p)} \frac{h}{\gamma} \tag{9.3.7}$$

Full derivations of the hydraulic radius for spheres and blocks are in Appendix B. The factor γ is a geometrical factor related to the shape of the blocks forming the keel and is approximated as 4.45 (see Appendix B). The ratio of the porosity, p, to $(1-p)$ is the ratio of the fluid to solid fractions.

For our keels, the porosity in the lower portion of the keel is assumed constant at 0.3 (Lepparanta et al., 1995) and the hydraulic radius becomes R_H=0.096 h. When the keel is constructed out of 10 cm thick ice, the hydraulic radius will be 0.96 cm, and on a larger scale, for 1 m thick ice, the hydraulic radius will be approximately 9.6 cm.

Substituting R_H for L in (9.3.6) we find that u and I_H are dependent on ν, $\breve{g}$, and R_H, along with the parameters, α and β. No analytical derivation of these last two parameters exists, but they are expected to include information about the tortuosity, or interconnectedness of the pores (Burcharth and Andersen, 1995). The relationship between the hydraulic conductivity and the velocity becomes:

(9.3.8) $$I_H = \frac{\alpha \nu}{\breve{g} R_H{}^2} u + \frac{\beta}{\breve{g} R_H} u^2$$

In this form, (9.3.8) differs from the derived Forchheimer equation in Burcharth and Andersen (1995) by the factors of γ^2 and γ, which are included in R_H. Burcharth and Andersen (1995) include these factors (6^2 and 6 for spheres, from the d/6 dependence in R_H) in their parameters (here indicated as α' and β'). Care must be taken to remember these factors when estimating the discharge velocity using published values α' and β' for α and β in (9.3.8).

(9.3.9) $$\alpha = \frac{\alpha'}{36}, \beta = \frac{\beta'}{6}$$

A selection of values for α' and β' found in literature are summarized in Table 9-3. The coefficients in (9.3.3) are often reported, rather than the coefficients α and β. In these cases, α' and β' are calculated using the relations (Burcharth and Andersen, 1995; Wong et al., 1985):

(9.3.10) $$K^{-1} = \frac{(1-p)^2 \alpha' \nu}{p^3 \breve{g} h^2}; \quad K_I = \frac{\beta'(1-p)}{p^3 \breve{g} h}$$

For rough samples, h is chosen as the diameter at which 50% of the sample, by mass, has a smaller diameter, D_{50}. The uncertainty in this, along with a lack of information about the geometry of the grains makes determining the ideal values for α and β difficult. Table 9-3 illustrates the variation in coefficients found experimentally.

A first approach at determining the flow through a keel suggests that, based on experimental results with irregular shaped particles, α'and β' will vary from 400-1300 and 0.5-2, respectively. Adjusting these to the derivation of the Forchheimer equation for rectangular blocks, α and β will range from 11-37, and 0.08-0.34, respectively. Using literature values for K^{-1} and K_I in (9.3.3) is not desirable as the porosity of the non-spherical samples is much greater than the porosity of the ice keel.

Spherical Particles

	Englelund (1953)[1]	Hall et al., (1995)	van Gent (1995)
material/ packing	uniform rounded grains	75mm spheres	46mm spheres
Re		400-12800	170-1700
p		0.3	0.48
V			0.67-6.7 cms^{-1}
α'	~240	692	209
β'	~2.8	0.54	0.129

Irregular Particles

	Englelund (1953)[1]	Hall et al., (1995)	van Gent (1995)			Kells (1993)
material/ packing	irregular, angular grains	stone sample, mean diameter[2], D_{50} = 100mm	irregular shapes[3] D_{50} = 20 mm	D_{50} = 31 mm	D_{50} = 61 mm	rockfill, random grains. sub-angular to sub-rounded. D_{50}=18.6 mm
Re		5000-24000	74-740	115-1150	227-2270	
p		0.47	0.45	0.39	0.44	
V			0.67-6.7 cms^{-1}	0.67-6.7 cms^{-1}	0.67-6.7 cms^{-1}	
α'	up to 360 or greater	1200 (K^{-1}=0.06)	~1200 (K^{-1}= 1.81)	~700 (K^{-1}=0.89)	~1250 (K^{-1}= 0.23)	~400 (K^{-1}=1.27)
β'	up to 3.6 or greater	0.95 (K_I = 4.94)	1.06 (K_I =32.5)	0.64 (K_I=21.7)	0.55 (K_I=6.0)	1.71 (K_I = 96.4)

Table 9-3: Porous flow parameters. [1]Englelund (1953) data as reported in Burcharth and Andersen (1995). [2]Diameter is given as D_{50}, the diameter, for which 50% of the sample is smaller than by mass. [3]Three different rectangular irregular samples with their results are listed.

The large variations in α and β between experiments may be due to sensitivity to different packing arrangements (Kells, 1993) along with porosity, surface roughness, Reynolds number of pore velocity, particle size, and other factors (Burcharth and Andersen, 1995). For this reason, without experimental results specific to ice keels, the appropriate coefficients are unknown. A sensitivity study for the variation in pore velocity with α and β follows in section 10.2.

9.4. Pressure distribution on keel

To determine the discharge velocity through the keel, the pressure gradient across the keel must be known. Unlike the groundwater case, the pressure gradient is determined by the velocity component of the dynamic head, the upper ocean velocity, $\bar{U}$, relative to the ice. Bernoulli's theorem for an incompressible fluid states that energy is conserved along streamlines and defines a constant Ω (often called H, see Batchelor, 1967; section 3.5), where

$$\Omega = \frac{1}{2}\left|\vec{U}\right|^2 + E_I + \frac{P}{\rho} + \breve{g}z \tag{9.4.1}$$

In this equation, E_I is the internal energy of the fluid per unit mass and Ω is the total energy per unit mass. Ω is constant in a frictionless, non-conducting fluid with a steady pressure distribution. In a groundwater situation, the pressure gradient is normally driven by the change in the height of the water column, z, as the dynamic head from the velocity component is far smaller. In rivers or oceanic conditions it is the change in velocity, the dynamic head, which changes the pressure gradient. Holding Ω constant and changing the velocity ($\vec{U}$) will change the corresponding pressure aligned horizontally and normal to the keel axis, $\partial P/\partial x$ (Cummins et al., 1994):

$$\Delta P \approx \frac{1}{2}\rho\left|\vec{U}\right|^2 \tag{9.4.2}$$

The change in pressure from the upstream to downstream obstacle face can be related to the velocity as:

$$C_D = \frac{\overline{P}_{upstream} - \overline{P}_{downstream}}{(1/2)\rho\left|\vec{U}\right|^2} \tag{9.4.3}$$

Where C_D is the drag coefficient (Vittal et al., 1977). Determining the drag coefficient, C_D, is straightforward for an obstacle in a single-layer homogeneous flow. Pite et al., (1995) found that ice keel models in a homogeneous fluid had constant drag coefficients of 0.62 and 0.51, depending on keel shape.

Lab experiments measuring drag coefficients of river sediment bedforms showed similar results for the drag on triangular impermeable obstacles with shallow slopes (30°). In rivers, the drag coefficients, C_D, are found to vary with the ratio of the bed form height to stream depth, d_{layer}, as $C_D \sim (H/d_{layer})^{3/8}$ where H is the obstacle height (Thibodeaux and Boyle, 1987). Larger obstacles, where H/d_{layer} exceeds 0.35, may be related as $C_D \sim (H/d_{layer})^{3/2}$ (Shen et al., 1990; Elliot and Brooks 1997). Reported values for the drag coefficients range from 0.15 to 0.4 (Vittal et al., 1977).

For an ice keel floating on the ocean, the upper-layer depth is analogous to the river depth, but the buoyancy difference between the upper and lower ocean layers has a reduced gravity three orders of magnitude less than the air-water interface. The relative ease of displacement of the internal pycnocline in flow past a keel suggests that values for drag coefficients from non-stratified systems cannot be used here.

Pite et al., (1995) used laboratory models with two-layer flows to estimate the force on the ice keels. Scaling the laboratory simulation to ratios of the ice keel to upper-layer depth observed in the Arctic, Pite et al., (1995) found that the drag coefficient varied with the upstream Froude number of the flow, which ranged from 0.1 to 0.7 under typical Arctic conditions. Maximum values for the drag coefficient of approximately 3.8 were observed at Froude numbers of ~0.3-0.5. Drag coefficients decreased as the Froude number increased. Keel draft and upper layer water depths were not varied. Drag coefficients from a single model keel are shown in Table 9-4. In this experiment the layer and keel depths were kept constant (keel depth is one half of upper-layer depth) so variations in the Froude number were solely due to variations in flow velocity (Pite et al., 1995).

To effectively estimate the drag coefficient for an ice keel, the undisturbed internal Froude number, F_o, of the system should be known. Here the Froude number is defined following the notation of Pite et al., (1995):

$$F_o = \frac{U}{\sqrt{g' h_o}}; \; h_o = \frac{d_1 d_2}{d_1 + d_2} \tag{9.4.4}$$

Where U is the current velocity remote from the keel, g' is the reduced gravity ~ 0.005 m s^{-2} under typical Arctic conditions, and d_1 and d_2 are the upper and lower layer depths. For the keels at site 2 in the Beaufort Sea, we estimated the upper and lower layer depths as 15 and 55 m, respectively (using Figure 1-4 to estimate mixed layer depth). With an oceanic velocity of 0.063 m s^{-1}, the Froude number is approximately 0.26. For peak flows, exceeding 0.3 m s^{-1}, the Froude number will exceed 0.8. Observed keel depths in summer are on average less than 10 m deep, such that the keel depth is less than half the upper-layer depth, similar to Pite et al., (1995). Large keels will increase the velocity past the keel such that the full range of drag coefficients from 0.2 to 3.8 may be possible.

The sensitivity of heat transfer and pore velocity to the variations in the drag coefficient, C_D, will be explored further in Chapter 10.2. The drag coefficient is estimated as 3.5 for the purposes of this investigation to match the expected Froude number, 0.26, at oceanic velocities of 0.063 m s^{-1}.

F_o	0.23	0.34	0.44	0.53	0.69	0.84	1.01	1.23	1.64
C_D	3.5	3.8	3.5	3.0	1.4	0.77	0.46	0.31	0.20

Table 9-4: Experimental drag coefficients for a laboratory model of a keel in a stratified flow (Cummins et al., 1994). The drag coefficient decreases as the Froude number, and hence the current velocity, increases.

The drag coefficient gives information about the total pressure difference between the upstream and downstream faces of the ice keel, but does not provide information about the distribution of pressure across the upstream face. Pressure measurements from river bedform models indicate low pressure at the upstream end and crest of the obstacle with a maximum pressure partway along the upstream face and a constant, low pressure along the downstream face (Figure 9-5;

Vittal et al., 1977). We assume that the shape of the pressure distribution along the upstream face of a ridge keel is similar.

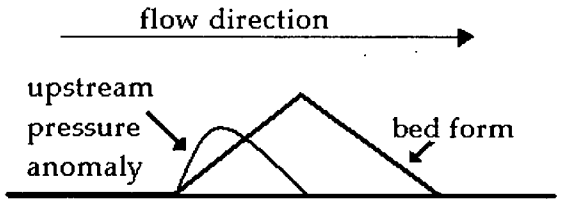

Figure 9-5: Distribution of pressure gradient along the flow direction on a bed form such as a sand dune at the bottom of a channel.

9.5. Pore velocity

Once the hydraulic pressure gradient is known, (9.3.8) can be solved for the pore velocity, *u (z)*. Equation (9.3.8) can be defined in terms of the hydraulic radius, R_H, as:

$$\frac{-1}{\rho}\frac{\partial P}{\partial x} = \frac{\beta}{R_H}u^2 + \frac{\alpha\nu}{{R_H}^2}u \tag{9.5.1}$$

In the simplistic model where the free-stream velocity is assumed constant with depth, the dependence on z reflects the fact that the keel width varies with depth, and thus $\partial P/\partial x$ is a function of depth; solving (9.5.1) for u gives:

$$u(z) = \frac{-\alpha\nu}{2\beta R_H} + \sqrt{\frac{\nu^2\alpha^2}{4{R_H}^2\beta^2} - \frac{R_H}{\rho\beta}\frac{\partial P}{\partial x}} \tag{9.5.2}$$

We expect that the pressure anomaly distribution is a function of the bed form shape (Figure 9-5) and reaches a maximum value along the upstream obstacle face before falling back towards zero at the keel crest (Vittal et al., 1977). The total pressure distribution must satisfy:

$$\int_h^H \Delta P(z)\,dz = \frac{1}{2}(H-h)C_D\rho U^2 \tag{9.5.3}$$

If we assume a parabolic shape for the pressure distribution, the simplest shape to satisfy the constraints at the keel boundaries, then the pressure drop across the keel (Figure 9-6) can be written as:

$$\Delta P(z) = \frac{3C_D \rho U^2}{(H-h)^2}((H+h)z - z^2 - Hh) \tag{9.5.4}$$

The pressure gradient as a function of depth depends on the width of the keel. An exponential distribution of ice draft within a keel can be expressed as:

$$b(z) = b_o e^{-z/\lambda}, \tag{9.5.5}$$

where b_o is a constant to conserve volume and λ is the e-folding scale. If we assume that the keel has a simple smooth shape, the keel width as a function of depth can be written as (see Appendix C):

$$\omega(z) = \frac{W(e^{-H/\lambda} - e^{-z/\lambda})}{e^{-H/\lambda} - e^{-h/\lambda}} \tag{9.5.6}$$

The pressure gradient across the keel (Figure 9-6) is then:

$$\frac{dP}{dx} = \frac{\Delta P(z)}{\omega(z)} \tag{9.5.7}$$

Using (9.5.7) we can solve for the pore velocity through the keel using (9.5.2). As the keel width must be finite at the maximum draft to be consistent with observations, in calculations for the discrete model (9.5.7) we set $H=H+\Delta h$, where Δh is the bin size in the internal melt model, here 0.1 m. We assume a porosity of 0.3, seawater density of 1024 kg m^{-3}, kinematic viscosity of 1.8 x 10^{-6} m^2 s^{-1}, and a hydraulic radius given by (9.3.7). The ocean current velocity relative to the ice drift is held constant at 0.1 m s^{-1}, the temperature anomaly above freezing is 0.18°C, and coefficients α and β are set at 20 and 0.11, respectively, based on results from van Gent (1995) for rectangular grains with a porosity of 0.39. This study was chosen as it has both the closest

porosity to ice keels and a range of Reynolds numbers in agreement with the expected Reynolds numbers in our application.

The calculations are made for a keel 9 m in draft, with block thicknesses of 0.5 m and a width to draft ratio of 6.8, and an e-folding scale of 4.2 m. These values are representative of the average keel shapes observed (Chapter 10). The impact of assuming these average geometries is discussed in Sections 10.5 and 10.6. Ice keels are assumed to be randomly oriented relative to the direction of current, so that a representative flow perpendicular to the keel is 0.063 m s^{-1} (see Section 9.2). The 9 m keel is chosen as it represents the largest keel observed during event D (Figure 8-1). The pore velocity increases with depth to a maximum velocity of 27.6 mm s^{-1} (Figure 9-6). The pore velocity at the keel draft is set to zero, as the block thickness within the keel, 0.5 m, is greater than the bin size used to calculate the pore velocity, 0.1 m, such that no porous flow is expected at the maximum draft.

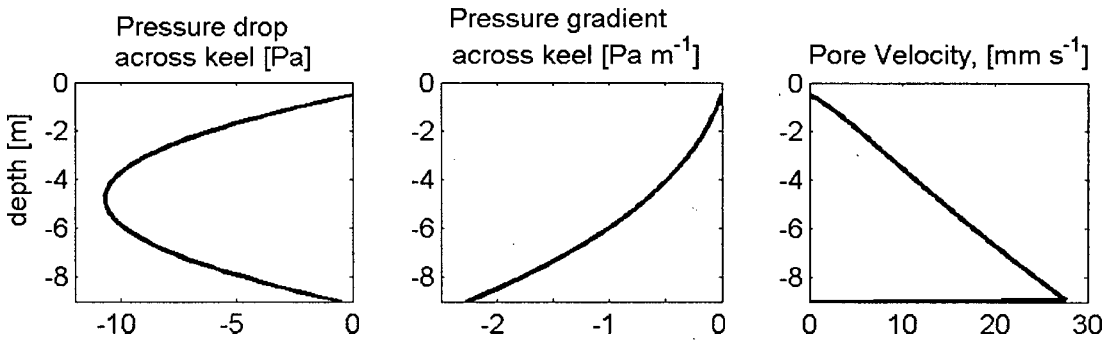

Figure 9-6: Distribution of pressure (9.5.4), pressure gradient (9.5.7), and pore velocity (9.5.2) through a 9 m keel with block thicknesses of 0.5 m and a ocean current of 0.1 m s^{-1}.

9.6. Heat transfer to a porous media

Analogous to the flow through tubes, once we know the keel discharge velocity, we can estimate the heat transfer from the fluid to the ice. For a pipe, the rate of heat transfer from the walls to the fluid can be expressed as (Bird et al., 1960):

(9.6.1) $$Q = \frac{Nu\kappa}{D} A \Delta T,$$

where κ is the thermal conductivity, D is the pipe diameter, Nu is the dimensionless Nusselt number, ΔT is the temperature difference between the fluid and the tube wall, and A is the area of contact.

Extension of this theory to porous materials such as packed beds or ice keels is achieved by replacing the pipe area, A, with the surface area of the pores, A_p. Essentially, the system can be envisioned as a network of connecting pipes, and Bird et al., (1960) noted the application of (9.6.1) to non-circular cross sections for turbulent flow can be accomplished by allowing D to be $4R_H$, four times the mean hydraulic radius. We judge the flow through the keel to be close to turbulent for the purposes of this discussion.

From Appendix B, the surface area of the blocks, A_p, is given as:

(9.6.2) $$A_P = 2N\left(b_1 b_2 + b_1 + b_2\right)h^2,$$

where N is the number of blocks in a volume of ridged ice, V_K, and is given by:

(9.6.3) $$N = \frac{(1-p)\,V_K}{b_1 b_2 h^3}$$

Substituting in for N, and recalling that R_H is defined as $p\,h\,/(\gamma(1-p))$, the surface area of the blocks for a keel volume $V_K = dx\,dy\,dz$ is given by:

(9.6.4) $$A_P = \frac{2(1-p)\left(b_1 b_2 + b_1 + b_2\right)V_K}{b_1 b_2 h} = \frac{(1-p)\gamma V_K}{h} = \frac{p\,dx\,dy\,dz}{R_H}$$

Equation (9.6.1) can be written as the heat flux, Q_m/dx, to the keel ice from the water along the x direction as (Bird et al., 1960):

(9.6.5) $$\frac{Q_m}{dx} = \frac{Nu\,\kappa\,p\,dydz}{4R_H{}^2} T_x$$

Where Q_m is the heat generating melt, and T_x is the temperature above freezing of the water at x.

A new parameter in (9.6.1) and (9.6.5) is the Nusselt number, *Nu*. For fluids where the variation in viscosity is negligible (such as seawater, whose viscosity varies on the order of 1% per degree temperature; Batchelor, 1967), turbulent Nusselt numbers are given as (Bird et al., 1960; Knudsen and Katz, 1958):

$$Nu = 0.023\,\mathrm{Re}^{0.8}\,\mathrm{Pr}^{1/3} \tag{9.6.6}$$

where Pr is the ratio of the molecular diffusivity of momentum to the molecular diffusivity of heat and is called the Prandtl number (Knudsen and Katz, 1958). The Prandtl number is estimated as 13.6 (Holland and Jenkins, 1999). The Reynolds number defined here uses the diameter of the porous system, $4R_H$, as its length scale (Bird et al., 1960). The turbulent form of the Nusselt number, (9.6.6), is applicable for Reynolds numbers greater than 20,000. Here, with a peak velocity of 24 mm s^{-1} and R_H=0.05 (for h=0.5), the Reynolds number is approximately 2500, less than the fully turbulent regime, but greater than laminar Reynolds numbers. As no simple parameterization of the Nusselt number for the transition region between laminar and turbulent flow exists, and the nature of the flow path through the porous media would intuitively increase turbulence, the turbulent Nusselt number is used as a best approximation.

9.7. Melt of ridged sea ice

For melting ice, this heat transfer model is complicated by the facts that not only will the temperature change due to the heat flux, but the melt will also result in an increasing volume of water. Considering the ice-water system as a packed bed box model, the conservation of volume flux through the ice pore can be written as:

$$(u_x - u_o)p^{2/3}dy\,dz = \int_0^x \frac{Q_m}{\rho_i L_i}dx \qquad or$$

$$(u_x - u_o)p^{2/3}dy\,dz = \frac{Nu\,\kappa\,p\,dy\,dz}{4R_H{}^2\rho_i L_i}\int_0^x T_x dx \tag{9.7.1}$$

and can be rewritten as:

$$u_x = \frac{Nu\,\kappa\, p^{1/3}}{4\rho_i\, L_i\, R_H{}^2} \int_0^x T_x\, dx + u_o\,, \tag{9.7.2}$$

where u_o is the initial velocity of the flow, x is the along tube distance, L_i is the latent heat of fusion for ice, 334000 J kg^{-1}, ρ_i is the density of sea ice, 920 kg m^{-3}, and ρ is the density of seawater, 1024 kg/m^3. Note that the subscripts *o,m,x* indicate input, melt, or along channel flow in the $\hat{x}$ direction respectively, and do not indicate a derivative. This notation is used for the remainder of the thesis.

Similarly, for conservation of heat flux, Q, the equation Q_o-Q_m=Q_x becomes:

$$T_o \rho u_o c_p\, p^{2/3} dydz - \frac{Nu\,\kappa\, p\, dydz}{4R_H{}^2} \int_0^x T_x\, dx = T_x \rho u_x c_p\, p^{2/3} dydz \tag{9.7.3}$$

which reduces to:

$$\int_0^x T_x\, dx = \frac{4R_H{}^2 \rho c_p}{Nu\,\kappa\, p^{1/3}} (T_o\, u_o - T_x u_x) \tag{9.7.4}$$

where c_p is the heat capacity of seawater, 4218 J kg^{-1} K^{-1}. Using (9.7.2) for u_x in (9.7.4), we find the equation for the heat transfer through a packed bed is:

$$\int_0^x T_x\, dx + \frac{\rho c_p}{\rho_i L_i} T_x \int_0^x T_x\, dx = \frac{4R_H{}^2 \rho c_p u_o}{Nu\,\kappa\, p^{1/3}} (T_o - T_x)\,, \tag{9.7.5}$$

where $T_x(0)$=T_o. This is a complex differential equation of the form:

$$y + \alpha\, y \frac{dy}{dx} = \beta(T_o - \frac{dy}{dx}); or \quad \frac{dy}{dx} = \frac{\beta T_o - y}{\beta + \alpha\, y}$$
$$where \quad y = \int_0^x T_x dx \tag{9.7.6}$$

The solution for (9.7.6) can be written in terms of the Lambert W function (Corless et al., 1996) as follows:

$$We^{W} = \frac{-\alpha\beta T_o}{\beta(1+\alpha T_o)} \exp\left[\frac{-x-\alpha\beta T_o}{\beta(1+\alpha T_o)}\right] \qquad (9.7.7)$$

$$and \quad W = \frac{\alpha(y-\beta T_o)}{\beta(1+\alpha T_o)}$$

To solve for T_x, (9.7.7) can be solved for y. This was done using the built-in Matlab/Maple solver for the Lambert W function (Corless et al., 1996).

Once T_x is known, the heat flux from the water to the keel can be found from (9.6.5). Using the above equations for a hypothetical keel 9 m in draft, 60.8 m wide, and constructed out of blocks 0.5 m thick, produces internal heat flux and water temperatures as shown in Figure 9-7.

From the heat flux, the enhanced melt rates for ridged ice can be calculated as the summation of the internal melt within the keel divided by $(1\text{-}p)^{1/3}$, to account for the decrease in pore volume, assuming that repacking maintains a constant porosity. Figure 9-8 shows the internal melt rates compared with observed level ice melt rates. The internal melt rate for ice within a 9 m keel is slightly less than the observed ridged ice melt at 9 m from event D (days 192 to 207), over all keels, but much greater than the level ice melt alone, suggesting that internal melt may be an important contributor to the enhanced melt of ridged sea ice. Level ice melt during event D, 23.6 mm day^{-1}, is less than the contribution from internal melt for all ridged ice greater than 4 m. The melt rate increases with ridge draft, consistent with the observations of Rigby and Hanson (1976). Note that the modelled rates of melt are tied to a plausible guess for the value of T_o (0.18 K). The actual value is not known.

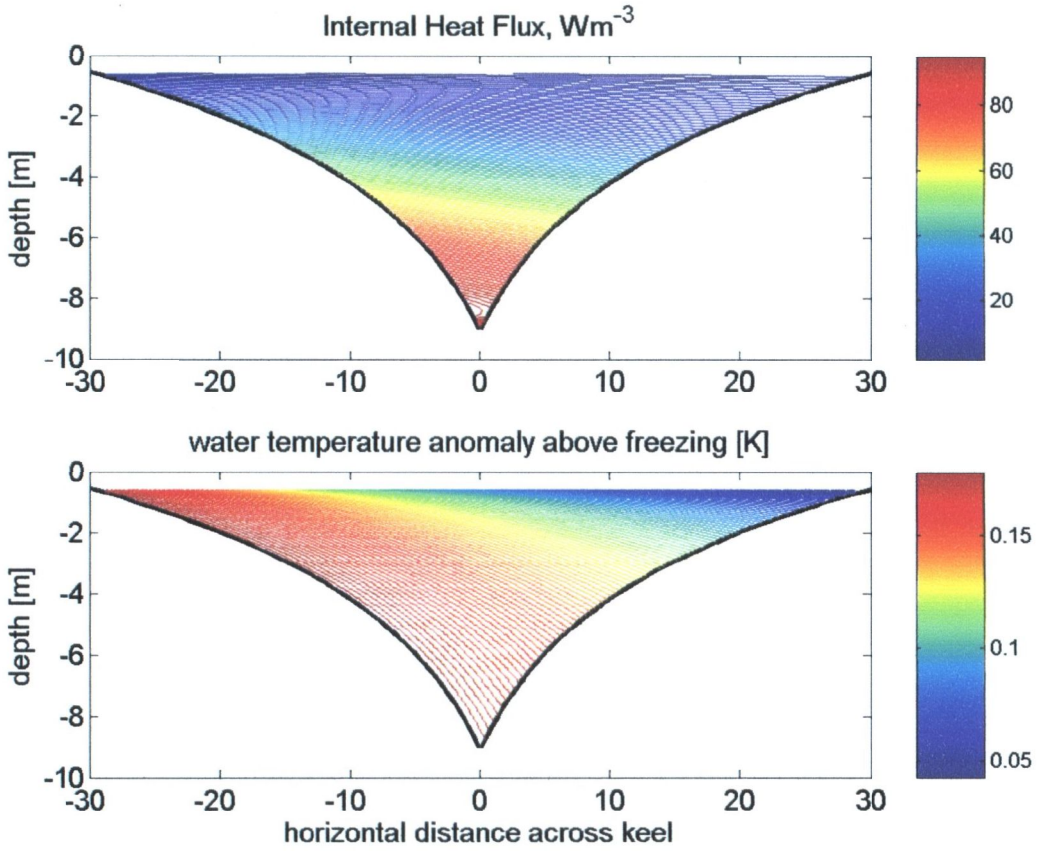

Figure 9-7: Top: Internal heat flux through keel showing the decrease in heat transfer across the keel. Bottom: Change in the water temperature through the keel due to the heat lost to melt and the influx of fresh water at the freezing point. At deeper drafts the water flows faster (from left to right on figure, see Figure 9-6) moving further through the keel before the water reaches the freezing temperature. Keel porosity is 0.3 and block thickness is 0.5 m.

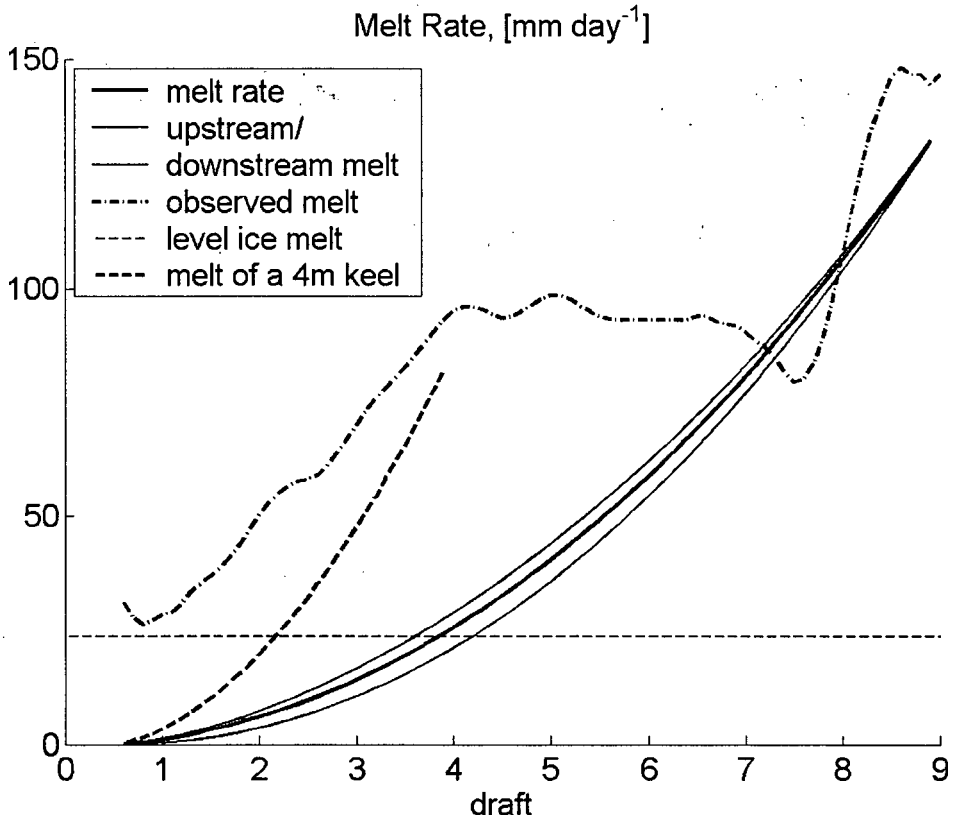

Figure 9-8: Melt rates from porous flow through a keel 9 m (heavy black line). Thin black lines show the melt rates upstream and downstream of the keel crest. Expected melt from level ice is shown as the thin dashed line, observed melt rates are shown as a thick dash-dot line. The melt rate from a small 4 m keel is shown for comparison (heavy dashed line). Keel porosity is 0.3 and block thickness is 0.5 m for both keels.

The bulge in observed melt in the range of 3 to 6 m of draft can be explained as a feature of the keel population. The internal melt rates from a 4 m keel constructed of 0.5 m thick blocks are shown on Figure 9-8 (heavy dashed line). A keel population with many keels in the size range of 3-6 m may lead to the observed bulge. A more accurate comparison of observed and internal melt rates will be discussed in chapter 11 when the melt rates for keels are combined with the keel population to develop a statistical ridged ice internal melt rate.

Equation (9.7.5) is complicated by the inclusion of the melt water to the porous flow. For a 9 m keel with blocks 0.5 m thick, the increase in flow velocity due to melt is much smaller than the

porous flow. Figure 9-9 shows that the addition of melt water to the porous flow through the keel adds only a maximum of 0.007 mm s^{-1} to the flow at a depth of 3.2 m. The ratio between the input from melt to the initial porous flow is less than 0.1 %, and the assumption that $u_o=u_x$ is justified for the internal melt model. Because the influx of melt water is small (Figure 9-9) and can be neglected, $u_x=u_o$ and (9.7.4) can be solved directly to give a solution for the temperature:

$$\int_0^x T_x\,dx = \frac{4\rho c_p R_H{}^2 u_o}{Nu\,\kappa\, p^{1/3}}(T_o - T_x)\,, \tag{9.7.8}$$

or,

$$T_x = T_o\, e^{-\frac{Nu\,\kappa\, p^{1/3}\, x}{4\rho u_o\, c_p\, R_H{}^2}} \tag{9.7.9}$$

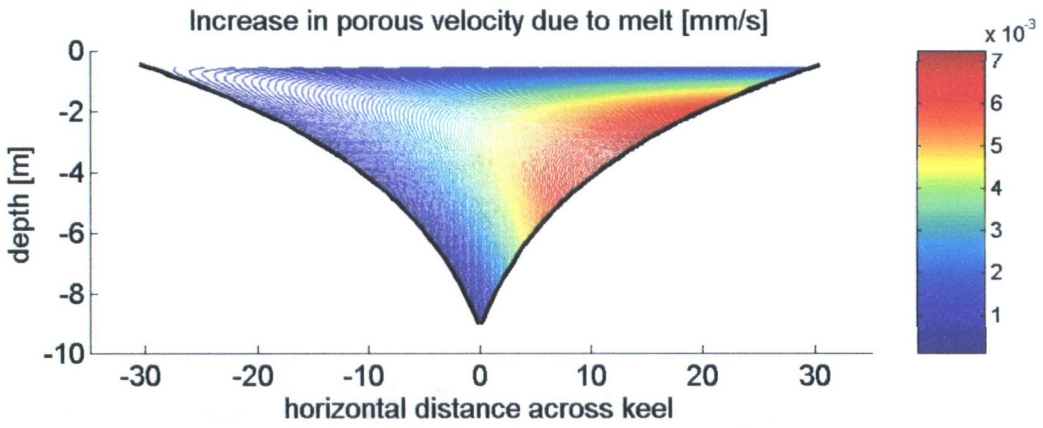

Figure 9-9: Top: Porous flow velocity due to melt through the keel. Increase in melt is very small compared with porous velocities that can exceed 20 mm s^{-1} (Figure 9-6). Keel porosity is 0.3 and block thickness is 0.5 m.

10. MELT WITHIN A SINGLE KEEL

10.1. Model sensitivity

The internal melt model developed in chapter 9 is an initial estimate that combines estimated keel and ocean parameters, empirical formulas, and simplifying assumptions. To calculate the porous flow we used estimates for the Forchheimer coefficients from similar, but not identical, physical systems. For the estimation of the pressure gradient we relied on laboratory tests to estimate the drag coefficient across the keel. To calculate heat transfer, we used a form of the Nusselt number applicable to fully developed turbulent flow, although Reynolds numbers indicate that internal flow will be in the transition region between laminar and turbulent. Finally, we assume that the porous flow can be approximated with a one-dimensional model, although melt may introduce buoyancy-driven vertical flow within the keel. All of these assumptions and estimations introduce some uncertainty into the calculated melt rates. In this chapter we investigate the consequences of these assumptions on the predicted melt rates and show that, while melt rates may vary, the ability of the internal flow to melt ridged ice at melt rates comparable or greater than level ice melt is maintained.

10.2. Sensitivity of melt to parameters for porous flow

To find the pore velocity through the keel, the Forchheimer equation (9.5.2) utilizes the parameters α and β. The appropriate values for α and β for this system are unknown. A review of the literature and personal communications with civil engineers reveal that no research has been conducted for flows with similar Reynolds numbers and material with similar block dimension ratios. We therefore chose to use values for α and β that represent a similar system of irregular shapes with appropriate Reynolds numbers (115-1150, van Gent, 1995). However the porosity for this system was higher (0.39) than the average porosity of ridged ice (0.3, Timco and Burden, 1997) and the particles were much smaller with a median (by mass) dimension of 61 mm.

To determine the uncertainty in flow velocities with α and β, we compared flow estimates over a range of published coefficients (Table 9-3). In the literature, α and β are found to range from 11-37, and 0.08-0.34, respectively. Calculating the velocity through the keel for this range of coefficients, increasing α and β will decrease the pore velocity (Figure 10-1). The maximum

velocity changes by a factor of 2.2, from 27 mm s^{-1} to 12 mm s^{-1} for a 9 m keel with 0.5 m level ice blocks and an ocean current velocity of 0.1 m s^{-1}. The velocity through the keel at 5 m depth varies by a factor of 2.2 for the same keel.

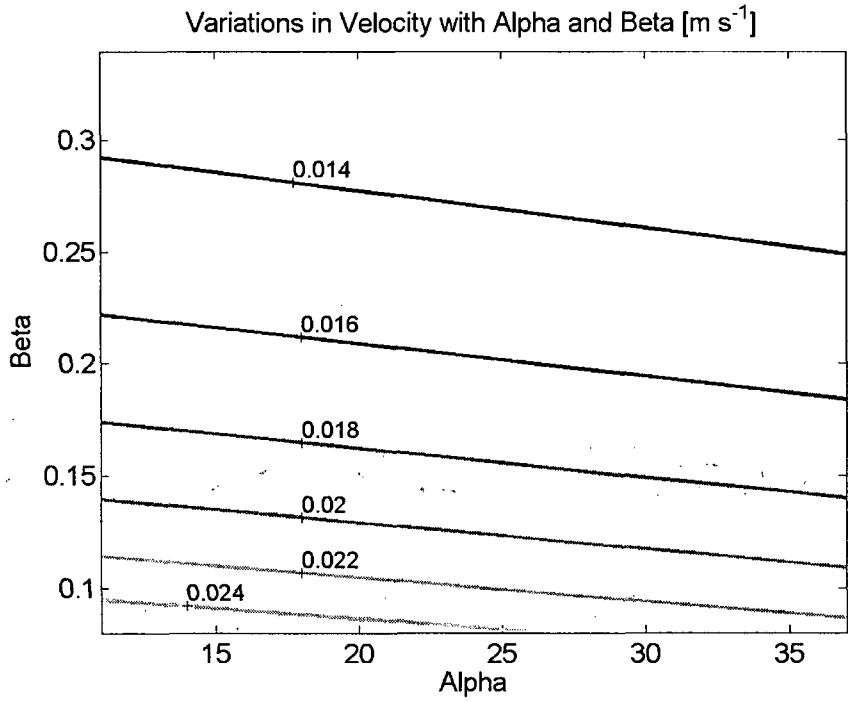

Figure 10-1: Variations in calculated maximum pore velocity for various coefficients α and β.

Further confidence in our choice of α and β is found when we calculate the porous flow velocity using values for α and β that corresponds to a packed bed of spheres with a porosity of 0.3, similar to ice (Table 9-3; Hall et al., 1995). From values for α' and β' we find that $\alpha = 19$ and $\beta = 0.09$ using (9.3.9). This introduces a 9% change in the porous velocity (Figure 10-1), only a small variation from the velocity found using van Gent's (1995) values. As the values of Hall et al., (1995) correspond to a system with an appropriate porosity, and the values of van Gent (1995) correspond to irregular shaped particles that may better represent the blocks of ice within a keel, it seems reasonable to assume that true values for α and β will not introduce large errors into the porous velocity.

As the equation for water temperature (9.7.9) depends on velocity as an exponential, and the e-folding scale of that negative exponential varies as u_o/Nu, the e-folding scale for heat transfer will vary with the pore velocity to the $1/5^{th}$, $u_o^{1/5}$. However, since the rate of heat transfer from the water to the ice varies as $u^{4/5}$ (9.6.5), increases in velocity will correspond almost directly to increased melt rates. Thus, over the entire range of Forchheimer coefficients, the internal melt rates vary by approximately a factor of 2 and will not effect the basic capacity for internal melt to contribute to the enhanced melt of ridged ice.

A further variation in the pore velocity is introduced by the influx of melt water which acts to increase pore velocity. The Forchheimer equation is derived for a constant porous flow. Increasing that flow volume will decrease the pressure gradient, $\partial P/\partial x$, and thus decrease the pore velocity according to (9.5.2). As the influx of melt water will increase the flow by less than 1% (Figure 9-9), the Forchheimer equation (9.3.6) can be written by expressing the pore velocity, u_x, as a perturbation from the initial flow $u=u_o+u'$:

$$\frac{1}{\rho}\frac{\partial P}{\partial x} = \alpha\nu\,\frac{u_o + u'}{{R_H}^2} + \beta\frac{(u_o + u')^2}{R_H} \tag{10.2.1}$$

The adjustment in the pressure gradient due to u' can then be written as:

$$\frac{1}{\rho}\frac{\partial P'}{\partial x} \approx \alpha\nu\,\frac{u'}{{R_H}^2} + 2\beta\frac{u_o u'}{R_H} \tag{10.2.2}$$

and as u' is less than 1% of u_o, and all the terms on the RHS are less than 1% of their undisturbed values, the decrease in the pressure gradient is minimal. Finally, as the velocity depends on the square root of the pressure gradient (see (9.5.2)), u is not extremely sensitive to small variations in $\partial P/\partial x$ and the impact on the melt rate will be negligible.

The final parameter impacting the pore velocity is the choice of the drag coefficient, C_D=3.5. The impact of the drag coefficient on the pressure gradient is linear (9.5.4) and the impact on the pore velocity, obtained from (9.5.2), is $C_D^{1/2}$. Over the range of coefficients (3.8 to 1.4; Cummins et

al., 1994) associated with Froude numbers typically found in the Arctic (0.1 to 0.7; Pite et al., 1995), the impact on the pore velocity is thus less than a factor of $(3.8/1.4)^{1/2}$, or 1.65.

The change in pressure over the whole keel is proportional to $\frac{1}{2}\rho C_D U^2$ (9.5.4). Using the laboratory results of Pite et al., (1995) reported in Cummins et al., (1994), the impact of various drag coefficients on the pressure gradient can be found by computing $F_o^2 C_D$ (Table 10-1), as the Froude number, F_o, is directly related to U (9.4.4). For all Froude numbers greater than 0.3, the increase in the drag coefficients corresponds to a decrease in the Froude number (and ocean current velocity) leading to a constant ratio of $F_o^2 C_D \sim 0.5$.

An immediate application of this result is the impact of storm events on the melt rates. Following from Table 10-1, we see that once the ocean current increases such that the Froude number exceeds ~0.3, the pressure gradient will approach a constant value approximately 250% greater than when the Froude number is 0.23 (Table 10-1). This increases the pore velocity by a maximum factor $2.5^{1/2}$, or 1.6 (9.5.2). Storm events may then increase the rate of heat transfer to the ice by a factor of $u^{4/5}$, (9.6.5), and thus have the capacity to increase melt rates over short time scales by a factor of approximately 1.5.

However, the drag coefficients in Table 10-1 are based on one data set where keel drafts are kept constant at 50% of the mixed layer drafts. In the Arctic, keels will be of varying shapes, sizes, and drafts and further research about the drag coefficients for the wide variety of naturally occurring keels is needed to increase confidence in the drag coefficient.

F_o	0.23	0.34	0.44	0.53	0.69	0.84	1.01	1.23	1.64
C_D	3.5	3.8	3.5	3.0	1.4	0.77	0.46	0.31	0.20
$F_o^2 C_D$	0.19	0.44	0.68	0.84	0.67	0.54	0.47	0.47	0.54

Table 10-1: Experimental drag coefficients for a laboratory model of a keel in a stratified flow (Cummins et al., 1994).

10.3. Sensitivity of melt to parameters for heat transfer

With a known porous velocity through the keel, the heat transfer from the water to the ice can be calculated. This heat flux is dependent on the Nusselt number, *Nu*, which influences both the

temperature of the pore water given by (9.7.9) and the heat flux to the ice given by (9.6.5). The Nusselt number used to calculate heat transfer is designed for turbulent flows (Bird et al., 1960); however, Reynolds numbers for a flow through a keel indicate that the flow may not be fully turbulent. The transition region from laminar to turbulent flow is not well understood, as it is usually avoided in experimental design for engineering research (Bird et al., 1960). However, a comparison with laminar Nusselt numbers for heat transfer in tubes is useful. Here, the laminar Nusselt number is $Nu=1.86(Re\ Pr\ (4R_H/l))^{1/3}$ (Bird et. al., 1960), where l is a length scale we approximate as the keel width. The laminar Nusselt number is within a factor of 2 of the turbulent Nusselt number for a 9 m keel with block thickness of 0.5 m, indicating that errors introduced by the choice of Nusselt number do not influence the general ability of a porous melt model to contribute significantly to the enhanced melt of ridged ice. Without further information about the turbulent characteristics of the flow, no further refinement of the Nusselt number is possible.

10.4. Stratification and stability: 2-d components of fluid flow

For simplicity, the Forchheimer model used here to predict fluid flow is 1-dimensional. This assumption implies that no significant flow in the vertical direction is present. This would be incorrect if the change in density of the pore water, due to the influx of fresh water, was large enough to drive vertical flow. However, the fresh water influx is very small compared to the porous flow, less than 0.2 % (Figure 10-2), and the change in pore water density through the keel (Figure 10-3) is both very small, and stably stratified, hence the assumption of horizontal flow is valid.

While the fresh melt water may not influence flow within the keel, the volume of fresh water produced by internal melt is not insignificant. Integrating the flux of melt water over the keel, the melt produces 3.5 m^3 of fresh water per day, exceeding the fresh water production from an equal area of level ice. The discharge flow from the keel is not fresh however, but well mixed with the flow of ocean water through the keel and thus would not create a distinct fresh layer under the ice, but would increase stratification within the upper water column.

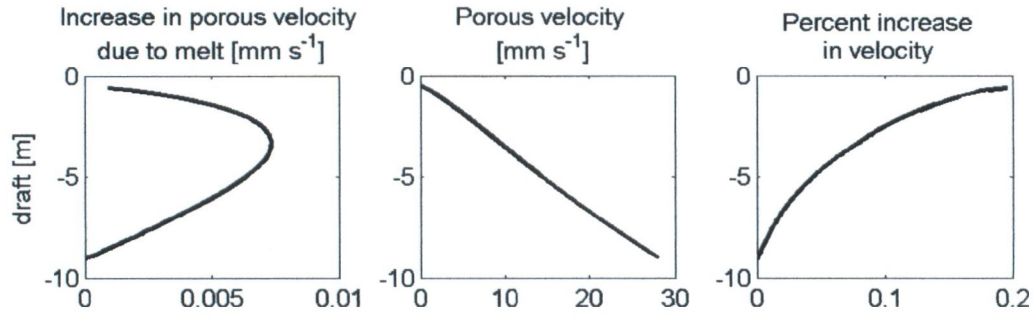

Figure 10-2: Increase in pore velocity due to influx of melt water.

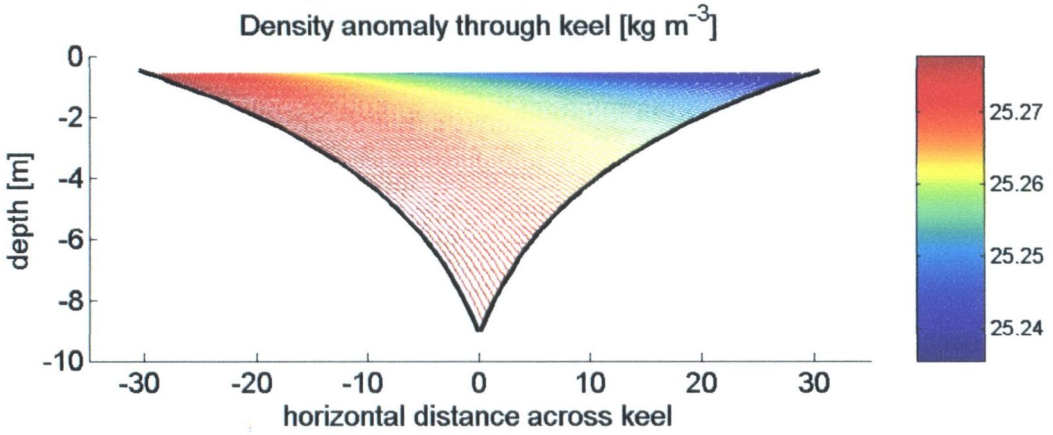

Figure 10-3: Density anomaly (from 1000 kg m^{-3}) through the keel due to the influx of fresh water and heat loss. Density varies by only 0.004% throughout the keel and pore water is stably stratified.

10.5. Sensitivity of melt to block thickness and porosity

The internal keel geometrical properties of block thickness and porosity will impact the internal melt rates. Larger blocks lead to increased pore sizes and thus an increased hydraulic radius, R_H, which appears in the equations for pore velocity and heat flux (see (9.5.2) and (9.7.9)). Increased porosity will increase the hydraulic radius. As no information on block sizes or porosity can be gathered from the sonar data, we investigate the effects of variations in geometry on melt rate using a sensitivity analysis.

Ridge porosity is reported to range between 20 to 45% (Bowen and Topham, 1996). We investigate the impact of varying porosity for a 9 m keel with block thickness set at 0.5 m. Results for porosities from 0.1 to 0.5 can be seen in Figure 10-4. As porosity increases, melt rates increase due to an increased hydraulic radius and heat transfer. However, increasing porosity will also decrease the surface area, as (9.6.4) can be rearranged as $A_P=(1-p)\gamma V_K/h$ using (9.3.7) where p is the porosity, γ is a geometrical factor (see Appendix B), and V_K is the keel volume. As porosity increases past 0.4, the increase in melt rate with porosity slows, while at porosity values in excess of 0.5, the melt rates begin to decrease due to the loss of surface area for heat transfer to occur (not shown in figure). Melt rates are thus maximized at porosities between 0.4 and 0.5, at the upper bound of observed values.

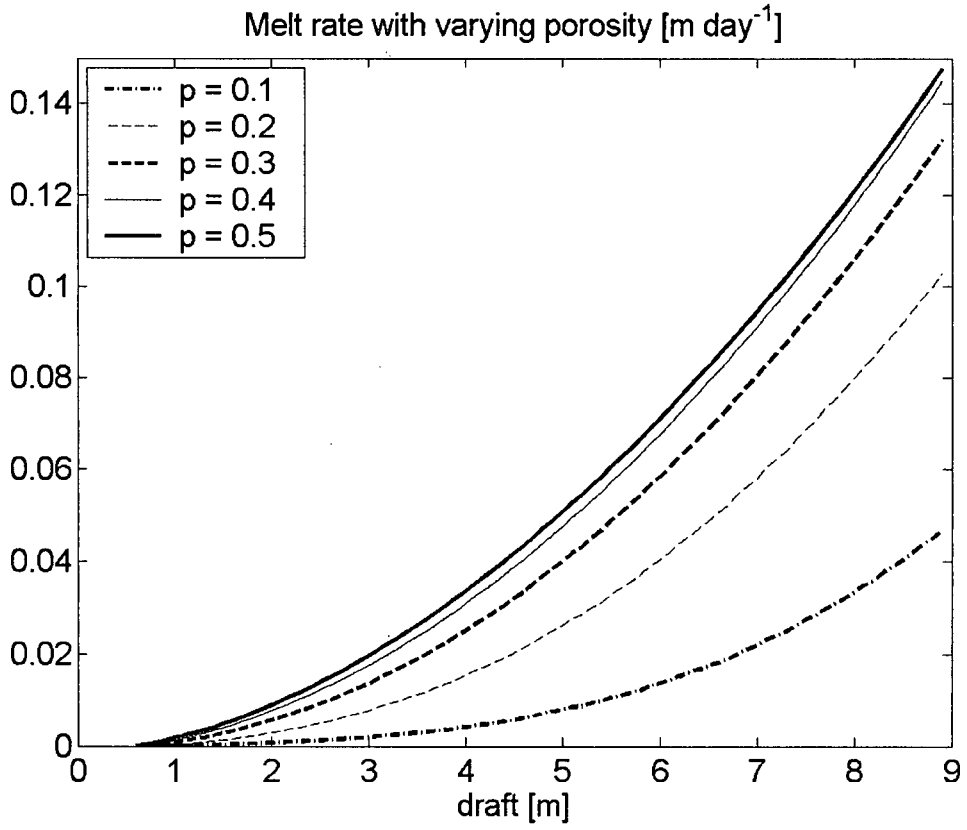

Figure 10-4: Variation in melt rates with porosity for a 9m keel with block thickness 0.5m.

The relationship between block thickness and keel draft during ridge formation is known to vary with the distribution of floe size (recall (5.2.2)).

$$H = \left[\frac{f_L}{2(1-p)}\right]^{1/2} h^{1/2} \tag{10.5.1}$$

Unfortunately, this relationship cannot be extended to provide information about the block thickness within keels observed by the sonar. While immediately following formation, surrounding level ice may indicate the thickness of the blocks within the keel, subsequent growth of the level ice means that during the winter, block thickness will be less than the thickness of the surrounding level ice. Further, the floe size constraint also suggests that all level ice within a floe may be consumed during ridging, leaving only thicker level ice adjacent to the keel.

While some keels created from very thick first year ice no doubt exist, these keels are expected to be rare, as they are only formed during the end of the winter when ice is thickest and when no thinner ice is available to be ridged. The main impact on melt is expected to come from the more common keels with moderate block thickness. All keels observed during events A and D could conceivably be formed from ice 0.5 m thick (based on a truncation of H=20 $m^{1/2}$ $h^{1/2}$) indicating that a block size estimate of 0.5 m may be reasonable.

The impact of different block thicknesses on melt is plotted in Figure 10-5. Block thickness is varied from 0.1 to 1.2 m to represent the range of blocks expected within keels. Melt rates increase with decreasing block sizes, as surface area increases (from (9.6.4)) and R_H decreases, until approximately h=0.25 m. At this point, melt rates are maximized and being to decrease, as the e-folding scale for the heat transfer (9.7.9) is dependent on R_H^2. As h decreases past 0.25 m, R_H^2 becomes very small and the e-folding scale (9.7.9) decreases such that the melt is restricted to an upstream portion of the keel and the averaged melt with draft decreases.

For the purpose of illustrating the potential for internal melt to account for the enhanced melt of ridged ice, we fix the porosity at 0.3 to match observations (Timco and Burden, 1997) and the block thickness at 0.5 m as a best guess. Further field studies of the distribution of ridge porosity and block thicknesses, especially of the numerous small 3-5 m keels would be useful in making more accurate internal keel geometry estimates.

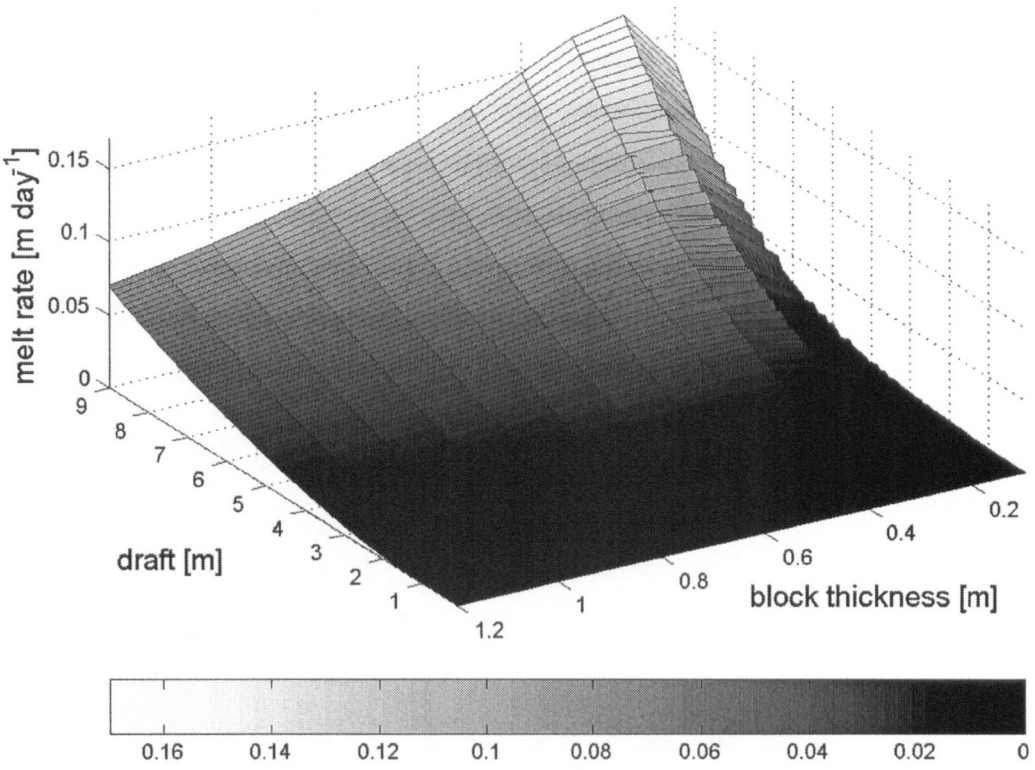

Figure 10-5: Variation in melt rate with block thickness for a 9 m keel with a porosity of 0.3.

10.6. Keel width and shape

For the 1-d Forchheimer model used to describe porous flow, the keel shape and width parameters affect the melt in similar ways. Increasing the width of a keel at a depth, via the total keel width or via the shape parameter, will decrease the pressure gradient and decrease the porous velocity given by (9.5.2). As keel widths increase and the pore velocity decreases, the e-folding scale for the heat transfer given by (9.7.9), will decrease, causing melt to occur mainly on the upstream side of the keel. As the melt rate is a statistical measure of the average melt for all ice of that draft, the overall melt rate will decrease. Note that in the real world, as no one side of the keel will consistently be upstream of the ocean currents, melt should be symmetric.

Keel width and shape parameters may not be separable from keel block thickness. Recall from section 5.2 that keel depth is a function of floe size. Keels that exceed the average width are likely

to have formed from larger floes based on the results of keel simulations (Hopkins, 1998). These keels are thus formed when the limiting truncation between H and $h^{1/2}$ approaches the mechanical limit of 20 $m^{1/2}$ (section 5.1). Then, wider keels may have blocks of smaller thickness than narrower keels. As the block thickness is such a dominant factor in determining melt rates, the errors introduced by uncertainties in keel width are secondary to concerns of block thickness.

10.7. Consolidation due to melt

The keel modelled in chapter 9 is assumed to have a porous structure that extends up to a level ice thickness equal to the block thicknesses that make up the ridge. This is the structure of a newly constructed ridge, before consolidation processes can increase the solid core of ice at the water level of a ridge. As consolidated ridged ice is predicted to have growth rates approximately twice that of level ice (Lepparanta and Hakala, 1992; Hϕyland, 2002; Veitch et al., 1991), the porous structure of a keel will extend from the maximum draft to the bottom of the consolidated portion of unknown thickness (as the keel age is unknown). However, as the heat flux is low in the upper portions of the keel (Figure 9-7), the overall melt rates within ridged ice will not be affected greatly by the loss of melt in a consolidated portion and hence the errors in melt rates are assumed to be small.

Multi year ridge keels are consolidated with very low porosities. Models and observations of melt demonstrate that this consolidation is unlikely to occur during the winter season as the consolidated layer growth rate is insufficient to extend throughout the entire keel in one winter season. Rigby and Hanson (1976) observed that voids in the ridge keel became more slush filled as the summer progressed, allowing for consolidation early in the next winter season. Internal melt due to porous flow may explain the consolidation process by allowing the keel to melt internally and eventually repack the now soft and partially melted blocks into a consolidated shape. For the purposes of model development, we have assumed this repacking would not occur during the events in early June and July simulated here, but itcould occur later in the summer, consistent with observations of Lepparanta et al., (1995) who found that porosity did not change during melt in the lower portions of the keel in the initial part of the melt season in the Baltic Sea (4^{th} February to 19^{th} April).

Further, the model assumes that the block shapes within the keel are retained throughout the summer. As the melt season progresses, the block size and orientation may change, impacting the porous flow and heat transfer. The internal melt model may then be most applicable during the early melt season, and further investigation of the evolution of the internal keel geometries due to melt is suggested.

11. INTERNAL MELT OF A DISTRIBUTION OF RIDGE KEELS

11.1. Keel statistics

To determine the characteristics of the keel population during the melt season, keels are identified within the ice draft profile using the level ice criteria of Melling and Riedel (1995). In these criteria, ridges are identified as regions of ice surrounded by level ice floes, which themselves are defined as greater than 10 m in extent and varying over only 0.25 m in thickness. For the purpose of an internal melt model, we add one more constraint to the definition of ridges. The definition of Melling and Riedel (1995) included rafted ice as a ridge if the extent of the raft was less than 10 m. To exclude rafted ice, which is not porous and thus cannot participate in internal melt, and to exclude small rubble structures where porous melt theory may not apply, the maximum draft of the keels must be at least three times the minimum draft of the surrounding level ice. Further, the edge of a keel must have a draft that exceeds the level ice draft by 0.25 m. This excludes small level ice floes (less than 10 m) from being counted in keel flanks.

Attempts to parameterize the keel width, shape, and block thickness as functions of keel depth should not be interpreted as demonstrating the dependence of these parameters on keel depth. Rather, the purpose of sections 11.2 and 11.3 is to allow the identification of average keel geometry for use in constructing a melt model. The causes of the relationships between geometrical variables and keel depth are beyond the scope of this thesis.

11.2. Keel width

Timco and Burden (1997) report keel widths to be approximately 4 times the keel draft, a value already used in this thesis to estimate the floe size needed to build a ridge of maximum draft. However, this ratio is poorly constrained, since no information is given on the types of keels measured or the criteria for measurement. A tendency to study linear ridges could bias the keel width measurement.

The ratio of the keel extent seen by the sonar to the keel draft, R, in the ice profile data during event A in 1999/2000 has a mean value of 12.7 and a standard deviation of 10.2 (Figure 11-1). Ratios of extent to draft are slightly higher in event D, perhaps due to a reduction of keel drafts due to melt. For model development, we want to assume an average keel shape, and the ratio of

keel extent to keel draft is fixed at R=13. This gives results similar to those of Melling and Riedel (1995) who found keel extent to be approximately 10 times keel draft for population of 21 large keels.

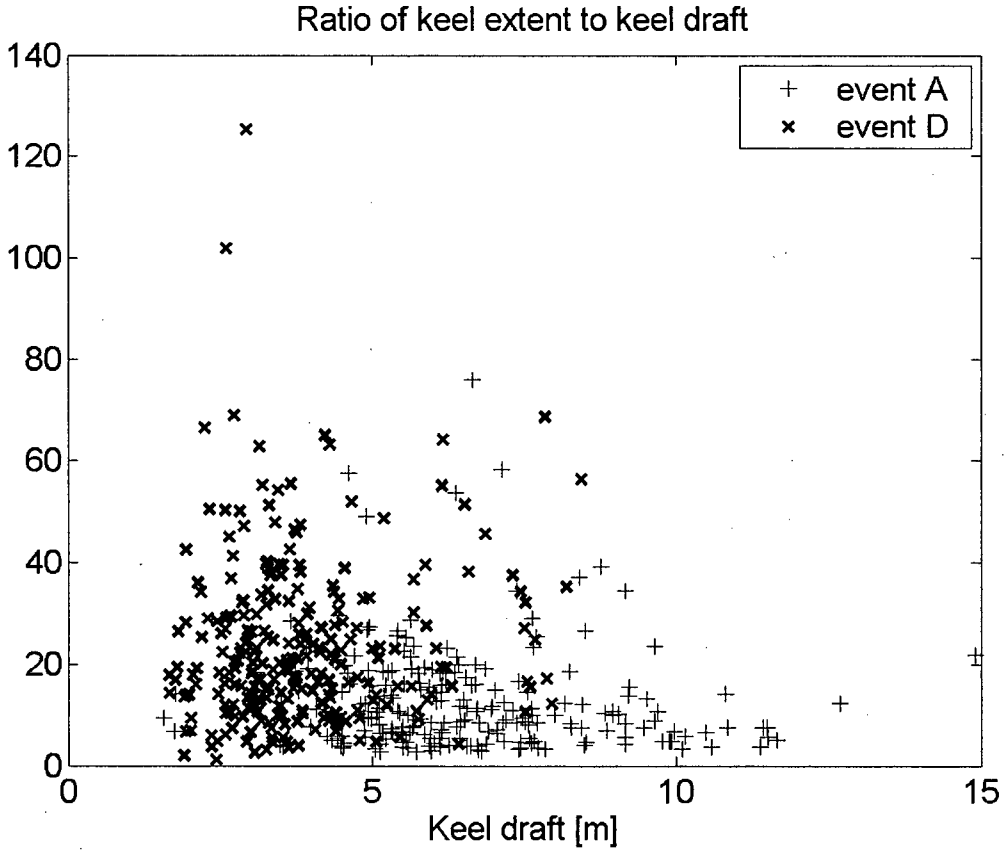

Figure 11-1: The ratio, R, of keel extent to keel draft for keels observed during event A (+) and event D (x).

Assuming that keels drift past the sonar with a random orientation, the true keel width, W, can be found from W<1/cos (θ) >= <R> H where the angled brackets indicate the average over the range of angles from 0 to $\pi/2$ radians (Figure 11-2). As the cosine of $\pi/2$ is 0, if the sonar did approach the keel at this angle, the sonar would track along the axis of the keel and the keel extent seen by the sonar would be infinite if the ridge was infinite in length. Assuming then that the maximum keel length along the keel axis is not more than 8 times the keel width, the range of angles is then 0 to $\tan^{-1}(8)$. Over this range, the mean of $1/\cos(\theta)$ is 1.92 and the true keel width works out to

be 0.52*RH*. If the keel length is 8 times the keel width, then for an 8m keel, the keel width is 53 m and the maximum expected keel extent is 430 m.

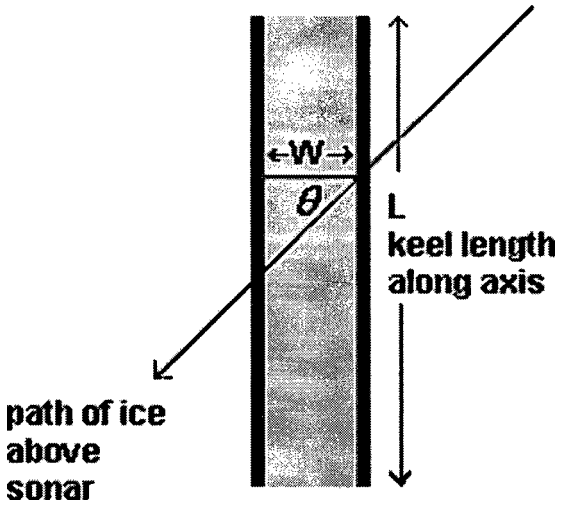

Figure 11-2: schematic of keel extent as seen by the sonar and true keel width, W.

The observed keel width to keel draft ratio is larger than the ratio of 4 times keel draft found by Timco and Burden (1997) from field measurements. This discrepancy likely stems from the inclusion of irregular shaped ridges in our keel population, including corner regions where the accumulation of rubble is greater than on linear sections (Bowen and Topham, 1996). For a melt model to work it should be based on the mean shape of all ridged ice, not just the simple linear sections of ridges, and we therefore chose to use a keel width to keel draft ratio of *0.52R*.

The use of the factor of 4 (Timco and Burden, 1997) in calculating the floe size consumed in ridging (section 5.2) may still be appropriate. Corner regions or non-linear ridges are the result of complex ridging interactions and are not yet well understood. If these wider ridged regions are created from the collision of more than two plates, then the consumed level ice from multiple plates may be close to the constraint given by (5.2.2).

11.3. Keel shape

The average distribution of ice draft within keels was found to have an exponential form in Chapter 5.5 with an e-folding scale λ. For five different keel sizes, λ was shown to increase with H, with keels at 5, 7.5, 10, 12.5, and 15 m having e-folding scales of approximately 2.7, 3.9, 4.3, 6.0, and 6.5 m, respectively. For simplicity, and due to the extreme variations in keel shape, with variations in shape exceeding the variations in e-folding scale with depth (Figure 5-8), a constant value of λ=6 m was chosen. For determining the shape of the keels used in a conceptual model of internal melt, we want to define the average-shaped keel. While these extreme variations in keel shape for individual keels are far greater than the variations in mean keel shape parameters for varying drafts, some trends can be observed when a large range of keels are studied.

The data analysis of keel shapes was repeated for two data sets collected in 2000: all keels within the winter of 1999/2000 and all keels within the spring melt season (day 150 to day 220 of 2000). Keels were binned with a $\pm$ 0.5 m range and the average keel shape (from the mean keel draft distribution) for each data set was calculated. From the mean keel shape, the e-folding scale and the standard deviation of that scale were found. The variation in e-folding scale with maximum keel draft is seen in Figure 11-3 where the keel shape e-folding scale is estimated as a linear best-fit line of the form $\lambda=0.50H-0.32$ m, for $H \geq 1$ m.

The increased error bars for the e-folding scale at large keel draft reflect the smaller sample size. While 1012 keels between 3 to 4 m in draft were observed during the 1999/2000 winter and spring seasons, only 107 keels between 8 -9 m and 8 keels between 13-14 m were observed in the same period. The e-folding scales found during 1997/1998 (Figure 11-3, filled squares) show the same pattern of a linear increase with draft, especially for keels less than 5 m. Melling and Riedel (1995) found that the mean e-folding scale for 21 keels with drafts exceeding 20 m was 15 m. Extrapolation of the best-fit line in Figure 11-3 gives an e-folding scale of 12.2 m for a 25 m keel, compatible within sampling error to the value found by Melling and Riedel (1995).

A linear best-fit can be used to estimate the average shape of a keel, and thereby predict the average melt over a population. However, the extreme variation in the shape of observed keels means that individual features will melt in greatly different ways.

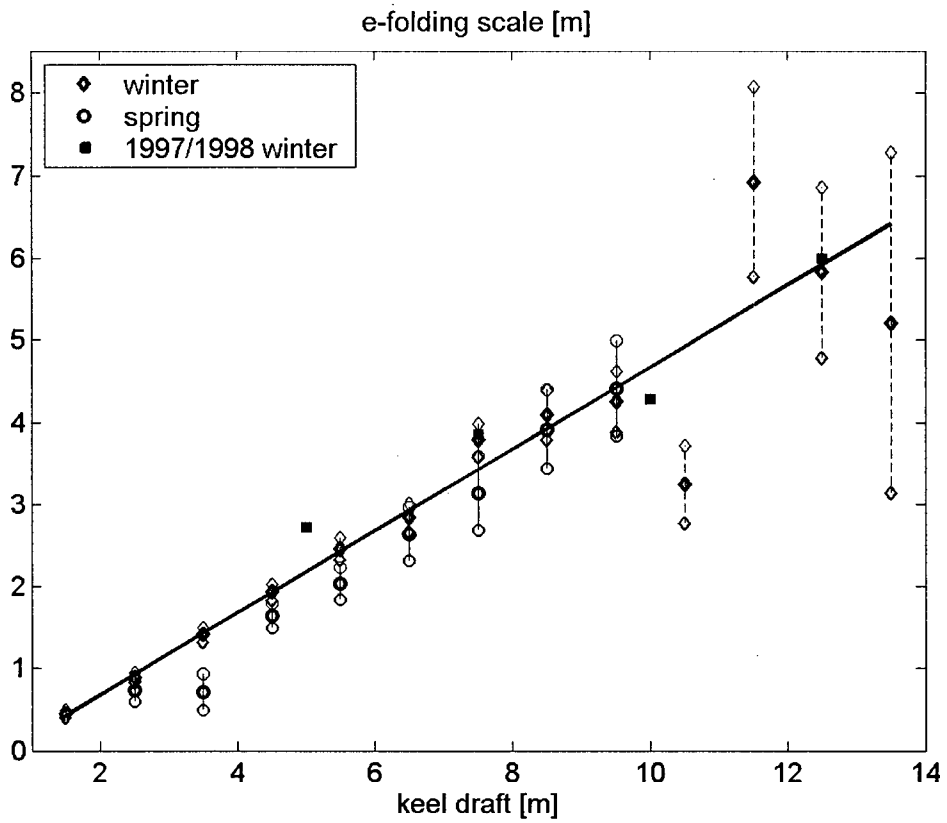

Figure 11-3: Mean e-folding scales for keels observed in 2000 during the melt season spanning events A and D (circles) and during the entire winter 1999/2000 (diamonds). Standard deviations of the e-folding scales are plotted as error bars. Observed e-folding scales from the 1997 data (section 5.5) are plotted as filled squares. The linear best-fit line takes the form $\lambda=0.50H-0.32$ m over the entire winter and spring seasons and match observations well.

11.4. Melt of a population of ridged ice

Using the keel statistics in sections 11.1 to 11.3, the enhanced melt rates for keels of average sizes can be calculated (Figure 11-4). The total melt rate is then a weighted average of these values using the distribution of keel drafts for ridged ice.

A standard definition of ridge keels (Melling and Riedel, 1995) includes all features surrounded by level ice of lesser draft. This definition includes rafted ice that is less than 10 m in extent. The internal melt model will apply only to ridged ice, as internal flow through rafted ice cannot occur. To restrict the melt model, the distributions of ridged and rafted ice, $g_{ri}(H)$ and $g_{ra}(H)$,

respectively, and the number of occurrences of each is found, η_{ri} and η_{ra}. Here rafted, or non-porous, ice is defined as ice where the maximum draft is less than three times the level ice thickness. The distribution of ridged ice is then weighted as:

$$g_{ri}'(H) = g_{ri}(H)\frac{\eta_{ri}\, g_{ri}(H)}{\eta_{ri}\, g_{ri}(H) + \eta_{ra}\, g_{ra}(H)} \tag{11.4.1}$$

The resulting distribution of ridged ice draft is shown in Figure 11-5. The sum of the distribution is less than one, approximately 0.75, as 25% of all thick ice is classed as rafted. The criteria that ridged ice must reach drafts greater than 3 times the level ice is a crude one; undoubtedly some small ridges exist that are surrounded by thick level ice. However, this criteria does serve as a good first approximation to exclude ice that is rafted or features that consist of rubbled ice of large block thickness relative to draft and thus unlikely to support porous flow. Including all ice that is not classified as level ice would be incorrect, although test simulations including these rafted ice features did not vary the melt rates significantly.

Figure 11-4 shows the modelled enhanced melt rates for event D. The expected internal melt is much greater than the observed level ice melt and the summation of internal and level ice melt can be seen to reproduce the observed melt for all but ice within the range 6-8 m. This discrepancy may be due to ridging of ice into this 6-8 m range, thus decreasing the observed melt.

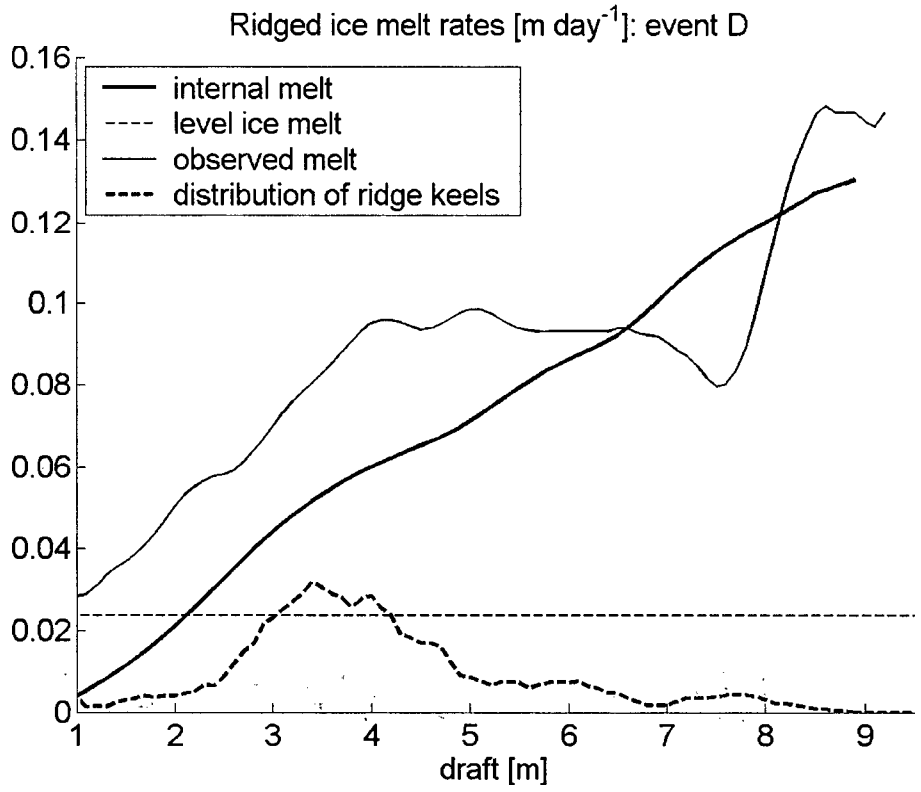

Figure 11-4: Melt rates within ridged ice during event D. The enhanced melt rate due to the internal melt (heavy black line) increases the melt rate from the level ice melt (thin dashed line) to match the observed melt rates (thin line). The probability density distribution of ridged ice (fraction per decimetre) is indicated by the heavy dashed line.

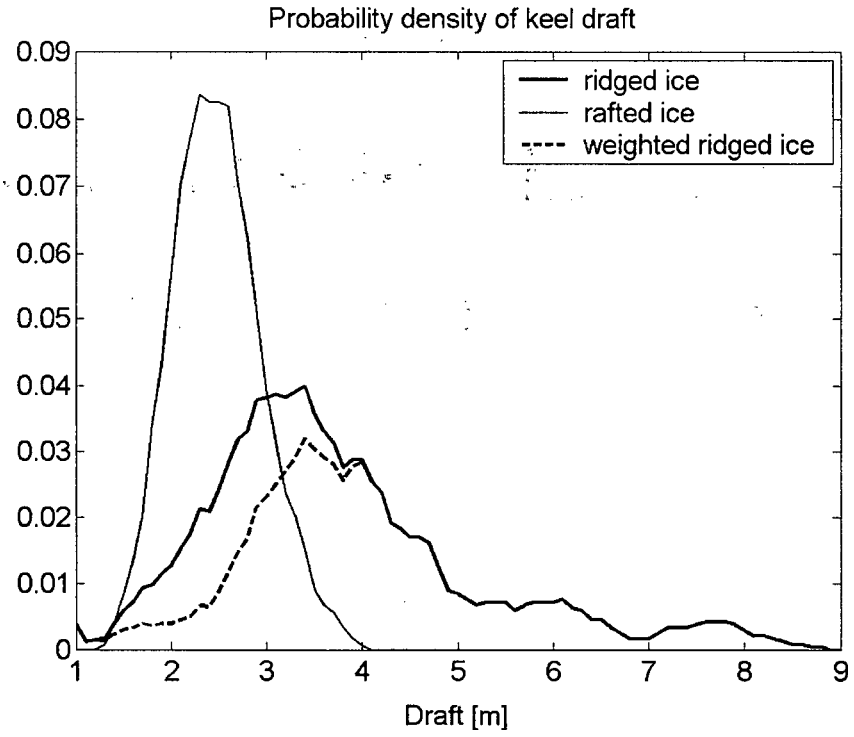

Figure 11-5: Distributions of the maximum draft of ridged ice keels (heavy line) and rafted ice (thin line) during event D (fractions per decimetre). The weighted distribution of ridged ice keels is shown as the dashed line and represents the proportion of thick ice at that draft that is in porous ridges.

The enhanced melt of a population of ice during event A (Figure 11-6) is close to the observed melt. To model event A (days 154 to 173), the water temperature was set at 0.09 degrees above freezing. This is based on the water temperature observed during the SHEBA project at day 165 during the winter of 1998 (Figure 9-3, SHEBA data). However, conditions at SHEBA two years earlier may vary greatly from conditions at the mooring site 2 in the year 2000.

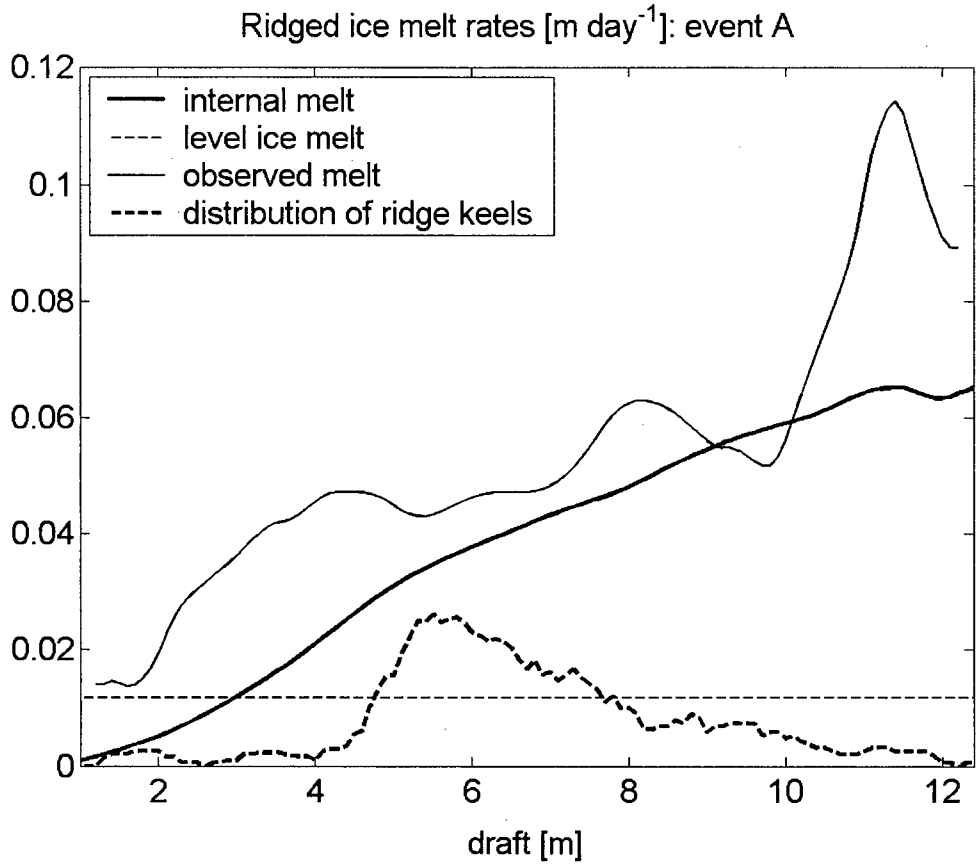

Figure 11-6: Melt rates within ridged ice during event A. The enhanced melt rate due to the internal melt (heavy black line) increases the melt rate from the level ice melt (thin dashed line) to represent most of the observed melt rates (thin line). The probability density distribution of ridged ice (fraction per decimetre) is indicated by the heavy dashed line.

11.5. Enhanced melt in redistribution models

To explore the abilities of internal melt to contribute to the observed enhanced melt of ridged ice, the internal melt rates found in Figure 11-4 and Figure 11-6 are added to the observed level ice melt and the ice draft redistribution model is run over events A and D with and without ridging. Results are displayed in Figure 11-7 and Figure 11-8 and show the ability of an internal melt model to decrease the amount of ridged ice significantly. In Figure 11-7 we see that when ridging is excluded, the model does an excellent job of reproducing the observed distribution of ridged ice, as expected from the melt rates of Figure 11-6. With ridging, the model cannot melt enough ice and is still producing new thick ridged ice.

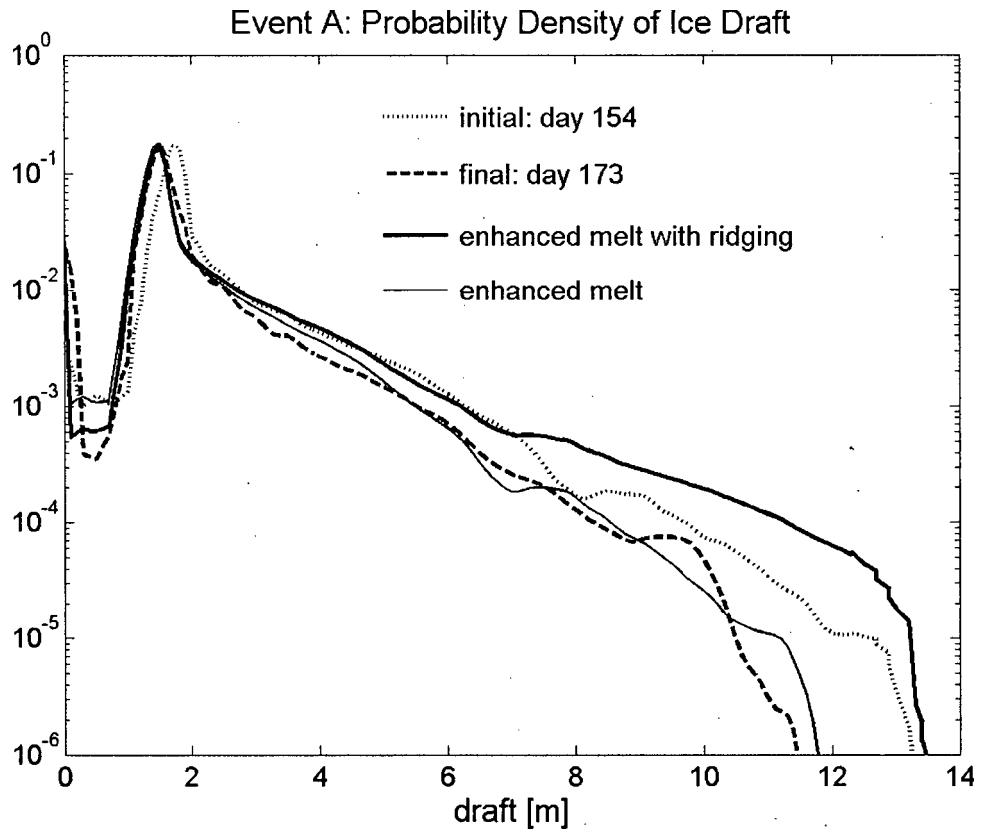

Figure 11-7: Probability density of draft (fraction per decimetre) for the internal melt model predicted distribution of ridged ice during summer melt from days 154 to 173. Allowing ridging to occur, the model predicts an increase in thick ice due to ridging (thick solid line). Without ridging (thin solid line) the model predicts a decrease in ridged ice density in agreement with observed final distribution (dashed line).

Figure 11-8 shows the distribution of ridged ice when the internal melt model is run over ice motion event D. Visible in these results is the ability of the internal melt model to melt significant amounts of ice such that, even with ridging (thick line), the model shows a decrease in ridged ice at all depths less than 5 m. At larger drafts, ridging still dominates over the predicted internal and level ice melt, resulting in an increase in ridged ice rather than the observed decrease in ridged ice. The model results with ridging and level ice melt (from Figure 8-7) are plotted as the thin dashed line, showing the marked improvement of the enhanced melt model. Model results without ridging show melt in agreement with observed melt, but are of limited value without the inclusion of ridging.

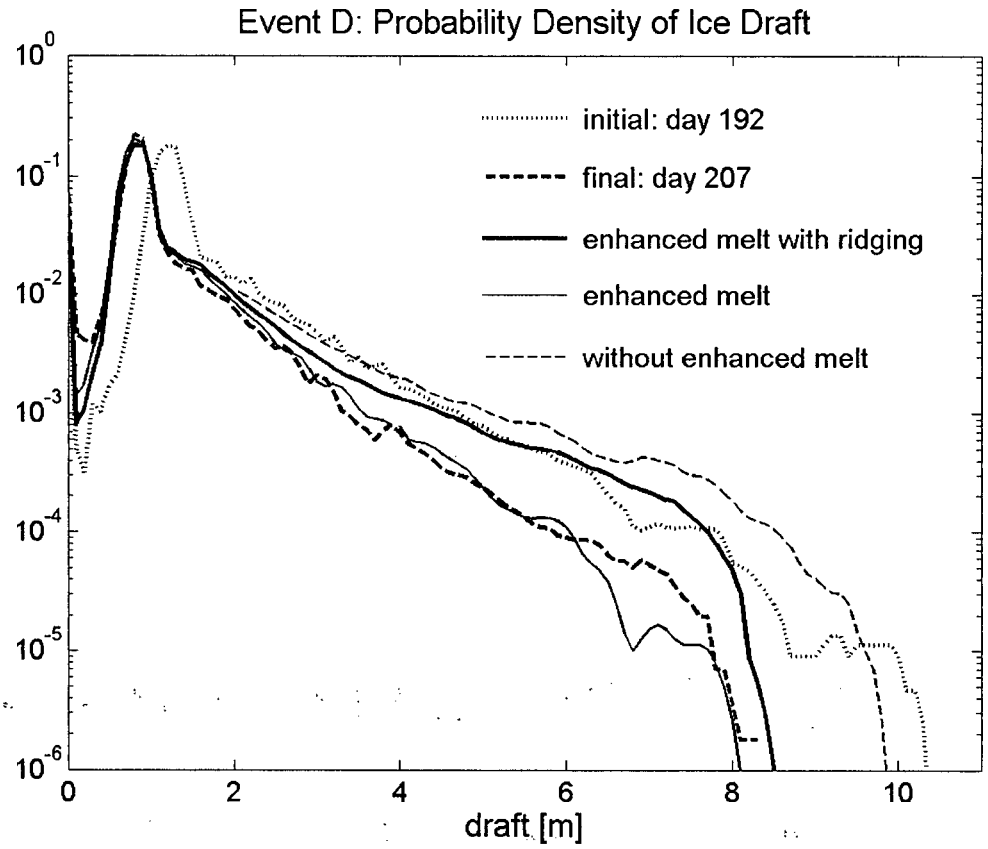

Figure 11-8: Probability density of draft (fraction per decimetre) for the internal melt model predicted distribution of ridged ice during summer melt from days 192 to 207 of 2000. When ridging is included, the enhanced melt from porous flow (heavy solid line) reduces the production of ridged ice when compared to the model with only level ice melt (thin dashed line).

11.6. Ability for internal melt to account for enhanced melt rates

The results of Figure 11-7 and Figure 11-8 demonstrate the importance of internal melt processes to the enhanced melt rates of ridged ice. However, the inability of the model to melt the thickest ice suggests that the strength of porous melt is being underestimated, which may be caused by the choice of water temperatures. The water temperature departure from freezing may be too low (as SHEBA data may not be relevant to the ocean conditions at site 2 in the year 2000), such that melt rates of ridged ice are significantly higher than those found in section 11.4.

The turbulent heat transfer to the water column due to increased mixing at the interface of the two-layer flow may increase the water temperature. As the large keels extend over a significant fraction of the upper layer of the water column, the hydraulic flow is amplified for these keels, increasing the temperature of the upper layer of the ocean. The recent work of Skyllingstad et al., (2003) demonstrated the ability of ice keels to increase turbulent velocities. This may increase the temperature of the water column and thus increase melt rates.

The estimated freezing temperature departures of 0.18 and 0.09 degrees for events D and A, respectively, are estimates based on data from another year at a different location. A temperature profile from the 3rd of June, 1987 at the edge of the landfast ice in the Beaufort Sea shows a freezing temperature departure of 0.35-0.7 degrees, indicating that a temperature difference of 0.4 degrees between the water and ice is not unreasonable, and that the earlier choices of 0.09 and 0.18 degrees may be too low. Using 0.4 degrees as the freezing temperature departure for event D, with a maximum ridge constraint of 9 $m^{1/2}$ $h^{1/2}$, greatly increases the melt of the ridged ice and produces modelled results in agreement with observed ablation (Figure 11-9).

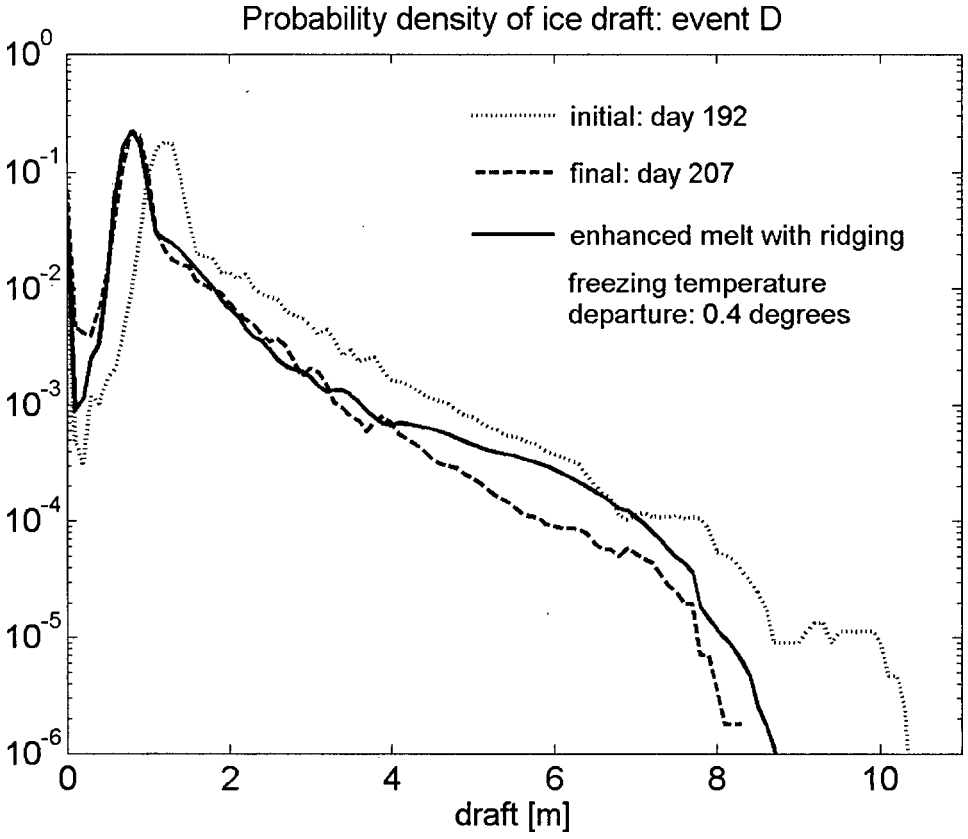

Figure 11-9: Probability density of ice draft (fraction per decimeter) for the internal melt model predicted distribution of ridged ice during summer melt from days 192 to 207 of 2000. Including the enhanced melt from porous flow (heavy solid line) with a assumed freezing temperature departure of 0.4 degrees reproduces most of the features of the observed distribution, except for an over-prediction of ice within drafts of 4-8 m.

The internal melt model proposed here, and used in section 11.6, is an initial approach with many potential unknowns. While we have chosen reasonable values for the ocean currents, keel statistics, Nusselt number, and Forchheimer coefficients, these are estimates and contribute uncertainty to the melt rates. However, the goal of this initial investigation was to demonstrate the potential for internal melt to contribute to the observed enhanced melt of ridged ice. The results clearly show that internal melt can make a significant contribution to enhanced melt and should be investigated further.

12. CONCLUSIONS: GEOMETRIC FACTORS INFLUENCING RIDGE MELT

Section D has developed and applied a semi-quantitative model for the enhanced melt of ridged ice. First, the inability of level ice melt processes to ablate thick ice is established using the ice draft redistribution model of Sections B and C. Second, a semi-quantitative model for internal ice melt in ridge keels is developed. Finally, the internal melt model is included in the ice draft redistribution model to demonstrate that internal melt processes ablate thick ridged ice in agreement with observations.

Initially, during the melt season, the model is constrained to melt level ice at a rate equal to the observed value. This provides an upper bound on the contribution of surface melt to the melt of ridged ice and allows for comparison between the observed and modelled melt of thick ice. The ridging model truncates the maximum draft of new ridges at lower drafts than in the winter season to represent the decreasing ice strength. Model results from two ice motion events during the melt season show an increase in the distribution of ridged ice, as ridging dominates melt processes, rather than the observed enhanced ablation rates. The inability of the IDR model to reproduce the evolution of ridged ice confirms that ridged ice melt cannot be represented by 1-dimensional level ice melt.

The underwater region of a ridge, consisting of interconnected ice blocks, is a porous media with a large surface area. The flow of warm oceanic water through the porous keel is suggested as a mechanism for enhanced melt. Pore velocities are estimated by adapting flow models from groundwater and engineering literature to the geometries of ridged ice. Driving the flow is the oceanic current, which generates pressure gradients across the keel. Porous flows through a 9 m keel are predicted to reach maximum velocities of 27 mm s^{-1}, for average ocean currents of 0.1 m s^{-1}.

Heat transfer from the warm oceanic water to the ridged ice is modelled as the heat transfer from a fluid to a packed bed. Integrated melt rates, assuming repacking maintains a constant porosity, reach melt rates almost five times the level ice melt rate (for a 9 m keel), supporting the role of internal melt as a contributor to enhanced melt.

Estimates for keel shape, width, and the distribution of maximum draft are found from the ice draft profiles. These parameters are combined with assumed porosity, ice block thickness, ocean current speed, and ocean temperature to calculate melt rates for a distribution of ridged ice. The enhanced internal melt rates are of the same order of magnitude and shape as the observed ablation rates calculated for two ice motion events we studied, suggesting that internal melt within the porous keel can explain the observed ablation rates. Including internal melt in the IDR model improved the simulated draft distributions of the melting thick ice.

Increasing the freezing temperature departure of the ocean to a reasonable value of 0.4 degrees above freezing, the model reproduces the ablation of ridged ice with only small variations from observed values. It is not unreasonable to assume that better estimates of ocean temperature, ice strength, and internal keel geometry will further improve the internal melt model and allow for more accurate redistribution models of enhanced ridged ice melt.

Notwithstanding the uncertainties introduced in the internal melt model through the use of average geometries or model parameters, the internal melt of ridged sea ice can be seen to explain the observed enhanced melt of ridged ice. The agreement between modelled and observed melt suggests that we have identified and quantified a major contributor to melt in ridged ice.

SECTION E: THESIS SUMMARY

13. CONCLUSIONS AND SUGGESTIONS FOR FUTURE RESEARCH

13.1. Conclusion

The ice pack of the Arctic Ocean is a complex structure of ridges, leads, and level ice, of which the large ridged features are a significant contributor to both ice area and volume. An attempt to understand the evolution of sea ice on seasonal, annual, or long-term timescales thus requires understanding of ridge-specific evolution processes. In this thesis the inability of current sea ice redistribution models to reproduce the evolution of ridged ice during winter and summer melt was demonstrated using a unique regional ice draft redistribution model that can be compared directly to observed drafts. Conventional parameterizations of ice draft redistribution during ridging and melt cannot replicate observations and suggest that ridge building and melt processes are not understood. This thesis utilizes observed ice draft profiles, ice draft redistribution model results, and conceptual models to explore geometrical constraints on ridging and melt.

During ridging, the maximum possible draft of ridge keel is constrained by ice strength. However, most keels do not grow to this maximum draft and are instead constrained by the extent of level ice available for ridging. Observations of floe size indicate that 75% of all floes are too small to form ridges of maximum draft. This suggests that approximately 75% of all ridges are size-limited by the level ice available for their creation. The inclusion of this floe size constraint in ridging models is thus necessary to limit ridged ice drafts.

Further, the shape of observed ridges differs from the conventional assumption of a triangular shaped keel. Ridge keels, on average, have a cusp-shape, with broad shoulders and steep narrow crests. The distribution of ice within a keel is exponential, with e-folding scales linearly increasing with maximum drafts. This shape constraint, along with the small ridges produced due to the floe size constraint, acts to place less ice in the thickest drafts and therefore increase the ridged ice area.

The porous structure of a first-year ridge keel permits percolation of seawater through the keel. During the melt season, when upper-layer ocean temperatures exceed the freezing point, this flow of ocean water through the keel transports heat deep into the structure, causing internal melt. A conceptual model for internal melt is developed. Melt rates are found to be dependent on the

external keel shape and the geometries of the blocks within the keels, their thickness and packing structure.

Melt rates for populations of ridged ice are calculated and found to be more than five times the melt rates of level ice, which is often assumed to be the sole contributor to ice melt. Reasonable choices for keel and ocean parameters demonstrate that internal melt processes are capable of explaining the observed enhanced melt of ridged ice. While the internal melt model developed should be viewed as a first approach, the enhanced melt of ridged ice has, for the first time, been estimated, and a physical process has been used to explain the observed enhanced melt rates.

Both ridging and ridge melt are found to be dependent on the geometric properties of the ice pack. Including these geometrical factors in ridge building and ablation models will produce more accurate estimations of ice evolution. Our understanding of ridge ice processes has been greatly increased by the knowledge that floe size, keel shape, and internal keel geometries will influence the evolution of ridged ice throughout the year.

13.2. Future directions

The dependence of the ridge sea ice on the geometrical characteristics of both level ice and ridged ice has not been previously investigated. As such, future research is needed to increase our understanding of the interconnections between such geometrical factors as keel shape, level ice extent, block thickness, and their evolution throughout the year.

The evolution of keel shape during ridge creation is unknown, but may be related to the extent of level ice consumed in ridging. Future research using particle models (e.g. Hopkins, 1996a) to explore the evolution of keel shape with level ice consumption would be of great value. Additionally, field observations of keel shape, draft, and internal geometries could be used to investigate the potential relationship between level ice extent consumed in ridging and keel shape. However, this dataset would require a great effort to collect.

To improve estimates of internal melt, the accuracy of the estimated keel shape, internal geometry, ocean temperature, and ocean velocity should be established. Ideally, a field study of a first year ridge and surrounding oceanic conditions would be conducted, with tracers used to

estimate porous flow and observations of porosity, block thickness, and ablation rates from borehole sampling used to verify model results. However, such a dedicated study may not be feasible due to funding and logistical constraints. Observations of under-ice oceanic conditions during the spring of 2004 from the CASES program, not yet available, may provide further guidance on appropriate oceanic temperatures during the melt season in the seasonal sea ice zone of the Beaufort Sea.

Similar to the research suggested above, field observations of the block thickness and external shape parameters for a wide variety of keels would allow for more accurate estimates of the block thickness. As such a study would be labour extensive and expensive, particle simulations similar to those of Hopkins (1996a) could be used to suggest block thicknesses for observed keel shapes and draft statistics, assuming such a relationship is observed.

Finally, melt rates are calculated based on average keel shapes. However, most keels are not average. Instead of the idealized cusp-shaped keel, with sides that increase continuously to a maximum draft, ridges may contain multiple draft maxima (peaks) connected by regions of lower draft (troughs). The pressure gradients across these irregular structures will differ greatly from the idealized ridges, and simple estimates for the porous flow are not possible. To investigate the impact of irregular keel shapes, a two-dimensional model of the interaction of a keel with the upper layer of the ocean would be needed. This model could also be used to investigate the contributions of hydraulic flow to internal melt by quantifying the turbulent heat transfer from below the pycnocline to the upper layer.

13.3. Implications of research

Conventional models of pack ice evolution have focused on basin-scale forcing and parameterized ridging without consideration of small-scale features of the ice pack. Here, in both winter and summer season, the evolution of the large scale pack ice is shown to be dependent on the characteristics of individual ice features. Total ice volume in the Arctic will depend on proportion of ridged ice, whose creation depends on the distribution of floe sizes and keel shapes on scales of 10 to 1000 m. The evolution of the distribution of ridged ice throughout the melt season depends on the internal geometries of the ice keels, on scales of 10 cm to 1 m. In order to

understand the basin-scale features of the ice pack, we must therefore understand the small-scale processes of ridging and melt that act to create and modify the ice cover.

The results of this research are directly relevant to the challenges of Arctic engineering. For offshore development and exploration, it is important to be able to reliably estimate both the maximum draft of ridges, and the probability of encountering a ridge of that maximum draft. With the floe size constraint, fewer ridges of maximum draft will be encountered, perhaps easing design requirements. For navigation, the strength of the sea ice, which is related to ice draft, is a limiting factor. The floe size and keel shape constraints on ridging imply that more ridged ice area is created. This increased ridged area is due to the preferential creation of smaller ridges, with ice area to volume ratios greater than those of larger ridges, by these constraints. As ridged ice impedes navigation, not including these geometric constraints in models could lead to overestimates of navigability. However, the internal melt of ridged ice suggests that ridged ice may be considerably weakened by melt, easing navigation as the melt season progresses. Offshore engineering and ship design, along with predictions of ice cover for transportation, are thus reliant on the geometric properties of the ice pack.

An understanding of the evolution of ridged ice is essential for predicting changes in sea ice area and thickness due to climate change. At present, the ice cover buffers the ocean from extreme variations in atmospheric temperature with thicker ice often lasting throughout the summer season and thus reducing heat uptake by the ocean in summer months. Climate change is often thought to lead to a decreasing ice cover, as ice melts thermodynamically. We suggest that ridging may be a dominant process in the response of sea ice to climate change. Potential increased storm activity, associated with high latitude climate variability, would cause increased ridging, and thus impact the ice extent. The floe availability constraint predicts an increase in ice of moderate drafts, rather than ice with very large keels that occupy little area. Increased ridging may therefore create a larger area of ice with drafts too thick to melt during the short summer season. Thus, ice extent may not decrease as rapidly as predicted by thermodynamic models. The internal melt model suggests a mechanism for consolidation of ridged ice to solid multi year keels, although the enhanced melt rate also suggests that many smaller keels could ablate completely during the melt season. The adaptation of present climate models to include realistic

ridging and enhanced melt will allow us to better estimate the influence of ridged ice on the Arctic heat budget.

Parameterizations of the floe size constraint on ridging and the internal melt rate for ridged ice are important corrections to the sea ice models currently used in climate change predictions. The adoption of these concepts into large-scale redistribution models will allow for increased confidence in sea ice simulations. In addition, the results of this thesis have yielded new information about the processes of ridge creation and how ridge melt contributes to ridged ice evolution. This provides us with a new awareness of the influence of small-scale geometric features on the large-scale characteristics of pack ice.

REFERENCES

1. Amundrud, T. L., H. Melling, and R. G. Ingram, Geometrical constraints on the evolution of ridged sea ice, J. Geophys. Res., 109, C06005, doi:10.1029/2003JC002251. 2004
2. Babko, O., D.A. Rothrock, and G.A. Maykut, Role of rafting in the mechanical redistribution of sea ice thickness, J. Geophys. Res., 107(C8), doi: 10.1029/1999JC000190, 2002.
3. Batchelor, G.K. An Introduction to Fluid Dynamics. Cambridge University Press, Cambridge, UK. 1967 (reprinted 2002). 615 pages.
4. Bird R.B., W.E. Stewart, and E.N. Lightfoot, Transport Phenomena. John Wiley, NY, 1960.
5. Bellchamber-Amundrud, T., G. Ingram, and H.M. Melling, Modelling the evolution of draft distribution in the sea ice pack of the Beaufort Sea, in Ice in the Environment, vol. 2, edited by V. Squire and P. Langhorne, University of Otago, Dunedin, 243-250, 2002.
6. Bitz, C.M., and W.H. Lipscomb, An energy conserving model of sea ice. J. Geophys. Res., 104(C7), 15669-15677, 1999.
7. Bitz, C.M., M.M. Holland, A.J. Weaver, and M. Eby, Simulating the ice-thickness distribution in a coupled climate model, J. Geophys. Res., 106(C2), 2441-2463, 1999JC000113, 2001.
8. Bjork, G. On the response of the equilibrium thickness distribution of sea ice to ice export, mechanical deformation, and thermal forcing with application to the Arctic Ocean. J. Geophys. Res., 97(C7), 11287-11298, 1992
9. Bowen, R.G. and D.R. Topham, A study of the morphology of a discontinuous section of a first year Arctic pressure ridge: Cold Regions Science and Technology, 24, 83-100,1996.
10. Burcharth, H.F., and O.H. Andersen, On the one-dimensional steady and unsteady porous flow equations. Coastal Engineering, 24, 233-257, 1995.
11. Cattle, H. and J. Crossley, Modelling Arctic Climate Change, Phil. Trans. R. Soc. London, 352, 201-213, 1995.
12. Cavalieri, D.J., and S. Martin, The contribution of Alaskan, Siberian, and Canadian coastal polynyas to the cold halocline layer of the Arctic Ocean, J. Geophys. Res., 99(C9), 18343-18362, 1994.
13. Cole, D.M. and L.H. Shapiro, Observations of brine drainage networks and microstructure of first-year sea ice. J. Geophys. Res., 103 (C10), 21739-21750, 1998.

14. Colony, R. and A.S. Thorndike, An estimate of the mean field of arctic sea ice motion. J. Geophys. Res., 89 (C6) 10623-10629, 1984.
15. Comfort, G. and R. Ritch, Field Measurements of Pack Ice Stresses, Vol I & II., Report prepared for Marine Works, A&ES, by Fleet Technology Ltd.,1989.
16. Corless, R.M., G. H. Gonnet, D. E. G. Hare, D. J. Jeffrey, and D. E. Knuth, `On the Lambert W Function, Advances in Computational Mathematics, 5, 329-359, 1996.
17. Cummins, P.F. Numerical simulation of upstream bores and solitons in a two-layer flow past an obstacle. J. Physical Oceanography, 25, 1504-1515, 1995.
18. Cummins P.F., D.R. Topham, and H.D. Pite. Simulated and experimental two-layer flows past isolated two dimensional obstacles. Fluid Dynamics Research, 14, 105-119. 1994.
19. Curry, J.A., J.L. Schramm, D.K., Perovitch, and J.O. Pinto, Applications of SHEBA/FIRE data to evaluation of snow/ice albedo parameterizations. J. Geophys. Res., 106 (D14), 15345-15355, 2001.
20. Darby, D., J. Bischof, G. Cutter, A. de Vernal, C. Hillaire-Marcel, G. Dwyer, J. McManus, L. Osterman, L., Polyak, and R. Poore, New record shows pronounced changes in Arctic Ocean circulation and climate. EOS Transactions, 82(49), 601, 607, 2001
21. Dempsey, J.P., R.M. Adamson, and S.V. Mulmule, Scale effects on the in-situ tensile strength and fracture of ice. Part II: First-year sea ice at Resolute, N.W.T., International Journal of Fracture, 95, 347-366, 1999.
22. Den Hartog, J.P., Advanced Strength of Materials. McGraw-Hill Book Company, Inc. New York, 379pp., 1952.
23. Dumas, J.A., G.M. Flato, and A.J. Weaver, The impact of varying atmospheric forcing on the thickness of Arctic multi year sea ice, Geophys. Res. Lett., 30(18), 1918, doi:10.1029/2003GL017433, 2003.
24. Elliott, A.H., and N.H. Brooks, Transfer of nonsorbing solutes to a streambed with bed forms: Theory. Water Resources Research, 33(1), 123-136, 1997.
25. Emery, W.J., and R.E. Thomson, Data Analysis Methods in Physical Oceanography. Pergamon. New York, 634pp., 1998.
26. Englelund, F.A., On the laminar and turbulent flows of ground water through homogeneous sand. Danish Academy of Technical Sciences. 1953.
27. Farmer, D.M., and R.A. Denton, Hydraulic control of flow over the sill in observatory inlet. J. Geophys. Res., 90 (NC5), 9051-9068, 1985.

28. Flato, G.M., Spatial and temporal variability of Arctic ice thickness, Ann. of Glaciol., 21, 323-329,1995.
29. Flato, G.M. and R.D. Brown, Variability and climate sensitivity of landfast Arctic sea ice, J. Geophys. Res., 101(C10), 25767-25777, 1996.
30. Flato, G.M. and W.D. Hibler III, Ridging and Strength in modelling the thickness distribution of arctic sea ice, J. Geophys. Res., 100(C9), 18611-18626. 1995.
31. Fox, C. and V.A. Squire, Coupling between the ocean and an ice shelf, Ann. of Glaciol., 15, 101-108, 1991.
32. Fox, C., T. Haskell, and H. Chung, Dynamic, in situ measurement of sea ice characteristic length, Ann. of Glaciol., 33, 339-344, 2001.
33. Gill, A. E., Atmosphere-Ocean Dynamics. Academic Press, San Diego, California, 662pp., 1982
34. Granberg, H.R., and M. Lepparanta, Observations of sea ice ridging in the Weddell Sea J. Geophys. Res., 104(C11), 25735-25745, 1992.
35. Haapala, J. On the modelling of ice thickness redistribution. J. Glaciol. 46, 427-437. 2000
36. Hall, K.R., G.M. Smith, and D.J. Turcke, Comparison of oscillatory and stationary flow through porous media. Coastal Engineering, 24, 217-232, 1995.
37. Hibler, W.D., III, Modelling a variable thickness sea ice cover, Mon. Weather. Rev., 108, 1943-1973, 1980.
38. Hibler, W.D. III and E.M. Schulson, On Modelling the anisotropic failure and flow of flawed sea ice. J. Geophys. Res.. 105(C7) 17105-17120, 2000.
39. Hibler, W.D. III, S.J. Mock, and W.B. Tucker III, Classification and Variation of Sea Ice ridging in the western arctic basin. J. Geophys. Res., 79 (18), 2735-2743, 1974.
40. Holland, D.M., and A. Jenkins, Modelling thermodynamic ice-ocean interactions at the base of an ice shelf. J. Phys. Oceanogr., 29, 1787-1800. 1999.
41. Hopkins, M, On the ridging of intact lead ice J. Geophys. Res., 99(C8), 16351-16360, 1994.
42. Hopkins, M. The effects of individual ridging events on the ice thickness distribution in the Arctic ice pack, Cold Reg. Sci. Technol., 24, 75-82, 1996a.
43. Hopkins, M.A., On the mesoscale interaction of lead ice and floes. J. Geophys. Res., 101(C8), 18315-18326, 1996b.

44. Hopkins, M., Four stages of pressure ridging, J. Geophys. Res., 103(C10), 21883-21891, 1998.

45. Hopkins, M. A. and Hibler, On the ridging of a thin sheet of lead ice. Annals of Glaciology, 15, 81-86. 1991.

46. Hopkins M.A., W.D. Hibler, III and G.M. Flato, On the numerical simulation of the sea ice ridging process. J. Geophys. Res., 96, 4809-4820, 1991

47. Hϕyland, K.V., Simulations of the consolidation process in first year sea ice ridges, Cold Reg. Sci. Technol., 34, 143-158, 2002

48. Hϕyland K.V. and S. Lϕset, Measurements of temperature distribution, consolidation, and morphology of a first-year sea ice ridge. Cold Reg. Sci. Technol., 29, 59-74, 1999.

49. Johnston, M., and R. Frederking, Decay of first-year sea ice: A second season of field measurements, 2001. Technical Report, HYD-TR-066, National Research Council, Canada, 2001.

50. Kells, J.A., Spatially varied flow over rockfill embankments. Can. J. Civil Eng., 20 (5): 820-827. 1993.

51. Knudsen, J. G. and D.L. Katz., Fluid Dynamics and Heat Transfer. McGraw-Hill Book Company, New York, 576 pgs, 1958.

52. Kovacs, A., and D. S. Sodhi, Shore ice pile-up and ride up: field observations, models, theoretical analyses, Cold Reg. Sci. Technol., 2, 209-288, 1980.

53. Lange, M.A., S.F. Ackley, P. Wadhams, G.S. Dieckmass, and H. Eicken, Development of sea ice in the Weddell Sea, Ann. Glaciol., 12, 92-96,1989.

54. Lawrence, G.A., The hydraulics of steady two-layer flow over a fixed obstacle. J. Fluid. Mech, 254, 605-633, 1993.

55. Lepparanta, M., and R. Hakala, The structure and strength of first year ice ridges in the Baltic Sea, Cold Reg. Sci. Technol., 20, 295-311, 1992.

56. Lepparanta, M., M. Lensu, P. Kosloff, and B. Veitch, The life story of a first-year sea ice ridge, Cold Reg. Sci. Technol., 23 279-290, 1995.

57. Lipscomb, W.H., Remapping the thickness distribution in sea ice models, J. Geophys. Res., 106(C7), 13989-14000, 2001.

58. Lowry, R.T. and P. Wadhams, On the statistical distribution of pressure ridges in sea ice. J. Geophys. Res., 84(C5), 2487-2494, 1979.

59. Makshtas, A.P., Thermodynamics of sea ice, in Physics of Ice-Covered Seas, vol. 1, ed. M. Lepparanta, Helsinki University Printing House, Helsinki, pp. 289-304, 1998.

60. Maykut, G.A., The ice environment. In "Sea Ice Biota", R. A. Horner (editor). CRC Press Inc., Florida. 21-82, 1985.

61. Maykut, G.A., The surface heat and mass balance, in The Geophysics of Sea Ice, NATO Sci. Ser., Ser B, vol 146, ed. N. Untersteiner, chap. 5, pp. 395-463, Springer-Verlag, New York, 1986.

62. Melling, H. Detection of features in first-year pack ice by synthetic aperture radar (SAR), International Journal of Remote Sensing, 19(6), 1223-1249, 1998a.

63. Melling, H. Sound scattering by sea ice: Aspects relevant to ice-draft profiling by sonar, Journal of Atmospheric and Oceanic Technology, 15, 1023-1033, 1998b.

64. Melling, H. Sea ice of the northern Canadian Arctic Archipelago. J. Geophys. Res., 107(C11), 3171, doi:10.1029/2001JC001102, 2002.

65. Melling, H., and D.A. Riedel, Draft and Movement of Pack Ice in the Beaufort Sea, April 1991-April 1992, Can. Tech. Rep. Hydrogr. Ocean Sci., No. 162, 109 pp. 1994.

66. Melling, H., and D.A. Riedel, The underside topography of sea ice over the continental shelf of the Beaufort Sea in the winter of 1990, J. Geophys. Res., 100(C7), 13641-13653, 1995.

67. Melling, H., and D.A. Riedel, Development of seasonal pack ice in the Beaufort Sea during the winter of 1991-1992: A view from below, J. Geophys. Res., 101(C5), 11975-11991, 1996a.

68. Melling, H., and D.A. Riedel, The thickness and ridging of pack ice causing difficult shipping conditions in the Beaufort Sea, Summer 1991, Atmosphere-Ocean, 34(3), 457-487, 1996b.

69. Melling, H., D.R. Topham, and D.A. Riedel, Topography of the upper and lower surfaces of ten hectares of deformed sea ice. Cold Regions Science and Technology, 21, 349-369, 1993.

70. Melling, H., P. H. Johnston, and D.A. Riedel, Measurements of the underside topography of sea ice by moored subsea sonar, J. Atmos. Oceanic Technol., 12, 589-602, 1995.

71. Mock, S.J., A.D. Hartwell, and W.D. Hibler III, Spatial aspects of pressure ridge statistics. J. Geophys. Res., 77(33), 5945-5953, 1972.

72. Overland, J.E., B.A. Walter, T.B. Curtin and P. Turet, Hierarchy and sea ice mechanics: A case study from the Beaufort Sea. J. Geophys. Res., 100(C3), 4559-4572, 1995.

73. Parkinson, C.L., and W.M. Washington, A large-scale numerical model of sea ice, J. Geophys. Res., 84, 311-337, 1979.

74. Parmerter, R.R. and M.D Coon, Model of pressure ridge formation in sea ice, J. Geophys. Res., 77(33), 6565-6575, 1972.

75. Perovitch, D.K., T. C. Grenfell, B. Light, and P.V. Hobbs, Seasonal evolution of the albedo of multi year Arctic sea ice, J. Geophys. Res., 107(C10), 8044, do:10.1029/2000JC000438, 2002.

76. Pite, H.D., D.R.Topham, and B.J. van Hardenberg, Lab measurements of the drag force on a family of two-dimensional ice keel models in a 2-layer flow. J. Phys.Oceanogr. 25(12) 3008-3031, 1995.

77. Proshutinsky, A., M. Steele, J. Zhang, G. Holloway, N. Steiner, S. Haakinen, D. Holland, R. Gerdes, C. Koeberle, M. Karcher, M. Johnson, W. Maslowski, W Hibler, and J. Wang, Multinational effort studies differences among Arctic ocean models, Eos Trans. AGU, 82(51), 637,643-644, 2001.

78. Richter-Menge, J.A. and B.C. Elder, Characteristics of pack ice stress in the Alaskan Beaufort Sea J. Geophys. Res., 103(C10), 21817-21829, 1998.

79. Richter-Menge, J., B. Elder, K. Claffey, J. Overland, and S. Salo, In situ sea ice stressed in the western Arctic during the winter of 2001-2002, in Ice in the Environment, vol. 2, edited by V. Squire and P. Langhorne, University of Otago, Dunedin, 423- 430, 2002.

80. Rigby, F.A. and A. Hanson, Evolution of a large arctic pressure ridge. AIDJEX Bull. 34, 43-71, 1976

81. Rothrock, D.A., Ice thickness distribution – Measurement and theory, in The Geophysics of Sea Ice, NATO Sci. Ser., Ser B, vol 146, ed. N. Untersteiner, chap. 8, pp. 551-575, Springer-Verlag, New York, 1986.

82. Rothrock D.A. and A.S. Thorndike, Geometric properties of the underside of sea ice. J. Geophys. Res., 85(C7), 3955-3963, 1980.

83. Sanderson, T.J.O., Ice Mechanics: Risks to Offshore Structures, Graham and Trotman, London, 253 pp., 1988.

84. Savage, S. B., Review of Sea-Ice Thickness Redistribution Models. Prepared for the Canadian Ice Service. Contract KM149-1-85-018, Technical Report 2001-02, 2001.

85. Sayed, M. and R.M. Frederking, Measurements of ridge sails in the Beaufort Sea. Can. J. Civ. Eng. 16, 16-21. 1989.

86. Schramm, J.L., Flato, G.M., and Curry, J.A., Toward the modelling of enhanced basal melting in ridge keels, J. Geophys. Res., 105(C6), 14081-14092, 2000.

87. Shulkes, R.M., A note on the evolution equations for the area fraction and the thickness of a floating ice cover, J. Geophys. Res., 100(C3), 5021-5024, 1995.

88. Shen, H.W., H.M., Fehlman, and C. Mendoza, Bed form resistance in open channel flows. J Hydraulic Engineering, 116(6), 799-815, 1990.

89. Skyllingstad, E.D., C.A. Paulson, W.S. Pegau, M.G. McPhee, and T. Stanton, Effects of keels on ice bottom turbulence exchange, J. Geophys. Res., 108(C12), 3372, doi: 10.1029/2002JC001488, 2003.

90. Smith, S.D., R.D. Muench, and C.H. Pease, Polynyas and Leads: An overview of physical processes and environment, J. Geophys. Res., 95(C6) 9461-9479, 1990.

91. Thibodeaux, D. J. and J. D. Boyle. Bedform-generated convective transport in bottom sediment. Nature, 325(22), 341- 343, 1987.

92. Thorndike, A.S., Estimates of sea ice thickness distribution using observations and theory, J. Geophys. Res., 97(C8), 12601-12605, 1992.

93. Thorndike A.S., Sea ice thickness as a stochastic process, J. Geophys. Res., 105(C1), 1311-1313, 2000.

94. Thorndike, A.S., D.A. Rothrock, G.A. Maykut, and R. Colony, The thickness distribution of sea ice, J. Geophys. Res., 80(33), 4501-4513, 1975.

95. Timco, G.W. and R.P. Burden, An analysis of the shapes of sea ice ridges, Cold Reg. Sci. Technol., 25, 65-77, 1997.

96. Tucker, W.B. III, W. F. Weeks, and M. Frank, Sea Ice ridging over the Alaskan continental shelf J. Geophys. Res., 4885-4897, 1979.

97. van Gent, M.R.A., Porous flow through rubble-mounded material, J. Waterw. Port Coastal Ocean Eng., 3, 176-181, 1995.

98. Veitch, B., Kujala, P., Kosloff, P., and Lepparanta, M., Field measurements of the thermodynamics of an ice ridge, M-114 Laboratory of Naval Architecture and Marine Engineering, i - vi , 1 - 33 1991.

99. Venegas, S.A. and L.A. Mysak, Is there a dominant timescale of natural climate variability in the Arctic?, J. Clim., 13, 3412-3434, 2000

100. Vittal, N., K.G. Ranga Raju, and R.J. Garde. Resistance of two dimensional triangular roughness. J Hydraulic Research, 15, 19-35, 1977.

101. Wong, J., S. Beltaos, and B.G. Krishnappan, Seepage flow through simulated grounded ice jam, Can. J. Civil, Eng., 12, 926-929, 1985.

APPENDICES

Appendix A VARIABLES AND PARAMETERS

Symbol	Meaning	Units
a	Conservation of area constant	
A, B	Constants related to thermal ice growth	[ ]
$b(i)$, b_o	Conservation of volume transfer coefficients	
b_1, b_2	Ice block length scales	m
C_d	Average drag coefficient	[ ]
C_p	Local pressure coefficient	[ ]
c_p	heat capacity of water	4218 J kg^{-1}
d	Diameter of sphere	m
d_1, d_2	depths of upper and lower layers of the ocean	m
D	pipe diameter	m
div	Rate of divergence	% day^{-1}
d_{layer}	Depth of oceanic mixed layer	m
E	Young's modulus	Pa
E_I	Internal energy of a fluid per unit mass	$m^2 s^{-2}$
f	Ice thermal growth rate	m day-^{1}
F	Thermal growth matrix operator	
F_I	Heat flux within the keel	W m^{-2}
F_B	Longwave heat flux (up)	W m^{-2}
F_L	Longwave heat flux (down)	W m^{-2}
f_L	Floe extent	m
F_{net}	Heat flux	W m^{-2}
F_o	Froude number of flow	[ ]
$F_{oceanic}$	Heat flux from ocean	W m^{-2}
F_s	Shortwave heat flux	W m^{-2}
F_t	Turbulent heat flux	W m^{-2}
G	Vector probability distribution of thickness, $\Sigma G=1$;	m^{-1}
$\breve{g}$	Gravitational acceleration constant	m s^{-2}
$g(h)$	Probability distribution of ice thickness/draft	m^{-1}
$g_{ri}(H)$	Probability distribution of maximum ridge draft	m^{-1}

$g_{ra}(H)$	Probability distribution of maximum rafted ice draft	m^{-1}
h	draft of sea ice	m
Δh	change in draft associated with melt	m
h1, h2	draft of ice at value of the cumulative density distribution	
H	Keel draft	m
h^*	Bin size	m
I	Identity matrix	[ ]
I	Hydraulic gradient	[ ]
K	Constant of hydraulic conductivity	$m\ s^{-1}$
K_T	Turbulent Forchheimer coefficient	$s^2\ m^{-2}$
L	total number of samples in the ice profile	[ ]
L_i	Latent heat of fusion, ice	$J\ kg^{-1}$
l_1, l_2, l_3	Arbitrary length scales	m
L_c	Characteristic buckling length	m
L_P	Characteristic pore length scale	m
m	Buckling mode number	[ ]
N	Number of blocks in V_M	[ ]
N_T	Number of tubes in a section of keel volume	[ ]
n	Poisson's ratio	[ ]
$\mathcal{N}$	Number of independent samples in ice profile	[ ]
η_{ri}	Number of rafted keels	[ ]
η_{ra}	Number of ridged keels	[ ]
Nu	Nusselt number	[ ]
p	Porosity	%
P	Pressure	Pa
Q_m	Heat flux of water due to melt	W
Q_o	Heat flux of water at entrance to keel	W
Q_x	Heat flux of water at distance, x, along tube	W
r	ratio of porous fraction, p, to solid fraction, 1-p.	[ ]
R	ratio of keel extent to keel width	[ ]
Re	Reynolds number	[ ]
R_H	Hydraulic Radius	[m]

S	Open water source vector, S_1=1; S_n=0;	[ ]
$s(z)$	segment of keel with a draft, z	m
t	Time,	s or day
ΔT	Temperature difference between fluid and pipe	K
T_o	Temperature of ocean above freezing	K
$T_x(x)$	Temperature above freezing (K) of porous flow	K
u	Ice velocity	m s^{-1}
u, u_o	Characteristic pore velocity	m s^{-1}
$u_x(x)$	pore velocity across the keel	m s^{-1}
U	Characteristic free stream velocity	m s^{-1}
V	Discharge flow velocity	m s^{-1}
V_B	Volume of a block	m^3
V_M	Volume of material	m^3
V_P	Volume of pores in material	m^3
V_T	Volume containing one tube	m^3
V_K	Volume of keel, similar to V_M	m^3
Vf_m	Volume flux of water due to melt	m^3 s^{-1}
Vf_o	Volume flux of water at entrance to keel	m^3 s^{-1}
Vf_x	Volume flux of water at distance, x, along tube	m^3 s^{-1}
W	Width of keel	m
$W_k(z)$	Width of keel as a function of z and λ	m
$\dot{\varepsilon}$	Convergent strain rate	% day^{-1}
Ω	Bernoulli's constant of conserved energy	m^2 s^{-2}
Ψ_{ij}	Mechanical ridging matrix operator with indices i,j	
α', β'	Forchheimer coefficients	[ ]
α, β	Forchheimer coefficients	[ ]
$\beta(j)$, $\beta(h)$	Truncation factors	$m^{-1/2}$
κ	Thermal conductivity of water	0.56 J m^{-1} $s^{-1}K^{-1}$
λ	Characteristic e-folding scale of exponential distribution of draft within a keel	m
ν	Viscosity of water, 1.8×10^{-6}	m^2 s^{-1}

θ	Number of cumulative freezing days	days
ρ_i	Density of ice	kg m^{-3}
ρ_w, ρ	Density of water	kg m^{-3}
σ	Buckling stress	Pa
$\omega(z)$	keel width at draft, z	m
ψ	Mechanical ridging operator	
ζ	generic constant used for a placeholder.	[ ]

Appendix B HYDRAULIC RADIUS FOR SPHERES AND RECTANGLES

For flow through a granular medium, the hydraulic radius can be defined as the ratio of the pore volume to the pore surface area. Typically, in hydro-geological systems, the solid particles are approximated by spheres and the hydraulic radius is given as R_H= [p/(1-p)]d/6, where d is the sphere diameter and p is the porosity (Burcharth and Andersen, 1995).

For spherical particles, V_M is the volume of the media and V_p is the volume of the pores:

(13.3.1) $$V_P = pV_M$$

Pore volume can also be defined as a function of the number of particles, N, when the volume of each particle is given by the volume of a sphere, $V_{sphere}=\pi d^3/6$, where d is the sphere diameter.

(13.3.2) $$V_P = V_M - N\frac{\pi d^3}{6}$$

Solving (13.3.1) and (13.3.2) for N, the number of particles:

(13.3.3) $$N = \frac{V_M - V_P}{\pi d^3/6} = \frac{6V_M(1-p)}{\pi d^3}$$

The hydraulic radius, R_H, can then be found as the ratio of the pore volume to the pore surface area, which is the same as the particle surface area, $N\pi d^2$.

(13.3.4) $$R_H = \frac{pV_M}{N\pi d^2} = \frac{pV_M}{\pi d^2}\cdot\frac{\pi d^3}{6\cdot V_M(1-p)}$$
$$R_H = \frac{d}{6}\left(\frac{p}{1-p}\right)$$

The hydraulic radius of a triangular ice keel can be derived in a similar fashion. The volume of the keel is V_K and that of the pores, V_P.

(13.3.5) $$V_P = pV_K$$

The volume of the pores is again a function of the number of blocks. Letting the dimensions of the block be multiples b_1 *and* b_2 of the thickness, h, the volume and surface area of a block are given by:

(13.3.6) $$V_B = b_1 b_2 h^3$$

(13.3.7) $$A_B = (b_1 b_2 + b_1 + b_2) 2h^2$$

And pore volume and pore surface are (same as block surface area) are:

(13.3.8) $$V_P = V_K - N b_1 b_2 h^3$$
$$A_P = 2N(b_1 b_2 + b_1 + b_2) h^2$$

Again solving for the number of blocks, n:

(13.3.9) $$N = \frac{(1-p)\, V_K}{b_1 b_2 h^3}$$

The hydraulic radius is then the ratio of pore volume to pore surface area:

(13.3.10) $$R_H = \frac{p V_k}{2N(b_1 b_2 + b_1 + b_2) h^2} = \left(\frac{p}{1-p}\right) \frac{b_1 b_2 h}{2(b_1 b_2 + b_1 + b_2)}$$

The factor [p/(1-p)] is the ratio of the porous fraction to the solid fraction. Representing the block geometry, the factor γ is introduced and equation (13.3.10) becomes:

(13.3.11) $$R_H = \frac{p}{(1-p)} \frac{h}{\gamma}$$

From research looking at block sizes in ice keels in the Beaufort Sea, we can estimate the hydraulic radius; R_H. Block structure data is available from a detailed study of landfast ridge sails near 70° N, 133° -137° W by Sayed and Frederking (1989) found that the ratios of block length and width to block thickness were 2.33 and 1.26 respectively. Substituting these ratios for b_1 and b_2, γ is approximately 4.45.

At first glance, this value for R_H appears larger as the hydraulic radius for a medium constructed of spheres. It should be recognized though that the thickness, h, is the smallest of the three dimensions: height, length, and width; while the diameter is the only dimension. An average diameter for a block of sides h x 2.3h x 1.3h would be 1.43h, making the hydraulic radius for blocks proportional to (1/6.4) of the average dimension, compared to value of $1/6^{th}$ for spheres.

For a block thickness of 1 m and porosity of 30%, the hydraulic radius is approximately 10cm, for a block thickness of 0.1m the hydraulic radius is 1 cm.

Appendix C DERIVATION OF KEEL WIDTH

The observed averaged distribution of ice within the keel can be approximated by a negative exponential with an e-folding scale of 6 m (see Section 5.5). Here, z is the draft of the ice along the envelope of the keel, and h is the level ice draft.

(13.3.12) $$b(i) = b_o e^{-z/\lambda}$$

Assuming that the keel has a smooth cusp-shape (averaged shape), the relative length of the segment, s(z), at draft z to the segment at draft h is:

(13.3.13) $$\frac{s(z)}{s(h)} = \frac{e^{-z/\lambda}}{e^{-h/\lambda}}$$

And the absolute length of any segment is:

(13.3.14) $$s(z) = \zeta e^{(h-z)/\lambda}$$

We know the total width of the keel, W, from the ice profiles (see section 11), which allows us to solve for the constant in (13.3.14) as the total width of the keel is the sum of all the segments.

(13.3.15) $$\zeta = \frac{W}{e^{h/\lambda} \int_H^h e^{-z/\lambda}}$$

The width of the keel at any draft, z, is then:

(13.3.16) $$\omega(z) = \frac{W \int_H^z e^{-z/\lambda}}{\int_H^h e^{-z/\lambda}} = \frac{W(e^{-H/\lambda} - e^{-z/\lambda})}{e^{-H/\lambda} - e^{-h/\lambda}}$$